

## INFORMATION TO USERS

The most advanced technology has been used to photograph and reproduce this manuscript from the microfilm master. UMI films the text directly from the original or copy submitted. Thus, some thesis and dissertation copies are in typewriter face, while others may be from any type of computer printer.

**The quality of this reproduction is dependent upon the quality of the copy submitted.** Broken or indistinct print, colored or poor quality illustrations and photographs, print bleedthrough, substandard margins, and improper alignment can adversely affect reproduction.

In the unlikely event that the author did not send UMI a complete manuscript and there are missing pages, these will be noted. Also, if unauthorized copyright material had to be removed, a note will indicate the deletion.

Oversize materials (e.g., maps, drawings, charts) are reproduced by sectioning the original, beginning at the upper left-hand corner and continuing from left to right in equal sections with small overlaps. Each original is also photographed in one exposure and is included in reduced form at the back of the book.

Photographs included in the original manuscript have been reproduced xerographically in this copy. Higher quality 6" x 9" black and white photographic prints are available for any photographs or illustrations appearing in this copy for an additional charge. Contact UMI directly to order.

# U·M·I

University Microfilms International  
A Bell & Howell Information Company  
300 North Zeeb Road, Ann Arbor, MI 48106-1346 USA  
313/761-4700 800/521-0600



**Order Number 9028922**

**The design and implementation of a three-dimensional, primitive  
equation ocean circulation model**

**McCalpin, John D., Ph.D.**

**The Florida State University, 1990**

**U·M·I**  
300 N. Zeeb Rd.  
Ann Arbor, MI 48106



THE FLORIDA STATE UNIVERSITY  
COLLEGE OF ARTS AND SCIENCES

THE DESIGN AND IMPLEMENTATION OF A THREE-DIMENSIONAL,  
PRIMITIVE EQUATION OCEAN CIRCULATION MODEL

By

JOHN D. MCCALPIN

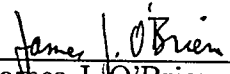
A Dissertation submitted to the  
Department of Oceanography  
in partial fulfillment of the  
requirements for the degree of  
Doctor of Philosophy

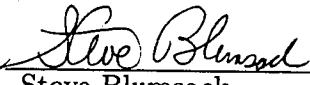
Degree Awarded:

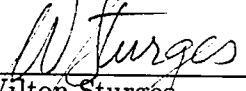
Spring Semester, 1990

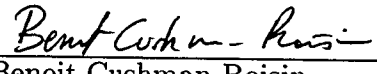
The members of the Committee approve the dissertation of John D. McCalpin on January 19, 1990.

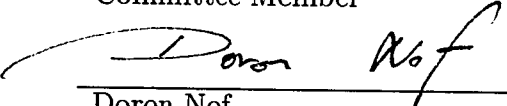
Approved:

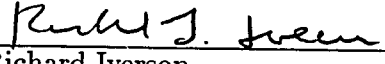
  
\_\_\_\_\_  
James J. O'Brien  
Professor Directing Dissertation

  
\_\_\_\_\_  
Steve Blumsack  
Outside Committee Member

  
\_\_\_\_\_  
Wilton Sturges  
Committee Member

  
\_\_\_\_\_  
Benoit Cushman-Roisin  
Committee Member

  
\_\_\_\_\_  
Doron Nof  
Committee Member

  
\_\_\_\_\_  
Richard Iverson  
Committee Member

Approved:

  
\_\_\_\_\_  
Ya Hsieh, Chair, Department of Oceanography

THE DESIGN AND IMPLEMENTATION OF A THREE-DIMENSIONAL,  
PRIMITIVE EQUATION OCEAN CIRCULATION MODEL

(Publication No.            )

John D. McCalpin, Ph.D.

The Florida State University, 1990

Major Professor: James J. O'Brien, Ph.D.

The development and implementation of a new, primitive equation ocean circulation model is described. The model employs finite-difference discretization in the horizontal directions and a linear, Galerkin finite-element discretization in the vertical direction. A novel coordinate transformation is employed to retain fourth-order accuracy in the vertical.

The main emphasis of this work is an extensive discussion of the decisions concerning physical, numerical, and computational issues, including discussions of several competitive (and currently interesting) numerical schemes which were not chosen. The model is compared and contrasted with the current generation of ocean circulation models. The performance of the model is tested in several simple cases. Finally, some future applications of the model are outlined.

A series of high-resolution experiments with the barotropic part of the code are used to discuss the flow along a seamount chain, modelled after the the Fieberling Guyot and its neighbors. The basic features of the flow are described and the numerical convergence of the model is demonstrated. The full three-dimensional code is applied to a the single-seamount geometry with a variety of amplitudes.

Other specific results of this work include: (1) An analysis of the incomplete cancellation of the pressure terms in the transformed coordinate system, with a simple estimate for the spurious acceleration. (2) An analysis of the semi-Lagrangian advection scheme used in some atmospheric models. The damping of the scheme is described in terms of an equivalent Laplacian or biharmonic viscosity coefficient, and formulae are derived for calculating the resolution required to obtain damping below a desired threshold. (3) A discussion of the three-dimensional semi-implicit scheme. It is shown that the scheme becomes physically ill-posed as the stratification of the fluid goes to zero.



## Acknowledgements

The author gratefully acknowledges the support of the faculty and staff of the Supercomputer Computations Research Institute. I would like to especially acknowledge Dr. David Kopriva, for serving as a *de facto*, but unofficial, member of my committee. I would also like to thank Dr. Dennis Morrow, Mr. Daan Sandee, and Mr. Bill Holter for contributing to my knowledge of supercomputers, and Dr. Dennis Duke, Associate Director of SCRI, for allowing me such a close and fruitful relationship with the Institute.

This work was made possible by research grants from the Physical Oceanography Section of the Office of Naval Research, the National Science Foundation, the Oceanic Processes Branch of NASA, and by a PACER Fellowship to the author from Control Data Corporation — all under the direction of Dr. James J. O'Brien, Secretary of the Navy Professor of Meteorology and Oceanography.

Some of the calculations reported in this work were performed on the Cyber 205 and ETA-10 supercomputers at the Florida State University, supported in part by the Department of Energy.

Most importantly, I am indebted to my wife, Julie, for her patience and support throughout this long, and often frustrating, adventure.

# Contents

<b>1</b>	<b>Introduction</b>	<b>1</b>
1.1	Review of Large-Scale Ocean Modelling . . . . .	3
1.1.1	The Primitive Equations . . . . .	4
1.1.2	More Simplified Ocean Models . . . . .	5
1.2	The New Model - Background . . . . .	8
<b>2</b>	<b>The New Model</b>	<b>11</b>
2.1	Horizontal Discretization: FD vs FE vs Spectral . . . . .	11
2.1.1	Accuracy . . . . .	12
2.1.2	Computational Efficiency . . . . .	17
2.1.3	Discussion . . . . .	21
2.1.4	The Arakawa C-grid . . . . .	22
2.2	Vertical Discretization . . . . .	23
2.2.1	Coordinate System . . . . .	24
2.2.2	Linear, Galerkin Finite-Element Scheme . . . . .	26
2.3	Time Integration Schemes . . . . .	30
2.3.1	Advection Schemes . . . . .	30
2.3.2	Gravity Waves . . . . .	31
2.3.3	Horizontal Diffusion . . . . .	33

2.3.4	Vertical Diffusion . . . . .	35
2.3.5	Coriolis Terms . . . . .	36
2.4	Physics . . . . .	36
2.4.1	Diffusive and Dissipative Processes . . . . .	36
2.4.2	Convective Adjustment . . . . .	38
2.4.3	Boundary Conditions . . . . .	39
2.4.4	Equation of State . . . . .	43
<b>3</b>	<b>Derivations and Differencing</b>	<b>44</b>
3.1	Introduction . . . . .	44
3.2	Governing Equations . . . . .	44
3.2.1	Boundary Conditions . . . . .	47
3.3	Coordinate Transformations . . . . .	48
3.3.1	Viscous/Diffusive Terms . . . . .	50
3.4	Vertical Discretization Scheme . . . . .	52
3.5	Horizontal Discretization Scheme . . . . .	55
3.5.1	Advection Terms . . . . .	56
3.5.2	Diffusion Terms . . . . .	58
3.6	Time Discretization/Integration Scheme . . . . .	59
3.6.1	Solution of Vertically Integrated Flow . . . . .	60
3.6.2	Solution of the Internal Modes . . . . .	64
3.7	Implementation . . . . .	66
<b>4</b>	<b>Barotropic Model Tests</b>	<b>68</b>
4.1	Stommel and Munk Single-Gyre Tests . . . . .	68
4.2	Isolated Vortex Tests . . . . .	71

4.3	Flow over an isolated Seamount . . . . .	73
4.4	Flow Over Fieberling Guyot . . . . .	73
4.4.1	Single Seamount Tests . . . . .	78
4.4.2	Three Seamount Tests . . . . .	81
4.4.3	Convergence Tests . . . . .	81
<b>5</b>	<b>Baroclinic Model Tests</b>	<b>89</b>
5.1	Single-Gyre Tests . . . . .	89
5.2	Channel Tests . . . . .	92
<b>6</b>	<b>Summary and Conclusions</b>	<b>99</b>
<b>A</b>	<b>The Dissipation of the Semi-Lagrangian Advection Scheme</b>	<b>111</b>
A.1	Introduction . . . . .	111
A.2	Amplification Factors . . . . .	112
A.3	Decay time scales and “equivalent” viscosity . . . . .	113
A.3.1	Long waves . . . . .	117
A.3.2	Short Waves . . . . .	119
A.4	Comparison to Other Dissipative Schemes . . . . .	121
A.4.1	Lax-Wendroff . . . . .	121
A.4.2	Matsuno (Euler-backward) . . . . .	122
A.5	Discussion . . . . .	123
A.5.1	Dependence on $\Delta t$ . . . . .	123
A.5.2	Dependence on $\Delta x$ . . . . .	125
A.5.3	Shallow-Water Equation Results . . . . .	126
A.5.4	Application to Ocean Models . . . . .	127
A.6	Summary . . . . .	128

<b>B</b>	<b>The Non-Interpolating Semi-Lagrangian Scheme</b>	<b>130</b>
<b>C</b>	<b>The Three-Dimensional Semi-Implicit Scheme</b>	<b>132</b>
C.1	Introduction . . . . .	132
C.2	Application to Shallow Water Equations . . . . .	132
C.3	Application to Three-Dimensional Equations . . . . .	134
C.4	Discussion . . . . .	136

# List of Tables

2.1	Percent phase speed errors for a linear advection problem. . . . .	14
2.2	Work requirements for phase accuracy at various orders . . . . .	20
3.1	List of Symbols . . . . .	46
5.1	Stability of test cases with topography . . . . .	95

# List of Figures

2.1	Depths of $s$ -levels in a sample basin . . . . .	27
2.2	Depths of $s$ -levels in a continental shelf area . . . . .	28
3.1	The Arakawa C-grid in a sample geometry . . . . .	56
4.1	SSH anomaly for Barotropic Stommel/Munk tests . . . . .	69
4.2	Meridional velocity in Western boundary current for Barotropic Stommel/Munk tests . . . . .	70
4.3	Sample SSH field for a nonlinear barotropic Stommel/Munk test .	72
4.4	Streamfunction of flow over strong topography . . . . .	74
4.5	Contours of depth for the idealized Fieberling Guyot test cases. .	76
4.6	Bathymetry for the Fieberling Guyot test cases with three seamounts.	77
4.7	Spinup characteristics of the barotropic flow over Fieberling Guyot.	79
4.8	Comparison of the sea-surface-height anomaly at day 100 for barotropic flow over Fieberling Guyot. . . . .	80
4.9	Barotropic response of the Fieberling Guyot at day 100. . . . .	82
4.10	Barotropic response of the Fieberling Guyot at day 150. . . . .	83
4.11	Sea-surface height at day 300 for the barotropic Fieberling Guyot experiment with three seamounts. . . . .	84

4.12	Anomaly of the SSH due to barotropic flow over three seamounts of the Fieberling Guyot chain at day 300. . . . .	85
4.13	Close-up of the important SSH anomaly contours for the barotropic flow over three seamounts on day 300. . . . .	86
4.14	Error norms of the Barotropic flow for the three-seamount case at various resolutions . . . . .	88
5.1	Temperature at 533 m at day 50 of a baroclinic single-gyre calculation. . . . .	91
5.2	Sections of three-dimensional flow over seamount at day 50 . . . . .	98
A.1	Decay time scale for linear interpolation . . . . .	114
A.2	Decay time scale for quadratic interpolation . . . . .	115
A.3	Decay time scale for cubic interpolation . . . . .	115
A.4	Decay time scale for quartic interpolation . . . . .	116
A.5	Effect of time step on damping . . . . .	125



# Chapter 1

## Introduction

The “Grand Challenge” of physical oceanography is the description of the large-scale flow of the world ocean and the understanding of its mesoscale variability. It has become increasingly clear in the last two decades that numerical simulations must play an irreplaceable role as a supplement to observations and analytic theory in this quest. Barring unexpected breakthroughs in remote sensing, observations will remain far too expensive to provide a truly comprehensive view of the state of the ocean for the foreseeable future. Analytical theories, though still a center of vitality of physical oceanography, are ultimately unable to attend to the level of detail required to understand the cumulative effects of nonlinearity and the complex basin geometry that are responsible for the richness of detail of the ocean circulation.

Numerical modelling occupies an ill-defined region between the traditional emphases of physical oceanography and the field of applied mathematics. Unlike the situation in meteorology and in the engineering sciences, oceanography is only slowly coming to accept the necessity of a significant investment of personnel and resources to acquire an expertise in the tools of applied mathematics and computational science pertinent to ocean modelling. The questions of consistency

and stability of the numerical methods have generally been treated rather well, but relatively little attention has been paid to the difficult problem of achieving and verifying convergence in realistic nonlinear simulations.

From a philosophical point of view, the use of a numerical model takes us two steps farther away from the ocean than analytic theories. We may view the hierarchy as:

1. The ocean.
2. The continuous model equations.
3. The discrete model equations.
4. The computer program.

To equate the output of the computer program with the solution of the discrete model requires the assumption that the computer program is correct, and that the finite-precision arithmetic does not introduce substantive errors. To equate the solution of the discrete model equations with the solution of the continuous model equations requires the assumption that the discrete system has converged. These assumptions are necessary before the physical question of the validity of the continuous model equations can be tested by comparison of the model output with observations. Therefore, this concern for convergence is not an abstract mathematical quest, but is directed at the very practical question of verifying that the output of the program is essentially the same as the solution of the continuous model equations.

Ocean models span a broad range of complexity, depending on the specific application. Although the same questions concerning the convergence of the numerical methods apply to all sets of continuous model equations, the current work

limits itself to the design and implementation of a three-dimensional primitive equation model. Special attention has been paid to maintaining consistent levels of truncation error in the differencing schemes, and to avoiding any *a priori* assumptions about the relative importance of the terms in the equations.

The model described here is among the most complex of ocean models, intended for detailed and realistic simulations of ocean flow. The complexity of the implementation of an ocean circulation model is not due only to the dynamics and physics of the primitive equations, but is increased by numerous considerations from numerical analysis and computational science. The calculations involved in a large-scale model require a very efficient use of computer resources in order to obtain answers with our necessarily limited resources. Although it may seem inelegant, the design of this model has been significantly affected by the state of the art of computer programming languages and computer architectures. This topic will be discussed in some detail in the next chapter.

The remainder of this chapter is devoted to a review of the various approaches to large-scale ocean modelling, and how the current work fits into the field as a whole.

## 1.1 Review of Large-Scale Ocean Modelling

The fundamental equations governing the flow of a fluid have been known since the last century. These Navier-Stokes equations are believed to be “correct” in the sense of properly accounting for the various physical forces which govern fluid motion, but they admit few useful analytic solutions and are computationally intractable for geophysically relevant flows. This intractability has led to the development of a sequence of approximations (based on scaling arguments) for

the fluid systems studied by various scientific and engineering disciplines.

### 1.1.1 The Primitive Equations

The beginning point for atmospheric and oceanic models are the so-called “Primitive Equations”. These equations are a relatively straightforward simplification of the Navier-Stokes equations in a rotating coordinate system, based on the scalings appropriate to large-scale oceanic and atmospheric motions. The equations are called “primitive” not because they are simplistic, but rather because few approximations have been applied to derive them.

The simplifications made to obtain the primitive equations are: the hydrostatic approximation; the Boussinesq approximation; the assumption of incompressibility; the approximation that the vertical component of the Coriolis force is negligible; and the assumption that the dissipative and diffusive processes can be parameterized in terms of large-scale variables.

The hydrostatic approximation is based on the observed fact that the large-scale flow in the ocean is in a very strong hydrostatic balance. Scaling analysis shows that the vertical pressure gradient is balanced by the local density to an accuracy of at least 3 decimal digits. This approximation, while very robust in terms of scaling, causes the most difficulty with numerical methods because it destroys the purely hyperbolic character of the Navier-Stokes equations. Because the equations are not hyperbolic, much of the extensive theory from numerical analysis and applied math is inapplicable. A consequence (discussed in Appendix C) is that it may not be possible to produce an unconditionally stable integration scheme.

The Boussinesq approximation states that density deviations may be ne-

glected except in calculating the pressure. This is a very accurate approximation in the ocean, though not in the atmosphere. It has the added benefit of linearizing many terms, and making the energy terms quadratic rather than cubic.

The assumption of incompressibility removes the fast compression (sound) waves from the equations. These are not believed to interact with the large-scale flow of the ocean. This assumption also destroys the purely hyperbolic character of the equations.

Finally, since the Coriolis force is neglected in the vertical momentum equations (due to the hydrostatic approximation), it is necessary to neglect the corresponding components in the horizontal momentum equations. This is required for energetic consistency, since the Coriolis force is not allowed to produce or destroy energy.

These approximations produce the “standard” primitive equations (Bryan, 1969; Semtner, 1986a). Many other decisions regarding physical parameterizations must also be made and will be discussed in the next chapter.

### **1.1.2 More Simplified Ocean Models**

Numerical models are used in two rather distinct roles in physical oceanography. First, they are used in “process studies” as an adjunct and enhancement to analytical studies of idealized geophysical fluid dynamical processes. Second, they are used in “simulation” to attempt to describe the state of the real ocean at some specific time.

Numerous simplifications of the primitive equations have been used in attempts to isolate and better understand various specific physical phenomena. Almost all of these simplifications can be grouped into two categories: simplifica-

tion of the dynamics, and simplification of the vertical structure. In this section I will briefly review the approaches and point out why the full three-dimensional primitive equations are necessary for a general-purpose model.

### **Simplifications of the Dynamics**

Two simplifications of the dynamics are commonly used: the linear primitive equations; or, a low-order perturbation expansion of the primitive equations about a geostrophic state.

Linearization of the equations is justified by the observation that much of the large-scale variability in the ocean can be described by linear wave dynamics. The linearized equations retain both the Rossby waves and the gravity waves, and have proven to be quite useful in the equatorial regions of the world ocean, where Kelvin wave and Rossby wave dynamics dominate the ocean's response to the wind (Busalacchi and O'Brien, 1980). The linearized equations fail, however, in strong currents (such as the western boundary currents of the oceans) in which nonlinear instabilities are important.

A perturbation expansion of the dynamics is based on the observed fact that the large-scale flow of the oceans is strongly geostrophically balanced. Thus the flow can be described as the sum of a geostrophic part and a small ageostrophic part. The most common schemes result from retaining zero, one, or two terms in the expansion. These choices yield the geostrophic, the general geostrophic, and a variety of balance equations, respectively.

Systematic analyses of the equations resulting from the retention of one term of the series expansion have been presented in (Williams, 1985; Cushman-Roisin, 1984). These "nearly-geostrophic" equations (which include the traditional quasi-

geostrophic approximation as a special case) appear to capture the important dynamics of the ocean in middle and high latitudes, but do not contain the Kelvin waves which are crucial to the equatorial ocean's dynamics. The question of how well these models handle the significant levels of nonlinearity in western boundary currents and strong eddies is still open, but it is not expected that these models will be useful for general-purpose simulations.

The retention of two terms in the Rossby number expansion of the primitive equations leads to a variety of balance equation models (McWilliams and Gent, 1980). The global balance equations of Gent and McWilliams (Gent and McWilliams, 1983) retain all the linear terms of the divergence equation as well as the first terms of the perturbation expansion of the vorticity equation. These equations have an approximation to the equatorial Kelvin waves, and so might be appropriate for large-scale simulations. It is too early to tell if these models capture enough of the important dynamics to serve as a general-purpose ocean model.

### **Simplification of the Vertical Structure**

Most large-scale models also include substantial simplifications to the vertical structure, based on the observed fact that most of the energy in the ocean is contained in the first two or three vertical modes.

A simple and useful approximation is the assumption that the ocean consists of two or more homogeneous, immiscible layers of fluid of different densities. This leads to the layer equations, which reduce the vertical degrees of freedom of the model to the number of layers.

Careful choice of the layer thicknesses and density contrasts can produce ac-

curate simulations of many regimes of the large-scale flow. However, there are significant difficulties with layered models when layers vanish or outcrop which render this scheme unsuitable for general-purpose calculations at the present time. Some progress has been made at applying stable numerical schemes to this problem (Bleck and Boudra, 1981; Bleck and Boudra, 1986; Bleck and Smith, 1989), but their accuracy is not yet validated. The more sophisticated front-tracking schemes applied in some engineering disciplines have not yet been applied in any substantial ocean calculations.

Another possible simplification of the vertical structure is the modal formulation. This allows continuous vertical variability of the flow variables by expanding the equations in terms of the eigenfunctions of the linear equations. The modal expansion allows more accurate representation of nonlinear interactions and topographic interactions than the layer formulation, but requires that the basic state be horizontally uniform. This scheme is therefore typically associated with the traditional quasigeostrophic approximation, and is not suitable for realistic, large-scale calculations.

## 1.2 The New Model - Background

The model described in the following chapters is a primitive equation model intended for realistic ocean simulations, or for process studies that require the full primitive equations. Combining the requirements of the research with the characteristics of the various approximations and numerical schemes sharply limits the choices available for the new model.

The requirements for a model to be able to run realistic simulations are:

- The model must be able to handle the full physics and thermodynam-



ics of the incompressible, Boussinesq, primitive equations. This excludes quasigeostrophic and balance equation models, and weighs against layered models.

- The model must be able to handle the observed irregular geometries of the oceans in both the horizontal and vertical directions. This excludes any reasonably easy spectral model, and causes severe difficulties for layered models.
- The model must use numerical schemes that are consistent with optimal performance on current high-performance computers. The model must additionally be able to make use of multiple processors. Versatility in this last regard is an advantage, since it is not yet clear what parallel architectures are going to be available in the near future.

The decisions on the design discussed below are very highly interdependent, so the order of discussion is somewhat arbitrary. A surprising aspect of this study has been the way that the special considerations of the various numerical techniques seem to fit together in only one way. Comments will be made where alternative techniques are possible — often, though, changing one decision causes the other decisions to be made unworkable, unhelpful, or unnecessary.

Interspersed through the discussion will be comparisons to the Bryan/Cox model (Bryan, 1969) (also known as the GFDL model). The current model formulation is specifically intended to remedy some of the shortcomings of the Bryan/Cox formulation, and to provide a tool that is most effective in those areas in which the numerics of the Bryan/Cox model are the weakest.

Throughout the design of the model, an overriding priority has been to pro-

duce a model which can be used to study the convergence of the numerical schemes being used. It is impossible to answer the scientific question, "Do these model equations adequately describe the ocean's flow?", if one does not have strong evidence that the solution of the *discrete* version of the equations has converged to the solution of the *continuous* model equations. It is hoped that this model will prove useful in beginning to address this major unknown aspect of ocean modelling.

# Chapter 2

## The New Model

In this section, I will discuss the major design decisions of the new ocean circulation model. The discussion will be technical, but not highly mathematical. The detailed derivations of the transformed and discretized governing equations are presented in the next chapter.

The heart of the model is contained in the options for the horizontal and vertical discretization. The strong vertical density stratification in the ocean, coupled with the large aspect ratio of the ocean geometry and forcing, produces a strong anisotropy in the ocean dynamics. Therefore, the “best” decisions for discretization in these two directions may not be identical. They are dealt with here separately.

### **2.1 Horizontal Discretization: FD vs FE vs Spectral**

Since the development of the first generation of ocean models in the late 1960's (Bryan, 1969), there has been a great deal of progress in the application of finite-element methods and spectral methods to fluid mechanical problems (Fletcher, 1984). Because of the current interest in these techniques, it is appropriate to

contrast these two techniques with the finite-difference method chosen here and show that the decision to continue with a finite-difference scheme was not a naive one.

The horizontal discretization chosen for the first version of the model uses standard second-order finite differences on a uniformly-spaced staggered grid (the Arakawa C-grid). The following subsections will present the rationale behind these decisions by comparing the finite-difference (FD) technique with the finite-element (FE) and spectral techniques in the following categories:

- Accuracy
  1. linear phase and group speed errors
  2. truncation errors
  3. conservation and aliasing errors
- Computational Efficiency
  1. Work Estimates
  2. Storage Requirements
  3. Vectorizability/Parallelizability

### **2.1.1 Accuracy**

There are many directions from which to view the differences between the accuracies of the finite-difference, finite-element, and spectral methods. One helpful viewpoint is to compare how the three methods make the inevitable tradeoff between resolution and accuracy for a fixed computational resource. In this context,

“resolution” refers to range of allowable wavelengths in the system, while “accuracy” refers to the truncation error in the estimation of derivatives. For a fixed computational resource, the usual second-order finite-difference method can be considered to yield the most resolution at the least accuracy. Conversely, for the same computational effort, global spectral methods yield the most accuracy but the least resolution. Finite-element and spectral-element methods occupy the middle ground.

The errors of finite-difference methods for hyperbolic-like problems are well known, though their cumulative effects are not always well understood. These errors can be conveniently divided into three categories: phase and group speed errors for the linear dynamics, truncation errors for the nonlinear dynamics, and conservation errors (including aliasing errors).

### **Linear Phase Errors**

Phase speed errors in second-order finite-difference methods are scale dependent, and are typically quite severe for waves with wavelengths of less than about 8 times the grid scale. Errors decay to about 1% for waves with 20 grid intervals per wavelength (Haltiner and Williams, 1979; Grotjahn and O’Brien, 1976). Increasing the order of the scheme can decrease the magnitude of these errors considerably as shown in Table 2.1. The compact-differencing schemes (Chang and Shirer, 1985; Haltiner and Williams, 1979) are especially accurate for phase speeds. Finite-element methods exhibit the same pattern of phase speed errors as the finite-difference compact-differencing schemes since they are mathematically identical in one dimension. Spectral methods, on the other hand, give essentially exact results for linear wave phase speeds. The errors are ameliorated in finite-

	$3\Delta x$	$4\Delta x$	$6\Delta x$	$8\Delta x$
Second order	59%	36%	17%	9%
Fourth order	39%	15%	4%	1%
Fourth order compact	17%	4%	1%	< 1%
Spectral collocation	$\approx 0\%$	$\approx 0\%$	$\approx 0\%$	$\approx 0\%$

Table 2.1: Percent phase speed errors for a linear advection problem. Results are shown at various wavelengths for second-order, fourth-order, and spectral schemes with exact time differencing.

difference models by adding sufficient diffusion to the system to strongly damp the waves in the 2–4 grid interval range.

### Truncation Errors in Nonlinear Terms

Truncation errors in nonlinear advection arise from the same numerical source as linear wave phase speed errors, but the results are interpreted differently from a dynamical point of view. The primary advantage usually cited for spectral techniques is the spectral convergence of the solution as the resolution is increased. This is clearly going to be important for simulations in which high accuracy is required. What is not known is whether or not very high accuracy is needed in ocean simulations. As a numerical example, spectral convergence is likely to be crucial if one desires accuracy of five or more significant digits in the solution. If only a few digits of accuracy is needed, then second- and fourth-order finite-difference schemes can provide adequate convergence rates.

With regard to the accuracy of ocean models, the traditional thinking has often been that since the forcing functions are known to be only approximate, and since the dynamics are known to be truncated, there is no need for highly accurate numerical techniques. This approach is reasonable for linear, steady-state problems, but is invalid with nonlinear time-dependent problems. There is

no *a priori* way to determine the effects of small errors on the long-term behavior of nonlinear systems.

### Conservation Properties

Conservation of integral invariants in ocean models has two aspects. The first is bulk conservation of quantities such as mass and energy, and the second is nonlinear aliasing of energy and enstrophy from the short waves back into the long waves.

The need for bulk conservation of integral invariants is an open issue with respect to ocean models. The conservation of linear quantities (mass and momentum) and quadratic quantities (energy and enstrophy) is usually considered to be “a good thing”, but (modest) explicit damping (which destroys such conservation) is not usually considered to be a major problem. The numerical scheme must not lose so much energy that the flow fields are significantly decelerated, but small variations do not seem important.

The more important problem concerns aliasing. It is widely held that conservation of energy and potential enstrophy are important for (at least) the horizontal discretization in large-scale models. A lack of conservation of energy and enstrophy both removes energy from the short waves (which are actively engaged in nonlinear processes) and puts it (incorrectly) into long waves which should not be participating. A lack of conservation of potential enstrophy is often associated with numerical instabilities in nonlinear models. This forces the modeller to apply more explicit damping to maintain stability. In strongly nonlinear cases (such as modelling of western boundary currents and ring formation) this extra damping can completely change the character of the solutions. In less nonlin-

ear cases, the solutions appear to be less sensitive to both the damping and the conservation properties.

For the quadratic nonlinearities of the primitive equations, the problem of aliasing in finite-difference models can be overcome if the 2–3 grid-length waves are filtered out of the solution at every time step (Orszag, 1971). The addition of scale-selective dissipation to the system tends to accomplish the same result, though without 100% effectiveness.

Finite-element methods for fluid mechanical problems are usually derived by a Galerkin procedure, which guarantees freedom from aliasing. Galerkin spectral methods are also free of aliasing, though they are too expensive to apply directly, and approximately dealiased schemes are usually used. Spectral collocation methods are not guaranteed free of aliasing, but typically show very little in well-resolved simulations.

Both second-order and pseudo-fourth-order finite-difference schemes for the Arakawa C-grid have been developed that conserve energy and enstrophy (Abramopoulos, 1988; Takano and Wurtele, 1982). (Pseudo-fourth-order schemes are fourth-order accurate only for the non-divergent part of the flow). For problems involving nonlinear instability, the conservation properties appear important, while for stable, quasilinear problems, the Taylor series accuracy of the scheme is more important. There are significant unanswered questions in this area, especially comparing the relative importance of phase errors and conservation errors. For non-linear problems, the phase relationship of the waves making up a field is clearly going to be important, and finite-difference schemes typically produce significant phase errors. This line of reasoning appears inconsistent with the more common thinking that conservation properties are more important, but



is in agreement with the good performance of the semi-Lagrangian advection schemes used in atmospheric models (see Appendix A).

### 2.1.2 Computational Efficiency

The balancing consideration to the accuracy discussed in the previous section is computational efficiency. The primary drawback of the finite-element and spectral methods is their excessive computational cost when applied to realistic problems in irregular domains.

For use in irregular domains, spectral methods require transformation of the coordinate system into a logically rectangular box so that Fast Fourier Transforms (FFT's) can be used to calculate the derivatives. These coordinate transformations can be quite complicated and difficult to derive for realistic ocean geometries, and the extra metric terms in the equations add substantially to the total work requirement. For domains that are multiply-connected, the domain must be decomposed to produce a set of singly-connected domains, which then must be patched together.

The time step restriction on a Chebyshev collocation method is proportional to  $N^2$  (where  $N$  is the number of collocation points in each direction), due to the quadratic convergence of the collocation points at the ends of the domain. Thus, doubling the resolution requires four times as many time steps, compared to twice as many for finite-difference techniques. The variable grid spacing exacerbates this problem, in that the stability limitation is based on the smallest grid distance in the entire domain. If an implicit integration scheme is used to overcome this time step limitation, the structure of the matrices is such that fast (*e.g.* FFT) techniques cannot be used.

The current “state-of-the-art” approach to spectral models is the “spectral element” technique. The spectral element technique divides the domain into a number of subdomains, then uses standard spectral interpolation scheme within each subdomain. This technique has two advantages over the globally interpolating schemes: first, the domain does not need to be so severely distorted, since awkward pieces can be put in separate domains; and second, higher accuracy can be obtained with only a linear increase in the number of time steps required by increasing the number of domains (with the same order interpolation inside each). A disadvantage of this scheme is that the matrix equations are even less regular than in the global spectral technique.

The efficiency concerns are quite similar for finite-element techniques. Although the mapping of the governing equations can be replaced by the construction of a nonuniform mesh, the sparse matrix equations that must be solved to calculate the derivatives have irregular structures and must be solved by slow direct or iterative matrix techniques. Direct techniques have work requirements of  $O(N^3)$  operations for each derivative calculation at all the points of an  $N \times N$  grid. By contrast, the derivative calculations in finite difference methods scale linearly with the number of grid points, and so require only  $O(N^2)$  operations for estimating the derivative at all the points of the same  $N \times N$  grid. Since for a large-scale ocean calculation,  $N$  will be in the range of 100–600, the extra factor of  $N$  in work can be prohibitive. The compact finite-difference schemes require the solution of tridiagonal systems for the evaluation of derivatives, which requires  $O(1)$  operations at each grid point, for a total of  $O(N^2)$  operations.

The memory requirements of the finite-element schemes are perhaps more constraining than the work requirements. A simple finite-element scheme for a

two-dimensional problem requires  $O(N^3)$  storage locations for each of the pre-factorized matrices used for calculating derivatives along the coordinate axes. Since this matrix must be accessed at least once per time step, it must be stored in fast local memory.

Some progress has been made at improving the performance of sparse matrix solvers on supercomputers (Duff and Reid, 1983; Duff and Reid, 1984), but the codes are complex and the efficiency is still not comparable to the explicit derivative calculations in the finite-difference equations. Much of the effort in sparse matrix calculations has been directed toward the solution of very large systems of equations one time, rather than toward the repeated solution of one moderately large system, as would arise with a time-stepping ocean model.

The computational efficiency issue is mitigated somewhat by the need for fewer grid points, and on a simple operation-count comparison, the higher-order schemes appear competitive. However, because of its regular structure, the finite-difference scheme is much more highly vectorizable than the others, and this advantage skews the results in favor of the finite-difference schemes.

As an example problem, consider the linear hyperbolic problem:

$$\frac{\partial u}{\partial t} + c \frac{\partial u}{\partial x} = 0.$$

Table 2.2 compares the work requirements of several techniques to obtain a phase error of less than 10% when advecting the solution over  $j$  periods. This work estimate includes the number of grid points per wavelength, the number of operations per step per gridpoint, and the number of steps necessary to advect the solution over each period. For the compact-differencing schemes, the work estimates have been adjusted to count unavoidable floating-point division operations as 6 operations. This correction reflects the actual time required to perform

Order	N	Work	# steps	Total Work	Comments
2	$20j^{\frac{1}{2}}$	3	1	$60j^{\frac{1}{2}}$	2nd-order FD
4	$7j^{\frac{1}{4}}$	6	$\frac{4}{3}$	$30j^{\frac{1}{4}}$	4th-order 5-point FD
4	$4j^{\frac{1}{4}}$	16	$\frac{5}{3}$	$100j^{\frac{1}{4}}$	Compact 4th-order FD
6	$5j^{\frac{1}{6}}$	10	$\approx 2$	$100j^{\frac{1}{6}}$	6th-order 7-point FD
6	$3j^{\frac{1}{6}}$	21	$\approx 2$	$120j^{\frac{1}{6}}$	Compact 6th-order FD

Table 2.2: Work requirements for a simple linear hyperbolic problem at various discretization orders. The requirement is for 10% phase accuracy after  $j$  periods of advection. N is the number of grid-points per wavelength, Work is the equivalent number of floating-point operations, # steps is the relative number of time steps required, and Total Work is the product of these. The data is extracted from (Kreiss and Oliger, 1973; Chang and Shiner, 1985; Haltiner and Williams, 1979).

division on most current computers, and shifts the estimate of the most efficient scheme to the wide-stencil fourth-order discretization.

Work estimates for spectral schemes would be difficult to fit into the format of Table 2.2 since the time stepping schemes and work estimates are so different. The Tchebyshev collocation scheme requires only 3 collocation points per wavelength to obtain essentially exact phase response for the sample problem. The work required is of the order of  $10N \log_2 N + 2N$  operations for each evaluation of the right-hand-side of the equation in the time-marching scheme. The time step is proportional to  $N^2$ , but the constant of proportionality depends on the time marching scheme chosen and the exact physics of the problem.

The characteristics of current computer architectures also figure prominently in the estimates of the work and computational efficiency of the various schemes. The fastest available computers are now either shared-memory, moderately parallel vector computers (as in the Cray machines) or the massively parallel, single-instruction-multiple-data (SIMD) machines (exemplified by the Thinking Machines Corporation's Connection Machine). The shared-memory vector machines

are considerably more versatile with respect to the range of algorithms that may be efficiently employed, but the massively-parallel machines should provide an easier growth path for scaling to higher performance. The massively parallel machines are not well-suited for schemes like the compact-difference method, for example, because not enough of the tridiagonal systems need to be solved at once to keep all of the processors busy. Standard or wide-stencil finite-difference schemes will run very efficiently on the massively parallel machines, however.

### 2.1.3 Discussion

The basic question is whether the enhanced accuracy of the spectral, finite-element, and higher-order finite-difference methods is more important than the loss of the short waves in the spectrum (since the higher-order schemes will not be able to achieve the same resolution for the same amount of computational effort). In the atmosphere, studies have shown that a change from second-order to fourth-order differencing can improve the forecast skill of a weather model more efficiently than an increase of a factor of two in resolution (Williamson and Browning, 1973). Further studies have shown that most of the advantage of the fourth-order scheme can be obtained by applying it only to the nonlinear advection terms, leaving the terms controlling the linear wave dynamics at second-order accuracy (Campana, 1979).

For linear problems, the effect of spectral truncation on the solution is obvious — the short waves are simply removed, and the long waves are unaffected. For nonlinear problems, however, all wavelengths interact, and there is no way (short of “brute force” experimentation) to determine how the truncation of the spectrum will effect the solution.

In light of this, it is not at all clear where the “best” balance lies in the tradeoff of resolution vs. accuracy. The theory for linear problems is well-developed (Kreiss and Oliger, 1973), but for nonlinear problems, theory does not take one very far, and substantial experimentation must be done on the system of interest in the parameter range of interest in order to begin to be able to formulate a quantitative answer to this problem.

Because of this significant uncertainty it was decided to retain the finite-difference approach used in current models. Although the newer techniques may eventually prove superior in the ocean context, they should be tested in more specialized codes — not in a new general-purpose model. The work that is currently being done in this area has been either for simple geometries (LeProvost, 1986; Jensen and Kopriva, 1988), or for coastal, limited-domain models (Davies, 1987).

The initial version of the model uses standard second-order accurate finite-differencing schemes in the horizontal directions. The design of the model allows the replacement of the horizontal derivatives with a higher-order or more conservative scheme without excessive difficulty. In particular, the “compact differencing” scheme can be used to obtain fourth-order accurate derivative estimates using the same stencil as the second-order schemes and requiring no additional (unphysical) boundary conditions.

#### **2.1.4 The Arakawa C-grid**

Oceanic and atmospheric models have traditionally used staggered grids for the horizontal distribution of variables. Earlier ocean models have chosen the Arakawa B-grid in order to facilitate an implicit treatment of the Coriolis terms, and have

retained it because it has been thought that it performs better than the C-grid when the relevant radius of deformation is not resolved. In addition, several researchers have attempted to produce C-grid models, but have given up due to excessive noise in the higher vertical modes (Semtner, 1986b). This model addresses that problem by a change in the vertical discretization, as will be discussed in the next section.

For this model, the Arakawa C-grid was chosen because both gravity waves and planetary waves on the C-grid mimic the characteristics of the continuous solutions better than those on the B-grid whenever the radius of deformation is resolved (Wajsowicz, 1986). If the radius of deformation is not resolved, then neither grid gives good results, but it is difficult to decide which is better (or worse). This model is intended to be run in high-resolution simulations, as it is not reasonable to expect good results from *any* model if the baroclinic radius of deformation is not resolved.

## 2.2 Vertical Discretization

The primary new features of this model pertain to the vertical discretization, and are intended to remedy the major shortcomings of the models based on the Bryan/Cox/GFDL formulation. The GFDL model uses standard finite-differences in the vertical, and moves the bottom to the closest vertical velocity point. The grid is generally chosen to be non-uniform, with much tighter grid spacing in the upper layer of the ocean. Two substantial difficulties arise with this scheme. First, the non-uniform grid spacing means that many of the vertical derivative calculations are not centered, and are therefore of first-order accuracy. This decreases the accuracy of the simulation of both vertical advection and ver-

tical diffusion processes. Second, the quantization of allowed depths drastically alters slopes in the bottom topography. This has a strong impact on the wave dynamics by concentrating the topographic  $\beta$ -effect and nonlinear vertical mode interactions of broad sloping regions into discrete, narrow bands, rather than allowing the continuous spatial dependence. The combination of these two factors makes a large number of vertical levels necessary. This increases the requirements for computational effort, execution-time storage, and storage of archival data.

### 2.2.1 Coordinate System

To avoid the topography problem, the new model uses a boundary-fitted vertical coordinate — in the style of the “*sigma-coordinate*” scheme popular in meteorology. The vertical variable is replaced by a scaled variable whose value is 0 at the bottom of the ocean and 1 at the surface. Thus the bottom topography is continuous and has a continuously variable slope.

To avoid the problem of the loss of accuracy in the non-uniform grid, an analytic stretching is applied which allows uniform increments in the transformed variable to correspond to nonuniform increments in the old variable (Kalnay de Rivas, 1972). A stretching function has been derived which allows increased resolution in the upper ocean (and optionally in the bottom boundary layer) while still retaining the advantages of a uniform grid in the vertical variable.

A novel feature of the stretching function used here is that the degree of non-linearity of the transformation is a function of the local depth. The full stretching is only applied in the limit as the ratio of the local depth to the minimum depth becomes large. As the minimum depth is approached, the transformation becomes linear (which produces uniform vertical grid-spacing). This feature is



needed to prevent the levels from getting too close together and causing time step restrictions associated with vertical advection and diffusion to become important.

The stretching function used in the model is

$$\frac{z}{D} = -(1-s) \left[ 1 - \left( 1 - \frac{D_0}{D} \right) s \right], \quad (2.1)$$

where  $z$  is the vertical location,  $D$  is the depth of the bottom,  $D_0$  is a scaling parameter,  $s$  is the new vertical coordinate. The scaling parameter  $D_0$  must be chosen to be less than or equal to the minimum depth in the domain, and it determines the depth at which the stretching function is linear.

For shallow water, the equation tends to

$$\frac{z}{D} = -(1-s),$$

while in deep water ( $D \gg D_0$ ), the equation tends to

$$\frac{z}{D} = -(1-s)^2.$$

To make the upper level as uniform as possible in thickness, the scheme has the property that the metric term is independent of the topography at the surface

$$\frac{\partial z}{\partial s} = D_0, \quad \text{at } z = 0.$$

The depths of fixed  $s$ -levels in an 11-level discretization are shown in Figs. 2.1-2.2. The whole range of depth values are shown in Fig. 2.1, while Fig. 2.2 shows how the stretching becomes uniform in shallow water. If desired, the stretching function can be shifted to produce higher resolution near the top and bottom with least resolution in the middle depths.

The quadratic stretching function used fits nicely with the linear finite-element scheme (discussed below) since the vertical derivative of the stretching function is

linear just like the basis functions. If a user desires a higher-order stretching function, then the subroutines which calculate the vertical integrals in the Galerkin finite-element scheme must be replaced with more sophisticated versions. In particular, the stretching function should be a polynomial, since this allows the use of efficient Gauss-Lobatto quadrature schemes for the vertical integrals.

The sigma-coordinate system has not been used very often in oceanographic models. A potential problem with sigma-coordinate models is that, in the presence of topography, the pressure gradient term in the momentum equations splits into two terms. One term is the pressure gradient along surfaces of constant  $s$ , and the other is a correction term proportional to density and the gradient of the topography. A recent note by Batteen (Batteen, 1988), as well as experience with this model, suggests that the subtraction of the mean density and its associated hydrostatic pressure from the equations of motion can greatly decrease the noise generated by topography with this scheme. When topography interacts with strong stratification, the problems become very severe and there is not yet a satisfactory solution available. This will be discussed in chapters 4 and 5.

### **2.2.2 Linear, Galerkin Finite-Element Scheme**

Recent experience in atmospheric modelling has suggested the superiority of the finite-element technique for vertical representation (Beland et al., 1983; Hartmann, 1988). Based on this, the new model employs linear Galerkin finite elements instead of the usual finite differences. The linear Galerkin finite element scheme produces the same matrix equations (with tridiagonal matrices) as the fourth-order compact differencing scheme also occasionally used in atmospheric models (Haltiner and Williams, 1979). We expect that this fourth-order accurate

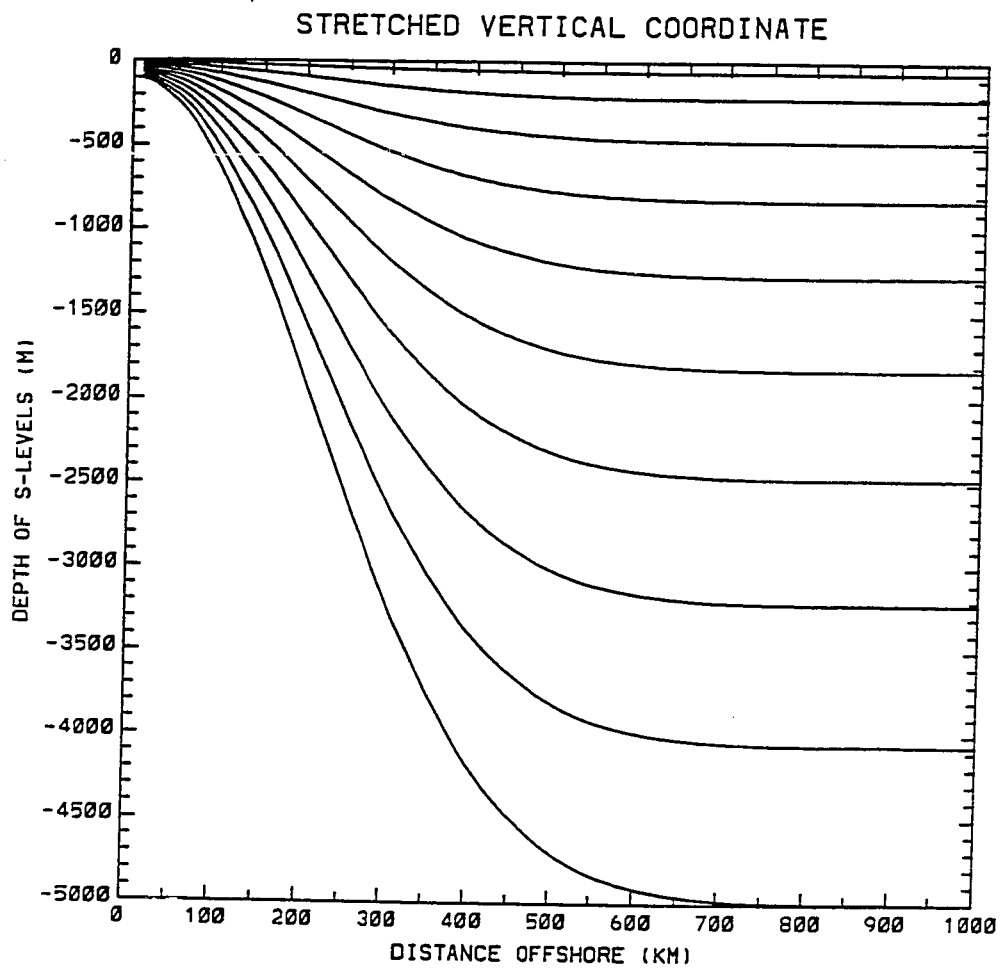


Figure 2.1: Depths of uniformly-spaced s-levels in an 11-level discretization of a sample ocean basin.

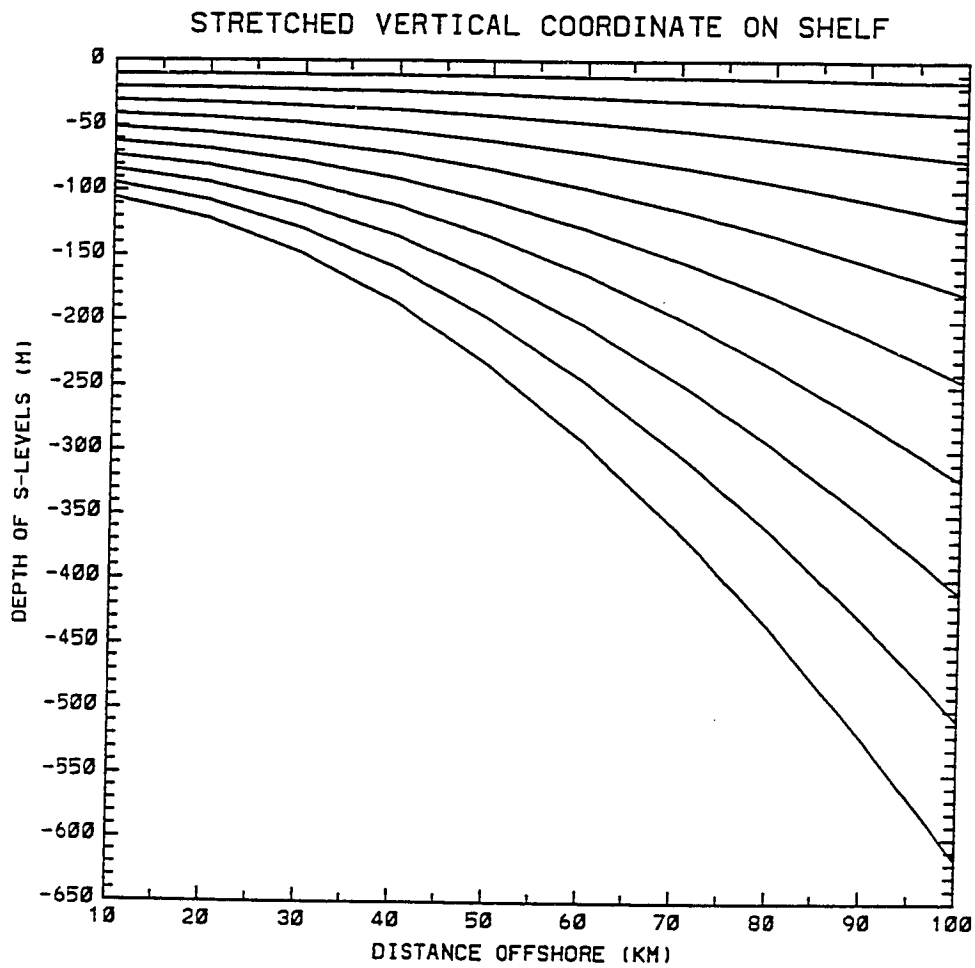


Figure 2.2: Depths of uniformly-spaced *s*-levels in the continental shelf area of the 11-level discretization of a sample ocean basin.

scheme, with continuously variable bottom topography, will greatly increase the accuracy of the model, or allow adequately accurate simulations to be run with significantly fewer grid points in the vertical. This superiority of the finite-element scheme has been demonstrated for an atmospheric problem by Hartmann (Hartmann, 1988). His results point out that the finite element scheme is especially useful for coarse vertical resolution of nonlinear instability processes.

The experience with respect to conservation properties for the horizontal discretization may not apply to the vertical discretization. Counterexamples to the rule "conservative is better" exist in the literature, based on the fact that conservative schemes have larger truncation errors than their non-conservative counterparts with the same order of accuracy. Williamson (Williamson, 1988) demonstrated that a nonconservative vertical discretization gave better results in the NCAR community climate model than a discretization which conserved energy. Cullen (Cullen, 1979) showed that the conservative finite-element scheme for advection produces much larger errors for short waves than a non-conservative version.

There is an added benefit to the use of a higher-order scheme in the vertical direction. By reducing the number of vertical nodes, the number of vertical modes present is reduced, and those modes that are present are treated much more accurately. It is hoped that this removal of the higher modes (which have poorly resolved horizontal radii of deformation) will alleviate much of the trouble experienced by previous modellers with the C-grid (Semtner, 1986b).

Another minor point related to the vertical discretization is the treatment of the upper boundary condition. This model applies a free-surface condition, as opposed to the rigid-lid approximation more commonly used. This will be

discussed in the section on the time integration of the gravity waves and in the section on the solution of the elliptic equation for pressure.

## 2.3 Time Integration Schemes

Given the conflicting requirements for high resolution and computational efficiency in ocean models, it is imperative to use the most efficient time integration scheme possible. For atmospheric models, typical scaling arguments suggest that time differencing errors are a factor of 40 or more smaller than spatial differencing errors for large-scale meteorological motions (McDonald, 1986).

The primitive equations can be considered to be composed of a hyperbolic part (consisting of the advection and gravity wave terms) and a parabolic part (consisting of the horizontal and vertical diffusion terms). The integration schemes for each of these four parts will be treated separately here.

### 2.3.1 Advection Schemes

Several time integration schemes were investigated for possible application in this model. The results were occasionally surprising, and point out the need for care in the application of numerical schemes used in atmospheric models to the ocean. The semi-Lagrangian scheme (which is an unconditionally stable method for handling the advective terms) was tested and shown to contain excessive implicit dissipation (McCalpin, 1988). This reference is reproduced in appendix A.

Ritchie (Ritchie, 1986) has developed a non-dissipative version of the semi-Lagrangian scheme which has been applied successfully to atmospheric models. In appendix B, this non-interpolating semi-Lagrangian scheme is shown to provide no benefit in time step in the ocean without the use of the semi-implicit scheme

(which is dismissed below).

After dismissing these two current approaches, it was decided to retain the standard Eulerian approach. The model currently employs the “quadratic averaging” scheme to help with stability, but it would not be a major effort to replace these terms with a more sophisticated differencing scheme.

### **2.3.2 Gravity Waves**

The large density contrast between the ocean and atmosphere causes a large ratio in the phase speeds of the external and internal gravity waves. Therefore models have traditionally treated these waves separately, with some sort of implicit treatment on the barotropic mode and explicit treatment of the baroclinic modes.

#### **Baroclinic Modes**

An earlier formulation of this model attempted to treat all the vertical modes implicitly, using the three-dimensional semi-implicit scheme (Robert et al., 1972). The scheme was shown to be physically ill-posed when applied to the stratification present in the ocean (McCalpin, 1989) — see appendix C.

It may be possible to produce a model that treats the first several internal modes implicitly and the rest explicitly, but the implicit scheme maintains stability by slowing down the fastest waves in the system. If the first internal mode gravity waves are important, the semi-implicit scheme will produce large phase errors. The equatorial Kelvin waves are the primary concern here. Since these waves are crucial to equatorial dynamics, the semi-implicit approach is unacceptable here. In the new model, the baroclinic gravity waves are treated explicitly.

## Barotropic Mode

The external waves travel at some  $200 \text{ m s}^{-1}$ , compared to  $3\text{--}5 \text{ m s}^{-1}$  for the fastest internal waves. Therefore, for numerical stability, it is necessary to handle the external gravity modes in some special way.

A standard approach (applied in the Bryan/Cox and Haidvogel models) is to apply the “rigid-lid” upper boundary condition. This condition prohibits vertical motion at the sea surface, and forces the vertically integrated flow to be non-divergent. External gravity waves do not exist in this system, so the stability requirement is substantially relaxed. Unfortunately, the physics are also slightly distorted. In addition to removing the external gravity waves from the system, the rigid lid also eliminates vortex stretching in the barotropic vorticity equation. The vortex stretching term affects the phase speed of long waves, causing them to slow down as the external radius of deformation scale is reached. In mid-latitude oceans, the barotropic radius of deformation is typically the basin scale (or large), so it is a good approximation to neglect this term. In the Southern Ocean, however, the external radius of deformation decreases to under 2000 km, and it is possible for significant energy to exist in barotropic waves of this scale. There are no published studies of the impact of such phase errors on large-scale simulations.

An alternative technique is the semi-implicit scheme, used here. In this scheme, the terms responsible for the external gravity waves (the external pressure gradient and the vertically integrated horizontal divergence) are treated implicitly by averaging in time. The barotropic part of the pressure gradient actually contains two parts: that due to the free surface anomaly, and that due to the mean of the vertically averaged perturbation pressure gradient. This scheme



only treats the sea surface anomaly implicitly (Madala and Piacsek, 1977), since that is the part of the solution which moves at the external gravity wave phase speed. The vertical mean of the perturbation pressure gradient is due to a depth-independent density perturbations which evolve on advective time scales and so do not require the implicit treatment.

The semi-implicit approach is appropriate for calculations for which the speed of the external gravity waves is not important. For simulations involving tides or tsunamis, the barotropic mode may be calculated explicitly (asynchronously) using a shorter time step. The current version of the code contains the semi-implicit scheme, but the explicit/decoupled scheme can be installed in a few hours. Of course, the entire model can be run explicitly with a very short time step. In this case, the barotropic flow is calculated with the baroclinic flow. This modification is trivial, but the resulting code would be rather expensive to run.

### 2.3.3 Horizontal Diffusion

The leap-frog technique which is so successful for the hyperbolic part of the primitive equations is unconditionally unstable for the parabolic part. Many models avoid the stability difficulty by simply calculating the diffusion terms at the oldest time level of the 3-time-level leapfrog scheme. This technique is stable for

$$\frac{A_H \Delta t}{\Delta x^2} \leq \frac{1}{4}.$$

For values of  $A_H$ ,  $\Delta t$ , and  $\Delta x$  typical of ocean simulations, this condition is much less restrictive on the time step than the restrictions due to advection and gravity wave propagation.

A difficulty of this scheme is that it is only first-order accurate in time. The

alternative used here is the duFort-Frankel scheme. This scheme is implicit in that one term is time-averaged, but the time-averaged term is not differentiated, so the scheme can be solved directly, without the need for any matrix inversion.

A careful analysis of the scheme shows that the truncation error is of the form (Haltiner and Williams, 1979)

$$O(\Delta t^2) + O(\Delta x^2) + O\left(\frac{\Delta t}{\Delta x^2}\right).$$

Therefore the scheme requires

$$\frac{A_H \Delta t}{\Delta x^2} \ll 1$$

for consistency. A typical set of values for use in high-resolution ocean models would be  $A_H = 1000 \text{ m}^2\text{s}^{-1}$ ,  $\Delta t = 2000 \text{ s}$ , and  $\Delta x = 10000 \text{ m}$ , producing

$$\frac{A_H \Delta t}{\Delta x^2} \approx 0.02,$$

which ensures the consistency of the scheme. For higher-resolution cases typical parameters would be  $\Delta x = 1000 \text{ m}$ ,  $A_H = 20 \text{ m}^2\text{s}^{-1}$ ,  $\Delta t = 200 \text{ s}$ , producing even smaller values of this error term.

If the formulation of the model includes a full tensor form of the diffusion (discussed in a later section), then the diagonal elements corresponding to horizontal momentum fluxes should be treated with the Dufort-Frankel scheme as described here. The off-diagonal elements (containing the cross derivatives) are likely to be very small corrections, and can be treated either explicitly (in which case the unconditional instability is unlikely to show up) or by lagging in time.

### 2.3.4 Vertical Diffusion

The vertical diffusion in the model is treated with a constant vertical eddy viscosity,  $K$ . A general implicit integration scheme is employed of the form

$$\theta K \left( \frac{\partial^2 u}{\partial z^2} \right)^{n+1} + (1 - \theta) K \left( \frac{\partial^2 u}{\partial z^2} \right)^{n-1}, \quad (2.2)$$

where  $\theta$  is a time-differencing control parameter which the user may set to be between zero and one. For  $\theta \geq \frac{1}{2}$ , the scheme is unconditionally stable, while for  $\theta \leq \frac{1}{2}$ , the scheme is conditionally stable. For  $\theta = \frac{1}{2}$ , this is the Crank-Nicholson scheme, which is second-order accurate in time, otherwise it is only first-order accurate in time. For  $\theta = 0$ , the scheme is explicit and conditionally stable.

The Crank-Nicholson scheme is generally preferred, except that it has the property that waves which have wavelengths of  $2\Delta t$  and  $2\Delta z$  are not damped. Since a major function of the viscous terms is to remove the  $2\Delta z$  waves, a value of  $\theta$  slightly greater than  $\frac{1}{2}$  is desired. This choice combines “almost-second-order” accuracy in time with damping of all short wavelengths.

The tridiagonal system of equations which results from any choice of  $\theta > 0$  is combined with the tridiagonal system which must be solved for the vertical derivatives in the finite-element scheme, and so adds essentially no work to the model.

The combination of the uniformly-spaced finite-element grid and the nonlinear coordinate transformation produces a fourth-order accurate scheme. This should provide significantly more reliable results than the first-order accurate schemes in current use.

### 2.3.5 Coriolis Terms

The Coriolis terms must be explicit on the C-grid, since an implicit treatment produces a pentadiagonal system of equations to solve at each time step. This imposes a stability restriction of

$$\Delta t \leq \frac{2}{f},$$

where  $f$  is the Coriolis parameter. This time step restriction is much less restrictive than those due to advection and gravity waves, allowing time steps of almost 4 hours in the most restrictive case.

## 2.4 Physics

Any model of a large-scale fluid system must parameterize unresolved processes. In this model, as in many others, the choices for these parameterizations do not significantly affect the choice of the differencing schemes and are often easily replaceable. Despite this, the importance of these parameterizations must not be played down. The following sections discuss the choices made for the initial version of the model.

### 2.4.1 Diffusive and Dissipative Processes

The modelling of sub-grid-scale diffusion/dissipation is one of the most subjective aspects of large-scale ocean simulations. Vertical diffusion has been the subject of intense study in recent years (Peters et al., 1988; Gargett, 1986), and some progress is being made at its parameterization. For horizontal diffusion, the case is not so clear. In fact, for some high-resolution simulations, it is possible that zero horizontal diffusion is an appropriate approximation.

### Vertical Diffusion

Most models of vertical diffusion attempt to apply some results from turbulence theory. For the upper tropical ocean, a vertical eddy diffusivity based on the Richardson number provides a good fit to the data (Peters et al., 1988). The Richardson number is the ratio of the square of the vertical density gradient to to the square of the vertical shear of the horizontal velocity. When this ratio is small ( $< 1/4$ ), the mixing is turbulent and the vertical eddy viscosity becomes as large as  $10^{-2}$ – $10^{-3}$   $\text{m}^2\text{s}^{-1}$ . For larger Richardson numbers, the mixing is much slower, with vertical eddy viscosities in the  $10^{-4}$ – $10^{-5}$   $\text{m}^2\text{s}^{-1}$  range.

### Horizontal Diffusion

Horizontal diffusion in most numerical simulations exists more to remove energy from the poorly resolved wavelengths in the system than to model the sub-grid-scale turbulent diffusion. The initial version of the new model assumes a uniform Laplacian eddy viscosity. This could be replaced with a biharmonic formulation, but there are several alternative approaches which should be considered: for example, the periodic application of a very sharp filter, or the introduction of a nonlinear viscosity parameterization based on two-dimensional geostrophic turbulence theories (Leith, 1968; O'Brien, 1986a).

### Isopycnal/Diapycnal Diffusion Tensor

It is becoming increasingly recognized that it is important to have the diffusion tensor in ocean simulations oriented with its major axes along isopycnals and its minor axis normal to the isopycnals. The derivation of a coordinate rotation to transform the tensor from isopycnal coordinates (where its form is assumed to be

known) to Cartesian coordinates (which most models work in) was presented by Redi (Redi, 1982), and simplified by Cox (Cox, 1987).

The isopycnal formulation of the diffusion tensor is often presented as being necessary to correctly model the diffusion due to mesoscale eddies in a non-eddy-resolving model. It is true that it is needed there, but it is also needed whenever the slope of isopycnals exceeds the ratio of vertical to horizontal diffusivity. This occurs at many scales, and the application of the standard horizontal/vertical mixing thereby produces excessively strong diapycnal mixing. Another side effect is that the non-rotated version contains insufficient vertical mixing in the case when an isopycnal occupies a large range of depths.

Mellor and Blumberg (Mellor and Blumberg, 1985) have examined the problem of diffusion in their sigma-coordinate model. They implemented a flux form of the diffusion in sigma coordinates which did not damage the representation of the bottom boundary layer.

### **2.4.2 Convective Adjustment**

The primitive equations contain the assumption that the flow is hydrostatic. In situations in which the vertical density gradient becomes positive (dense water overlying less dense water), the system is statically unstable and responds by a nonhydrostatic convective adjustment process. In the current model, this is implemented by locally increasing the vertical viscosity coefficient to about  $10 \text{ m}^2\text{s}^{-1}$ , or about 10000 times a typical large value. This quickly allows the vertical density field to adjust. Since the vertical diffusion is handled with an implicit scheme numerically, there is no trouble with exceeding the vertical diffusive stability criterion.

A technique used in earlier models was to vertically average adjacent densities repeatedly until a statically stable profile was obtained. This technique works, but is awkward, since it may need to be iterated. It is also considered to produce more spurious gravity wave energy than the enhanced diffusion approach (Bill Holland, Michael Cox, Frank Bryan, personal communication).

### 2.4.3 Boundary Conditions

The boundary conditions are another aspect of the model which are not tightly coupled to the fundamental numerical scheme, but which exert a strong influence on the overall quality of the simulation.

#### Surface

The surface boundary conditions in the model are applied stresses based on standard parameterizations. The finite-element scheme is expected to be more accurate than finite-difference schemes with respect to boundary conditions, because the derivative boundary condition enters the equations analytically, rather than by a finite-difference approximation. Therefore the effect of a particular stress should be much less dependent on the grid resolution near the surface.

#### Bottom

The bottom boundary layer is not expected to be resolved in most large-scale calculations. The model parameterizes the stress that the benthic viscous boundary layer applies on the interior flow by a simple scaling:

$$\frac{\partial u}{\partial z} = -c_D \hat{u}$$

where  $c_D$  is a drag coefficient and  $\hat{u}$  is the value of  $u$  in the interior near the boundary.

### Lateral Closed Boundaries

The debate about how to treat lateral boundaries properly in large-scale ocean models has been active for years, and shows no signs of slowing down. In the current model, both the free-slip and the no-slip boundary conditions are rejected as being unrealistic, being replaced by a parameterized boundary layer with a “partial-slip” boundary condition.

The usual model for lateral boundaries in an ocean model is an infinitely high, impermeable vertical wall. Given this assumption, the no-slip condition is the correct boundary condition for viscous flow — if the boundary layer is resolved. For the very small values of horizontal viscosity used in eddy-resolving models, this is probably not the case. There are several combinations of the frictional coefficients with the other parameters of the problem that lead to length scales associated with the viscous terms. The best known are the Stommel and Munk scales, associated with bottom and lateral friction respectively. These arise in simple linear vorticity models which do not necessarily include all of the important boundary layer dynamics. The Stommel scale is given by

$$L_S = \frac{r}{\beta}$$

where  $r$  is the inverse of the linear bottom-friction time scale, and  $\beta$  is the gradient of the Coriolis parameter. For decay time scales of  $O(100)$  days, this boundary layer is less than 6 km in width. The Munk layer scale is given by

$$L_M = \sqrt[3]{\frac{A_H}{\beta}}.$$



For eddy-resolving models, values of  $A_H$  are in the range of 100–500  $\text{m}^2\text{s}^{-1}$ , yielding a Munk layer scale of 17–30 km. While it might be said that this is “resolved”, since there is usually one grid point in the layer, it is not reasonable to expect the answers to be *quantitatively* correct, since finite difference schemes typically require several grid points per characteristic scale to get errors down below 10%.

It is crucial that the models incorporate the correct behavior in the boundary layer because the stress at the boundary is the relative vorticity of the fluid. In the case of mid-latitude boundary currents, for example, the instability of the separated boundary current can be expected to be quite strongly dependent on the vorticity of the fluid being advected off of the boundary and carried along with the free jet.

The alternative approach of using a free-slip condition does not allow viscous stresses to introduce any vorticity at the boundary. This is likely to produce boundary currents at least as inaccurate as those the no-slip case produces. It is also inconsistent with the non-negligible levels of viscosity still required in eddy-resolving models, since the free-slip condition arises from the inviscid equations.

Therefore, the most reasonable alternative is to allow the parameterization of the stress at the boundaries. Considerable work remains to decide on what this parameterization should be, but the model allows easy experimentation to determine the effects of various choices. Important open questions relate to the effects of more accurate schemes on the vorticity produced by the western boundary layer, and on the relative roles of side-wall and bottom friction in the continental shelf regions.

The implementation of a specified-stress boundary condition is straightfor-

ward along zonal and meridional boundaries, but is problematic along sloping boundaries. The usual strategy of applying “stair-step” boundary geometries allows the direct application of the kinematic (no normal flow) condition, but does not allow the direct application of the normal derivative of the tangential velocity to the finite-difference scheme. This is complicated by the fact that the tangential velocity is a linear combination of the  $u$  and  $v$  velocity fields, which are not defined on the same grid points.

### **Lateral Open Boundaries**

Open boundaries in ocean models are even more suspect than closed boundaries. It has been shown that it is not possible to produce a mathematically well-posed problem for the inviscid primitive equations at an open boundary (Olinger and Sundstrom, 1978) in terms of the spatial variables. These results suggest that it is possible to produce a well-posed open boundary condition in vertical-mode space, but the application of such an open boundary condition has not yet been published.

The usual implementation strategy for open boundaries is to over-specify Sommerfeld radiation conditions at the boundaries and then to smooth along the boundaries to remove the resulting short-scale noise from the solution. This has not been implemented in the model, though it should be straightforward. As with most of the model, the implementation of the boundary conditions is isolated to a single set of subroutines for simple modification.

#### 2.4.4 Equation of State

The equation of state is contained in a separate subroutine, and is easily replaceable. The basic model contains a simple bilinear relation, with constant coefficients for the temperature and salinity dependence. Since the density is calculated at all grid locations simultaneously, good performance will be achieved for any analytic formula. The usual polynomial approximations execute at full machine speed.

# Chapter 3

## Derivations and Differencing

### 3.1 Introduction

This chapter presents the details of the derivations of the equations of motion which result from the numerical decisions outlined in Chapter 1. This includes coordinate transformations, time differencing, and space differencing. This chapter is intended to be complete, rather than readable, and I have made an effort to describe the details of the effort to piece these techniques together. I have attempted to provide at least a brief explanation of each numerical technique, but there is not room here to provide substantial background material. The reader is referred to the references for further explanation.

### 3.2 Governing Equations

The governing equations are the Navier-Stokes equations in a rotating, Cartesian coordinate system, modified by the usual oceanic approximations: small aspect ratio, hydrostatic, Boussinesq, and no vertically-directed Coriolis force. In the usual notation, the basic equations are:

$$\frac{\partial u}{\partial t} + L(u) - fv = -\frac{1}{\rho_0} \frac{\partial p}{\partial x} + F_m(u) \quad (3.1)$$

$$\frac{\partial v}{\partial t} + L(v) + fu = -\frac{1}{\rho_0} \frac{\partial p}{\partial y} + F_m(v) \quad (3.2)$$

$$(3.3)$$

$$\frac{\partial p}{\partial z} = -\rho g \quad (3.4)$$

$$\nabla_3 \cdot \vec{V} = 0 \quad (3.5)$$

$$\frac{\partial T}{\partial t} + L(T) = F_T(T) \quad (3.6)$$

$$\frac{\partial S}{\partial t} + L(S) = F_S(S) \quad (3.7)$$

$$\rho = \rho(T, S, p). \quad (3.8)$$

In the above:  $L(\alpha)$  is the three-dimensional advection operator

$$L(\alpha) = \vec{V}_3 \cdot \nabla \alpha; \quad (3.9)$$

equation (3.8) is the equation of state, which may be modelled by a variety of polynomial approximations; and  $F_m, F_T, F_S$  represent the diffusion of momentum, temperature, and salinity, respectively. The symbols are defined in Table 3.1.

The numerical treatment of each of the terms in the above equations is discussed in the following sections. An effort has been made to separate the treatment of the terms to allow easy modification of the code.

$x, y, z$	Cartesian coordinates
$x, y, s$	transformed coordinates
$h$	metric term = $\frac{\partial z}{\partial s}$
$g$	gravitational acceleration
$f$	Coriolis parameter
$\beta$	$\frac{\partial f}{\partial y}$
$D$	depth of water (positive)
$D_0$	minimum depth (positive)
$K_m$	coefficient of vertical momentum diffusion
$K_T$	coefficient of vertical temperature diffusion
$K_S$	coefficient of vertical salinity diffusion
$A_m$	coefficient of horizontal momentum diffusion
$A_T$	coefficient of horizontal temperature diffusion
$A_S$	coefficient of horizontal salinity diffusion
$\theta$	selector for vertical diffusion scheme
$u, v, w$	Cartesian velocity components
$u, v, \dot{s}$	velocity in transformed coordinates
$U, V$	vertically averaged velocity components
$\rho_0$	mean density of water
$\rho'$	density anomaly
$p$	total pressure
$p'$	baroclinic pressure anomaly
$\eta$	free surface height anomaly
$T$	temperature
$S$	salinity
$\vec{V}_2$	horizontal velocity vector
$\vec{V}_3$	three-dimensional velocity

Table 3.1: List of Symbols

### 3.2.1 Boundary Conditions

This model formulation includes a free surface. Since the position of the free surface varies by no more than one meter or so due to geophysically relevant flows, some approximations are possible to simplify the boundary conditions. The wind and thermohaline forcing are applied at  $z = 0$ , by

$$\rho_0 K_m \frac{\partial}{\partial z}(u, v) = (\tau^x, \tau^y) \quad (3.10)$$

$$\rho_0 (K_T, K_S) \frac{\partial}{\partial z}(T, S) = (F^T, F^S), \quad (3.11)$$

where  $K_m$  is the coefficient of vertical momentum diffusion at the sea surface, and  $K_T$  and  $K_S$  are the coefficients of vertical temperature and salinity diffusion at the surface.

At the sea floor, the lower Ekman layer is parameterized by a simple drag coefficient model, and the fluxes of heat and salt are zero:

$$\rho_0 K_m \frac{\partial}{\partial z}(u, v) = c_D(u, v) \quad (3.12)$$

$$\frac{\partial}{\partial z}(T, S) = 0. \quad (3.13)$$

The momentum boundary condition can be viewed as a “partial-slip” condition. The no-slip condition produces excessive momentum loss if the boundary layer is unresolved, while the free-slip condition yields no momentum loss. This partial-slip can be tuned to produce an intermediate value of drag more closely approximating an actual Ekman layer (though the lateral Ekman transport does not exist in this simplification). The model formulation allows the drag coefficient to be a user-defined function of space and time. This can be used to include the changes in bottom drag caused by topographic roughness, for example.

The kinematic condition at the free surface ( $z = \eta(x, y, t)$ ) is

$$\frac{D\eta}{Dt} = w, \quad (3.14)$$

where

$$\frac{D}{Dt} \equiv \frac{\partial}{\partial t} + L_2(), \quad (3.15)$$

and  $L_2()$  is the two-dimensional advection operator. The boundary condition at the bottom ( $z = -D(x, y)$ ) is

$$w = -\vec{V}_2 \cdot \nabla D \quad (3.16)$$

for the case of a free-slip boundary, or (as a special case)

$$w = 0, \quad (3.17)$$

for a no-slip boundary.

### 3.3 Coordinate Transformations

The formula used in the current implementation is:

$$\frac{z}{D} = -(1-s) \left[ 1 - \left( 1 - \frac{D_0}{D} \right) s \right]. \quad (3.18)$$

The derivatives of the governing equations transform as (following (Cane, 1986)):

$$s = s(x, y, z), \quad z = z(x, y, s). \quad (3.19)$$

Define

$$h(x, y, s) \equiv \frac{\partial z}{\partial s} \quad (3.20)$$

so that

$$\frac{\partial}{\partial z} = \frac{\partial s}{\partial z} \frac{\partial}{\partial s} = \frac{1}{h} \frac{\partial}{\partial s}, \quad (3.21)$$



and, with  $\zeta = x$  or  $y$

$$\left(\frac{\partial}{\partial \zeta}\right)_z = \left(\frac{\partial}{\partial \zeta}\right)_s - \frac{\partial s}{\partial z} \left(\frac{\partial z}{\partial \zeta}\right)_s \frac{\partial}{\partial s}. \quad (3.22)$$

The pressure term is written as

$$p = p' + \rho_0 g z + \rho_0 g \eta, \quad (3.23)$$

where

$$\frac{\partial p'}{\partial z} \equiv -g\rho' \quad (3.24)$$

The middle pressure term has no dynamical significance, as it disappears from the horizontal gradient terms. Therefore, it is removed from the following calculations. Transforming into the new vertical coordinate converts the pressure gradient term to

$$\nabla_2 p|_z = \nabla_2 p'|_s - \frac{1}{h} \nabla z|_s \frac{\partial p'}{\partial s} + g \nabla \eta. \quad (3.25)$$

By use of the hydrostatic equation this may be rewritten as

$$\nabla p' + g\rho' \nabla z + g \nabla \eta, \quad (3.26)$$

Where the gradient operators are now implied to be two-dimensional and with respect to constant  $s$ . The new middle term is the topographic correction term, and is the cause of considerable trouble, as will be discussed later.

Applying these rules to the governing equations (and removing the mean density and associated pressure terms) results in:

$$\frac{\partial u}{\partial t} + L(u) - fv = -\frac{1}{\rho_0} \frac{\partial p'}{\partial x} - g \frac{\rho'}{\rho_0} \frac{\partial z}{\partial x} - g \frac{\partial \eta}{\partial x} + F_m(u) \quad (3.27)$$

$$\frac{\partial v}{\partial t} + L(v) + fv = -\frac{1}{\rho_0} \frac{\partial p'}{\partial y} - g \frac{\rho'}{\rho_0} \frac{\partial z}{\partial y} - g \frac{\partial \eta}{\partial y} + F_m(v) \quad (3.28)$$

$$\frac{\partial p'}{\partial s} = -g\rho' \frac{\partial z}{\partial s} \quad (3.29)$$

$$\nabla_2 \cdot (h\vec{V}) + \frac{\partial}{\partial s}(h\dot{s}) = 0 \quad (3.30)$$

$$\frac{\partial T}{\partial t} + L(T) = F_T(T) \quad (3.31)$$

$$\frac{\partial S}{\partial t} + L(S) = F_S(S) \quad (3.32)$$

$$\rho = \rho(T, S, z). \quad (3.33)$$

Now the three-dimensional velocity vector has components  $u, v, \dot{s}$ , where

$$\dot{s} \equiv \frac{1}{h} (w - \vec{V}_2 \cdot \nabla z). \quad (3.34)$$

Note that the hydrostatic equation has gained a metric term and that the continuity equation is now in flux form.

### 3.3.1 Viscous/Diffusive Terms

The second derivatives present in the viscous and diffusive terms cause the transformed versions to be rather complex. The constant-coefficient diffusion terms transform as

$$\frac{\partial^2 \alpha}{\partial z^2} \implies \frac{1}{h^2} \frac{\partial^2 \alpha}{\partial s^2} - \frac{1}{h^3} \frac{\partial h}{\partial s} \frac{\partial \alpha}{\partial s} \quad (3.35)$$

and

$$\left. \frac{\partial^2 \alpha}{\partial x^2} \right|_z \implies \frac{\partial^2 \alpha}{\partial x^2} - \frac{2}{h} \frac{\partial z}{\partial x} \frac{\partial^2 \alpha}{\partial x \partial s}$$

$$\begin{aligned}
& + \left( \frac{2}{h^2} \frac{\partial z}{\partial x} \frac{\partial h}{\partial x} - \frac{1}{h^3} \frac{\partial h}{\partial s} \left( \frac{\partial z}{\partial x} \right)^2 - \frac{1}{h} \frac{\partial^2 z}{\partial x^2} \right) \frac{\partial \alpha}{\partial s} \\
& + \frac{1}{h^2} \left( \frac{\partial z}{\partial x} \right)^2 \frac{\partial^2 \alpha}{\partial s^2}.
\end{aligned} \tag{3.36}$$

For the vertical terms, the nonconstant-coefficient version is

$$\frac{\partial}{\partial z} K \frac{\partial \alpha}{\partial z} \implies \frac{1}{h^2} \left( K \frac{\partial^2 \alpha}{\partial s^2} + \frac{\partial K}{\partial s} \frac{\partial \alpha}{\partial s} - \frac{K}{h} \frac{\partial h}{\partial s} \frac{\partial \alpha}{\partial s} \right). \tag{3.37}$$

The nonconstant-coefficient formulation of the lateral viscosity is extremely complex and is included here for reference only. It would be far too costly to actually calculate all of these terms — especially in a correct finite-element formulation.

The formula is

$$\begin{aligned}
\frac{\partial}{\partial x} A \frac{\partial \alpha}{\partial x} \Big|_z & \implies A \frac{\partial^2 \alpha}{\partial x^2} + \left( \frac{\partial A}{\partial x} - \frac{1}{h} \frac{\partial A}{\partial s} \frac{\partial z}{\partial x} \right) \frac{\partial \alpha}{\partial x} - \frac{2}{h} A \frac{\partial z}{\partial x} \frac{\partial^2 \alpha}{\partial x \partial s} \\
& + \left[ \left( \frac{1}{h^2} \frac{\partial A}{\partial s} \left( \frac{\partial z}{\partial x} \right)^2 \right) - \frac{1}{h} \frac{\partial A}{\partial x} \frac{\partial z}{\partial x} - \frac{1}{h^3} A \frac{\partial h}{\partial s} \frac{\partial h}{\partial s} \left( \frac{\partial z}{\partial x} \right)^2 \right. \\
& \quad \left. - \frac{1}{h} A \frac{\partial^2 z}{\partial x^2} + \frac{2}{h^2} A \frac{\partial z}{\partial x} \frac{\partial h}{\partial x} \right] \frac{\partial \alpha}{\partial s} \\
& + \frac{1}{h^2} A \left( \frac{\partial z}{\partial x} \right)^2 \frac{\partial^2 \alpha}{\partial s^2}.
\end{aligned} \tag{3.38}$$

As an alternative to this calculation, it is possible to interpolate the fields to be diffused onto level surfaces and to calculate the viscous terms at constant  $z$ . Since the functions are prescribed to be linear in  $s$ , this interpolation can be made exactly. The difficulty lies in the application of lateral boundary conditions in the interior produced by the presence of topography. This was a primary reason for switching to a boundary-fitted coordinate in the first place, but in this case, maintaining the boundary-fitted coordinate is clearly too expensive for non-constant-coefficient lateral diffusion terms.

The current implementation uses constant-coefficient vertical viscosity according to the formula above, and implements “lateral” viscosity along constant  $s$  surfaces. Obviously, the usefulness of this approximation will depend on how important diffusion is to the physics — the current implementation is only valid for nearly inviscid flow regimes.

### 3.4 Vertical Discretization Scheme

The vertical discretization of the transformed equations is by Galerkin finite elements. The nodes are taken to be uniformly spaced in  $s$ , and linear basis functions are used for  $u, v, T, S$ . Since the equation of state does not involve integration or differentiation in  $z$ , it follows that  $\rho'$  is also piecewise linear in  $s$ .

The diagnostic variables  $p'$  and  $s$  have a more complex vertical structure governed by the need for consistency with their defining equations. This will be discussed later.

In the Galerkin scheme, the residual of the discretized equations is forced to be orthogonal to each of the basis functions. Since this is a *finite*-element scheme, the basis functions are local – in this case, piecewise linear functions in  $s$ . For uniform grid spacing, calculating the inner product of the independent variable  $\alpha$  against the basis functions yields the tridiagonal matrix expression

$$\mathbf{M}\vec{\alpha} = \frac{\Delta s}{6} \begin{bmatrix} 2 & 1 & & & & \\ 1 & 4 & 1 & & & \\ & 1 & 4 & 1 & & \\ & & 1 & 4 & 1 & \\ & & & 1 & 4 & 1 \\ & & & & 1 & 2 \end{bmatrix} \begin{bmatrix} \alpha_1 \\ \alpha_2 \\ \alpha_3 \\ \alpha_4 \\ \alpha_5 \\ \alpha_6 \end{bmatrix}. \quad (3.39)$$

Nonlinear terms are, of course, more complicated and cannot be expressed by

matrix operations. Simple quadratic terms are written as

$$w = uv \implies$$

$$\mathbf{M}w = \frac{1}{12}(u_k + u_{k-1})(v_k + v_{k-1}) + \frac{1}{3}u_k v_k + \frac{1}{12}(u_k + u_{k+1})(v_k + v_{k+1}) \quad (3.40)$$

where  $u$  and  $v$  are piecewise linear functions,  $\mathbf{M}$  is the matrix equation from the previous paragraph, and  $w$  is the result, which is the contribution of this term to the equation for this node. Many simple examples are worked out in (Cullen, 1979).

The result of this procedure is a set of  $K$  equations (for a discretization with  $K$  nodes in the vertical) which express the orthogonality of the residual with respect to each of the  $K$  basis functions. Since the unknown variables are linear, the whole system reduces to a statement of the form

$$\mathbf{M}w = Q, \quad (3.41)$$

where  $w$  is a vector of any of the unknown prognostic variables, and  $Q$  is a very complicated expression resulting from integrating the right-hand-side of the equations against each of the basis functions. Note that  $\mathbf{M}$  is a matrix representing only the vertical structure of the solutions, so (3.41) consists of one independent tridiagonal system of equations for each point in  $x$  and  $y$ . These equations can be solved independently, either in parallel, or by vectorizing across the systems of equations. This latter approach is implemented in the present code.

It is important to note here that for consistency, this scheme must be applied uniformly to all the terms in the equations. The finite element scheme is not the same as simply treating the vertical derivative operators with a higher-order scheme. The benefit of applying the scheme is a guarantee of freedom from

aliasing, and conservation of quadratic invariants. Because of the metric terms, the momentum and mass are both quadratic invariants. The energy is a cubic, and is not guaranteed to be conserved, though it is conserved to fourth-order accuracy.

The diagnostic variables  $p'$  and  $\dot{s}$  have a more complex vertical structure. The perturbation pressure is the easier term,

$$p'(s) = -g \int_1^s \rho' h ds'. \quad (3.42)$$

Since  $\rho'$  and  $h$  are piecewise linear,  $p'$  is piecewise cubic in  $s$ . The finite element approximations to the pressure gradient terms must make use of the full cubic structure of  $p'$  to guarantee the conservation properties of the Galerkin scheme.

For maximum efficiency, the model integrates these terms using a 4-point Gauss-Lobatto integration scheme (Abramowitz and Stegun, 1972). This scheme is exact for polynomial functions up to fifth order, and so is exact for integrals of  $p'$  multiplied by basis functions and integrals of  $p'$  multiplied by the metric term  $h$ . This latter calculation is used in averaging operations for the calculation of the barotropic flow. The weights and nodes for 4-point Gauss-Lobatto integration are

$$\omega_i = \frac{\Delta s}{12} \{1, 5, 5, 1\} \quad (3.43)$$

$$x_i = \left\{ 0, \frac{1}{2} \left( 1 - \frac{1}{\sqrt{5}} \right), \frac{1}{2} \left( 1 + \frac{1}{\sqrt{5}} \right), 1 \right\}, \quad (3.44)$$

where the  $x_i$  are mapped into each interval  $[s_k, s_{k-1}]$ . The hydrostatic equation is integrated to evaluate  $p'$  on the finer grid of the Gauss-Lobatto points and integrals are evaluated as simple weighted sums of pressure terms multiplied by linearly interpolated basis functions or metric terms  $h$ .

The vertical velocity in the new coordinate system is more difficult to treat correctly. Integrating the continuity equation yields

$$\dot{s}(s) = -\frac{1}{h} \int_0^s \nabla \cdot (h\vec{V}_2) ds'. \quad (3.45)$$

Since  $h$  is a piecewise linear function,  $\dot{s}$  is a rational function composed of a cubic polynomial in  $s$  divided by a linear polynomial in  $s$ . No simple pointwise integration schemes are available for integrating this function, and the evaluation of the analytic integrals is quite expensive. In order to maintain reasonable efficiency, I have chosen to apply the same scheme to the vertical advection terms as is used for the pressure gradient terms. The vertical velocity is evaluated on the finer Gauss-Lobatto grid, and integrals of vertical advection terms are approximated by four-point Gauss-Lobatto integration. This has an error proportional to  $\Delta s^6$ , and is therefore fifth-order accurate. The vertical advection scheme with this discretization is not guaranteed to be conservative, but the high order of the scheme will force the errors to be small.

### 3.5 Horizontal Discretization Scheme

The basic horizontal discretization scheme is the Arakawa C-grid, shown in figure 3.1. The grid is ideal for integration of the gravity-wave part of the dynamics, since pressure gradient terms are easily calculated at the appropriate horizontal velocity points, and the divergence terms are easily calculated at the vertical velocity points. Other terms require spatial averaging to be available at the desired places, and there is some degree of flexibility in the calculation of those averages. In the present model,  $T, S, \rho, p'$ , and  $\dot{s}$  are all evaluated at the same points in the horizontal, while  $u$  and  $v$  occupy their usual C-grid positions. Thus the Coriolis

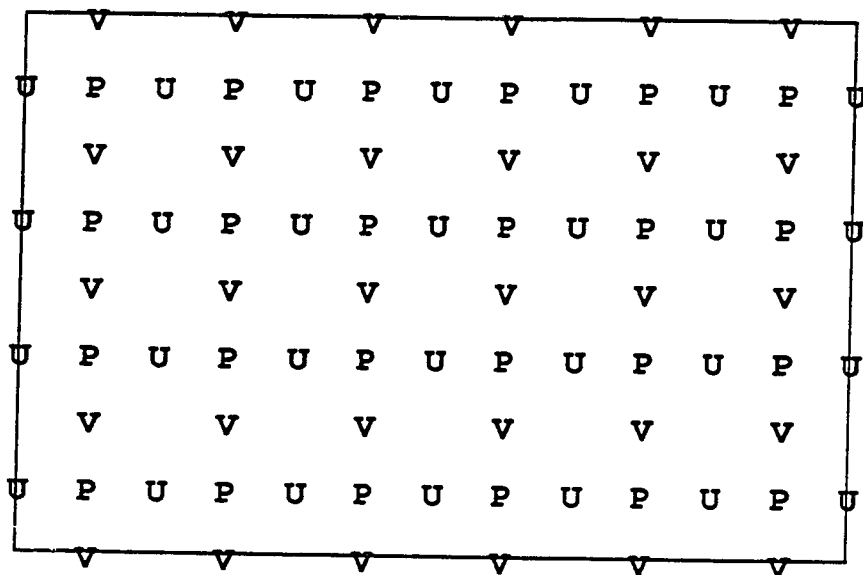


Figure 3.1: The Arakawa C-grid in a sample geometry

term must be based on a velocity interpolated in both the  $x$  and  $y$  directions in order to be available for each momentum equation.

### 3.5.1 Advection Terms

The most important interpolations required in the horizontal momentum equations are for the nonlinear advective terms. The naive approach of discretizing  $\vec{V} \cdot \nabla u$  directly as  $u \frac{\partial u}{\partial x} + v \frac{\partial u}{\partial y}$  has poor stability properties due to excessive aliasing. A simple modification which increases the stability of the scheme is the quadratic-averaging approach, which comes from the identity

$$\vec{V} \cdot \nabla \alpha = \nabla \cdot (\alpha \vec{V}) - \alpha \nabla \cdot \vec{V}. \quad (3.46)$$



In Cartesian coordinates in the three-dimensional case, the final correction term vanishes identically since the flow is non-divergent. This form is used in at least some versions of the GFDL model (Bryan, 1969). Due to the nonlinear vertical mapping and finite-element discretization of the present model, this approach is awkward, and is modified slightly to

$$\vec{V} \cdot \nabla \alpha = \nabla \cdot (\alpha \vec{V}_2) - \alpha \nabla \cdot \vec{V}_2 + s \frac{\partial \alpha}{\partial s}. \quad (3.47)$$

Here only the horizontal terms are in the quadratic averaged form. The form of the vertical advection term is unimportant, since it will be integrated analytically against the basis functions in a nearly conservative way, as discussed in the previous section. This representation of the nonlinear terms was studied by Grammelveldt (Grammelveldt, 1969) and shown to be more stable than the naive schemes, but less stable than the more sophisticated and expensive energy-conserving schemes.

On the finite-difference grid, the difference and averaging operators will be denoted by

$$\delta_x \alpha = \frac{1}{\Delta x} (\alpha_i - \alpha_{i-1}) \quad (3.48)$$

$$\delta_{2x} \alpha = \frac{1}{2\Delta x} (\alpha_{i+1} - \alpha_{i-1}) \quad (3.49)$$

$$\bar{\alpha}^x = \frac{1}{2} (\alpha_i + \alpha_{i-1}) \quad (3.50)$$

and

$$\bar{\alpha}^{xy} \equiv \overline{\bar{\alpha}^{xy}} \equiv \overline{\bar{\alpha}^{yx}}. \quad (3.51)$$

Note that the  $\delta_x$  and averaging operators are one-sided, to enable evaluation of values on the other node-types on the finite-difference grid. These are applied in either the positive or negative offset direction, depending on which variables are

being differentiated/interpolated to which grid. Since the grid is set up with  $p'_{i,j}$  to the east of  $u_{i,j}$  and to the north of  $v_{i,j}$ , the context determines the direction of the offsets. So now the finite-difference form of the horizontal part of the advection terms can be written as:

$$\vec{V} \cdot \nabla u = \delta_x \left( (\bar{u}^x)^2 \right) + \delta_y \left( \bar{u}^y \bar{v}^x \right) - u \left( \overline{(\delta_x u + \delta_y v)^x} \right), \quad (3.52)$$

with entirely analogous terms for the  $v$ -momentum equation. The formulation for the advection of temperature and salinity differs slightly from this due to the different grid locations of the variables. The scheme appropriate to those variables is

$$\vec{V} \cdot \nabla T = \delta_x \left( u \bar{T}^x \right) + \delta_y \left( v \bar{T}^y \right) - T \left( \overline{(\delta_x u + \delta_y v)^{xy}} \right), \quad (3.53)$$

with an identical equation for salinity.

### 3.5.2 Diffusion Terms

The lateral diffusion terms for the barotropic mode are currently treated explicitly with the simple finite-difference operator

$$\nabla^2 q \approx \frac{1}{\Delta x^2} (q_{i+1,j} - 2q_{i,j} + q_{i-1,j}) + \frac{1}{\Delta y^2} (q_{i,j+1} - 2q_{i,j} + q_{i,j-1}). \quad (3.54)$$

The Dufort-Frankel scheme for the lateral viscosity of the baroclinic modes is obtained by time-averaging the center term in the stencil,

$$\nabla^2 q \approx \frac{1}{\Delta x^2} (q_{i+1,j} - 2\bar{q}_{i,j}^t + q_{i-1,j}) + \frac{1}{\Delta y^2} (q_{i,j+1} - 2\bar{q}_{i,j}^t + q_{i,j-1}). \quad (3.55)$$

This can then be simplified to

$$\frac{1}{\Delta x^2} q_{i,j}^{n+1} = \frac{1}{\Delta x^2} \left( (\bar{q}^x)^n - q_{i,j}^{n-1} \right) + \frac{1}{\Delta y^2} \left( (\bar{q}^y)^n - q_{i,j}^{n-1} \right), \quad (3.56)$$

where the term at the new time level  $n + 1$  has been moved to the left side of the equation.

For later use, define

$$\alpha \equiv A_h 2\Delta t \left( \frac{1}{\Delta x^2} + \frac{1}{\Delta y^2} \right), \quad (3.57)$$

and

$$\hat{F}_h(q) \equiv 2A_h \left( \frac{\bar{q}^x}{\Delta x^2} + \frac{\bar{q}^y}{\Delta y^2} \right). \quad (3.58)$$

Then the Dufort-Frankel scheme can be written

$$(1 + \alpha)q^{n+1} = (1 - \alpha)q^{n-1} + \hat{F}_h(q^n). \quad (3.59)$$

### 3.6 Time Discretization/Integration Scheme

The model allows the treatment of the the barotropic mode in several ways. The simplest is to simply retain the barotropic component of the explicit equations and use a very short time step. This approach will be discussed in the section on the internal modes. A more generally useful technique is to treat the barotropic mode implicitly, which will be discussed here.

In order to bypass the very stringent time step limitation associated with the barotropic gravity waves, the free-surface anomaly,  $\eta$ , is integrated using the semi-implicit scheme (Kwizak and Robert, 1971). Unlike the rigid-lid scheme, this technique retains the barotropic gravity modes, but slows them down enough to be stable. More importantly, the free surface condition retains the vortex stretching term in the barotropic vorticity equation. This term is usually negligible, but can be of importance for long barotropic Rossby waves in shallow water or in high latitude regions (particularly the Southern Ocean).

In the semi-implicit scheme, the terms responsible for barotropic gravity waves are treated implicitly by averaging in time. These terms are: the pressure gradient due to the sea-surface height anomaly in the momentum equations, and the vertically integrated divergence terms in the continuity equation.

Leapfrog time differencing is used on the acceleration terms. All the remaining terms are calculated at the center time level, except for the diffusion terms, which are treated separately. For the baroclinic modes, the horizontal diffusion terms are calculated by the Dufort-Frankel scheme, while the vertical diffusion terms are treated by a general implicit scheme, discussed in the previous chapter. For the (implicit) barotropic mode, the vertical diffusion is integrated out analytically, and becomes a boundary-forcing term, while the horizontal diffusion is calculated from the old time level velocities. While this is only first-order accurate in time, it is not deemed to be a problem, since the high-frequency gravity waves are already severely distorted by the semi-implicit scheme, and since the dynamically important Rossby waves are of low frequency, and are thus well-resolved in time.

### 3.6.1 Solution of Vertically Integrated Flow

The semi-implicit scheme is applied here to the vertically averaged velocities and the sea-surface height anomaly. First, the equations for the vertically integrated flow must be derived and treated separately. The scheme is very similar to that outlined in Appendix C, so I will not review it again here. I define  $U$ , and  $V$  to be the vertically averaged  $u$  and  $v$  fields. Then applying the semi-implicit scheme to the vertically integrated momentum equations yields:

$$U^{n+1} + g\Delta t \frac{\partial \eta^{n+1}}{\partial x} = U^{n-1} - g\Delta t \frac{\partial \eta^{n-1}}{\partial x}$$

$$\begin{aligned}
& -2\Delta t \frac{1}{D} \int_0^1 L(u^n) \partial s' \\
& + 2\Delta t \left[ +fV^n + F_v(U^{n-1}) + F_h(U^{n-1}) \right] \\
& - 2\Delta t \frac{1}{D\rho_0} \int_0^1 \left( \frac{\partial p'}{\partial x} + g\rho' \frac{\partial z}{\partial x} \right) \partial s' \quad (3.60)
\end{aligned}$$

$$\begin{aligned}
V^{n+1} + g\Delta t \frac{\partial \eta^{n+1}}{\partial y} &= V^{n-1} - g\Delta t \frac{\partial \eta^{n-1}}{\partial y} \\
& - 2\Delta t \frac{1}{D} \int_0^1 L(v^n) \partial s' \\
& + 2\Delta t \left[ -fU^n + F_v(V^{n-1}) + F_h(V^{n-1}) \right] \\
& - 2\Delta t \frac{1}{D\rho_0} \int_0^1 \left( \frac{\partial p'}{\partial y} + g\rho' \frac{\partial z}{\partial y} \right) \partial s'. \quad (3.61)
\end{aligned}$$

The third equation for the semi-implicit calculation of the barotropic flow comes from the vertically integrated continuity equation. In order to make the resulting equations have constant coefficients, the depth is divided into a mean,  $\bar{D}$ , and a perturbation,  $D'$ . The part of the divergence associated with the mean depth is treated implicitly, and the remainder is treated explicitly to get

$$\bar{D} (\nabla \cdot \vec{V})^{n+1} + h\dot{s}^{n+1} = D_f, \quad (3.62)$$

where

$$D_f \equiv -\bar{D} (\nabla \cdot \vec{V})^{n-1} - h\dot{s}^{n-1} - 2D' (\nabla \cdot \vec{V})^n - 2\vec{V}^n \cdot \nabla D. \quad (3.63)$$

Next, I take the divergence of the vertically integrated horizontal momentum equations in order to substitute for the divergence terms in the vertically integrated continuity equation. If I now define the right-hand-sides of the vertically integrated horizontal momentum equations as  $U_f$  and  $V_f$ , I can write

$$\nabla \cdot \vec{V}^{n+1} = \nabla \cdot \vec{V}_f - g\Delta t \nabla^2 \eta^{n+1}. \quad (3.64)$$

Substituting this into the vertically integrated continuity equation (3.62) yields

$$-g\bar{D}\Delta t\nabla^2\eta^{n+1} + h\dot{s}^{n+1} = D_f - \nabla \cdot \vec{V}_f. \quad (3.65)$$

Finally,  $\eta^{n+1}$  and  $\dot{s}^{n+1}$  must be related in order to turn this into an elliptic equation for  $\eta^{n+1}$ . The desired relationship comes from the implicit version of the surface kinematic boundary condition

$$\frac{D\eta}{Dt} = \bar{w}^t = h\bar{s}^t. \quad (3.66)$$

Notice that here the other terms in the definition of  $\dot{s}$  (3.34) drop out since  $z$  and  $s$  are co-planar at the sea surface, and notice that the metric term is just a constant scale factor at the sea surface.

Expanding the implicit surface kinematic boundary condition gives

$$\eta^{n+1} - \Delta t h\dot{s}^{n+1} = \eta_f \quad \text{at } s = 1, \quad (3.67)$$

where

$$\eta_f \equiv \eta^{n-1} + \Delta t h\dot{s}^{n-1} - 2\Delta t (\vec{V} \cdot \nabla \eta^n). \quad (3.68)$$

Now the elliptic equation for  $\eta$  can be constructed

$$\nabla^2\eta^{n+1} - \frac{1}{g\bar{D}\Delta t^2}\eta^{n+1} = -\frac{1}{g\bar{D}}\Delta t \left[ D_f - \bar{D}\nabla \cdot \vec{V}_f + \frac{1}{\Delta t}\eta_f \right]. \quad (3.69)$$

This equation is solved for  $\eta^{n+1}$ , and then the barotropic velocities are obtained by back-substitution into the momentum equations (3.60) and (3.61). The implicit surface boundary condition (3.67) can then be used to obtain the vertical velocity at the surface if desired. This is the preferred technique for obtaining the vertical velocity at the sea surface, as it is much less prone to noise than the vertical integral of the two-dimensional divergence.

The boundary conditions for the elliptic equation are derived from the horizontal momentum equations. At a closed boundary, the normal flow is zero, and the normal momentum equation reduces to

$$g\Delta t \frac{\partial \eta^{n+1}}{\partial x} = -g\Delta t \frac{\partial \eta^{n-1}}{\partial x} + 2\Delta t \left[ +fV^n + 2\Delta t A_m \frac{\partial^2 U^{n-1}}{\partial x^2} \right] - 2\Delta t \frac{1}{D\rho_0} \int_0^1 \left( \frac{\partial p'}{\partial x} + g\rho' \frac{\partial z}{\partial x} \right)^n \partial s', \quad (3.70)$$

where I have chosen a meridional boundary for illustration. This equation is an explicit expression for the normal gradient of  $\eta^{n+1}$ , so it is a consistent boundary condition for the Helmholtz equation. The terms involving  $\eta$ , and  $V$  are straightforward, but the second derivative of the normal velocity and the integral of the normal gradient of the perturbation pressure pose additional problems. The viscous term is neglected based on a scaling argument, though this is not rigorously justifiable. The pressure gradient term is assumed to vanish in viscous simulations since the normal gradient of perturbation density is assumed to vanish in the absence of density fluxes across the boundary. This argument fails in the absence of dissipation, and a linear extrapolation of the normal pressure gradient from the interior values is used in those cases.

The efficient solution of the elliptic equation for the sea-surface height anomaly is the subject of an entire literature in itself. In this model, I have chosen to formulate the equation as a constant-coefficient Helmholtz equation, so that Fast Fourier Transform (FFT) techniques can be used for the solution. In the case of irregular geometry, the capacitance matrix method can be used to solve the problem with about 2–3 times the work required for the regular geometry case. On vector computers, the FFT's are calculated "sideways", by setting up the calculation for all the rows simultaneously and then vectorizing across the systems

of equations. After the FFT's, the equations are decoupled in the other coordinate direction. The resulting independent tridiagonal systems are also solved "sideways" by vectorizing the simple Gaussian elimination algorithm across the systems of equations, just as is done for the tridiagonal systems that result from the vertical finite element discretization.

More recently, an iterative method has been developed which extends the usefulness of the capacitance matrix method to non-constant-coefficient problems (Pares-Sierra and Vallis, 1989). This method has not been applied here, though it would not be prohibitively difficult to modify the barotropic code to treat the whole divergence implicitly, rather than just the part associated with the reference depth. This would produce a non-constant coefficient elliptic equation of the form

$$[\nabla \cdot D\nabla\eta]^{n+1} - \frac{1}{g\Delta t^2}\eta^{n+1} = -\frac{1}{g\Delta t^2}\eta_f - \frac{1}{g\Delta t}\nabla \cdot (D\nabla\vec{V}_f), \quad (3.71)$$

which can be solved with the method referenced above. This technique has the advantage of not requiring any time-averaging of the continuity equation. Since it uses the continuity equation with every term remaining in flux form, such a scheme might have better conservation and stability properties.

### 3.6.2 Solution of the Internal Modes

The calculation of the baroclinic modes is independent of the barotropic calculations just described. The leapfrog scheme is modified by the implicit treatment of both the vertical and horizontal momentum diffusion terms as discussed below. The basic discretization is

$$u^{n+1} = u^{n-1}$$



$$\begin{aligned}
& +2\Delta t \left[ -\frac{1}{\rho_0} \frac{\partial p'^n}{\partial x} - g \frac{\rho'}{\rho_0} \frac{\partial z}{\partial x} - L'(u^n) + f v^n \right] \\
& +2\Delta t \left[ F_v(u^{n+1}, u^{n-1}) + F_h(u^{n+1}, u^n, u^{n-1}) \right] \quad (3.72)
\end{aligned}$$

$$\begin{aligned}
v^{n+1} & = v^{n-1} \\
& +2\Delta t \left[ -\frac{1}{\rho_0} \frac{\partial p'^n}{\partial y} - g \frac{\rho'}{\rho_0} \frac{\partial z}{\partial y} - L'(v^n) - f u^n \right] \\
& +2\Delta t \left[ F_v(v^{n+1}, v^{n-1}) + F_h(v^{n+1}, v^n, v^{n-1}) \right] \quad (3.73)
\end{aligned}$$

$$s^{n+1} = -\frac{1}{h} \int_0^s \nabla \cdot h \vec{V} \partial s' \quad (3.74)$$

$$T^{n+1} = T^{n-1} + 2\Delta t [-L'(T) + F_v(T) + F_h(T)]^n \quad (3.75)$$

$$S^{n+1} = S^{n-1} + 2\Delta t [-L'(S) + F_v(S') + F_h(S')]^n \quad (3.76)$$

The hydrostatic equation is integrated exactly as discussed in the section on vertical discretization, and it is assumed here that the pressure is known at all  $p$  points when needed. Similarly, the equation of state is evaluated at the density points when it is needed.

Next let  $\mathbf{K}$  be the matrix resulting from the finite-element integration of the constant-coefficient vertical diffusion formula (3.35), let  $\mathbf{M}$  be the matrix for linear finite-element terms (3.39), and let  $\mathbf{FE}$  indicate the finite-element integrations that have been discussed in previous sections and which are not displayed in detail here. Then the  $u$ -momentum equation can be written

$$(\mathbf{M}(1 + \alpha) - \theta \Delta t \mathbf{K}) u^{n+1} = (\mathbf{M}(1 - \alpha) + (1 - \theta) \Delta t \mathbf{K}) u^{n-1}$$

$$\begin{aligned}
& +2\Delta t \mathbf{M} (fv^n + \hat{F}_h(u^n)) \\
& -2\Delta t \mathbf{FE}(L_2(u^n)) - 2\Delta t \mathbf{FE}(s \frac{\partial u}{\partial s}) \\
& - \frac{2\Delta t}{\rho_0} \mathbf{FE}(\frac{\partial p'^n}{\partial x} + g(\rho')^n \frac{\partial z}{\partial x}) \\
& +2\Delta t (F_{top} + F_{bottom}). \tag{3.77}
\end{aligned}$$

The right-hand-side is evaluated and then the tridiagonal system of equations implied by the left-hand-side is solved at each horizontal grid point. The equation for  $v$  is completely analogous, and the equations for  $T$  and  $S$  are similar, but less complex. The combination of the tridiagonal systems for the vertical structure and the vertical diffusion eliminates the need for a second tridiagonal solver and, in effect, makes the implicit treatment of the vertical diffusion free.

Once the momentum equations are solved for the new velocities, the vertical means are removed and replaced with the barotropic velocities which were calculated separately, then the vertical velocities are calculated on the fine vertical grid at the new time level. After the temperature and salinity have been updated, a new perturbation density field is calculated, and the perturbation pressure is calculated on the fine vertical grid in preparation for the next time step.

### 3.7 Implementation

As in any research project, the current implementation of the code is continuously evolving. Some of the design goals have not yet been met, but care has been taken to ensure that the implementation of these extra features will not prove inconsistent with the fundamental structure of the code.

The entire code is written in a language called 'PREP', written by Roger Ove. PREP is a variant of FORTRAN-77 and is implemented by a preprocessor

(written in C) which accepts PREP input and produces FORTRAN output. The package is publicly available in the USENET source archives. PREP has several advantages over FORTRAN as an implementation language for finite-difference codes. It provides an array notation which removes the need for most DO loops, and it provides macro expansion, conditional compilation, and enhanced flow control constructs. The resulting code is significantly more compact than FORTRAN, and hopefully more readable.

# Chapter 4

## Barotropic Model Tests

In order to debug the model, a variety of tests runs were performed. The test cases discussed here include both linear and nonlinear experiments chosen to isolate each piece of the equations for comparison against either known analytic solutions or well-known nonlinear model results.

The four basic tests are:

- Stommel and Munk single-gyre solutions.
- Isolated vortex drift and decay.
- Flow over an isolated seamount.
- Flow over multiple seamounts.

### 4.1 Stommel and Munk Single-Gyre Tests

The idealized solutions of Stommel (Stommel, 1948) and Munk (Munk, 1950), provide important tests of the Rossby wave dynamics and of the bottom and lateral viscosity of the model. The linear cases are very helpful, since analytic solutions exist, and the nonlinear versions are among the best-studied in the literature.

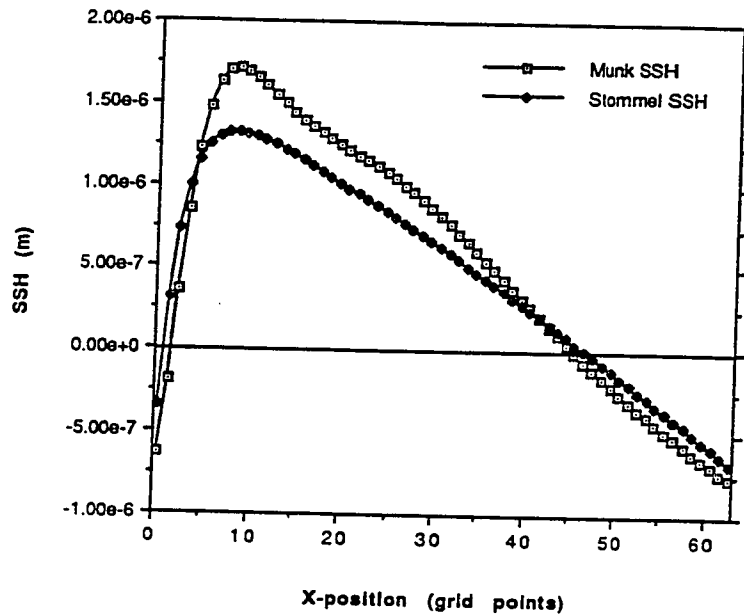


Figure 4.1: SSH anomaly for Barotropic Stommel/Munk tests

The numerical model in this case is constrained to be barotropic, and spun up from rest. The model is integrated until a steady state is achieved. Cross-sections of sea-surface height anomaly across the middle of the gyre are presented in Fig. 4.1. The corresponding meridional velocity fields along the same cross-section are presented in Fig. 4.2.

The sea-surface height anomalies for the two cases show the expected features. The Stommel case shows a smooth curve with a peak in the western basin, while the Munk case shows the characteristic dip just east of the maximum which corresponds to the recirculation region.

The meridional velocity field in the Stommel model shows a clear maximum at the boundary, with an exponential decay toward the interior. The observed scale of the exponential curve is about 2.5 grid points, while the analytical scale

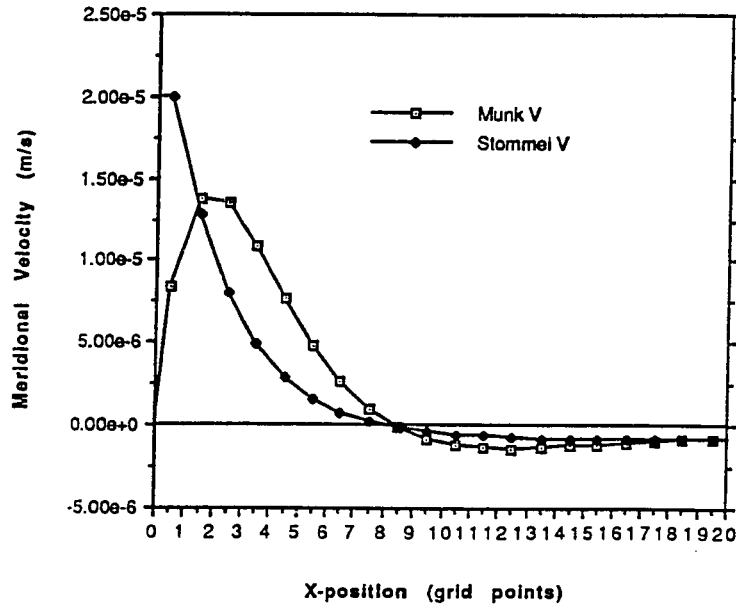


Figure 4.2: Meridional velocity in Western boundary current for Barotropic Stommel/Munk tests

is

$$\frac{r}{\beta} = \frac{50 \text{ days}^{-1}}{2 \times 10^{-11} \text{ m}^{-1} \text{ s}^{-1}} = 11.7 \text{ km} = 2.34 \Delta x,$$

which is an excellent agreement.

For the Munk model, the analytical scale is

$$\sqrt[3]{\frac{A_h}{\beta}} = \sqrt[3]{\frac{10 \text{ m}^2 \text{ s}^{-1}}{2 \times 10^{-11} \text{ m}^{-1} \text{ s}^{-1}}} = 8.0 \text{ km} = 1.60 \Delta x.$$

This agrees well with the observed location of the current maximum at about 1.5 grid intervals from the wall. Another experiment run with a larger grid spacing (and a predicted boundary layer width of  $0.8 \Delta x$ ) had no grid points in the boundary layer, and hence showed no evidence that the maximum in the velocity is separated from the wall.

The nonlinear versions of these cases showed the classical behavior as discussed in (Bryan, 1963; Veronis, 1966; Pedlosky, 1979). The nonlinear Stommel

model tends toward the Fofonoff free mode, while the nonlinear Munk model shows the expected standing Rossby waves in the outflow region. An example of the nonlinear response of a model with both lateral and bottom friction is presented in Fig. 4.3.

## 4.2 Isolated Vortex Tests

The behavior of an isolated vortex on a  $\beta$ -plane has been studied extensively both analytically (Flierl, 1977; Smith and Reid, 1982), and numerically (McWilliams and Flierl, 1979; Mied and Lindemann, 1979; Smith and Reid, 1982). Analytical results for the linear case include not only the solution (Flierl, 1977), but also closed-form expressions for many integral measures of the solution, such as the center of mass (Smith and Reid, 1982).

An isolated vortex was placed in a  $\beta$ -plane channel and allowed to evolve freely. When sufficient resolution was provided relative to the radius of deformation (in this case, the resolution was 5.5 grid points per radius of deformation), the observed westward drift of the center of mass was within 2% of the analytic solution. The observed westward drift of the pressure maximum was about 5% higher than the analytic solution, but I estimate at least a 3% uncertainty in reading the solution from the figure of (Smith and Reid, 1982). In addition, the position of the pressure maximum is determined by a bi-quadratic interpolation, which adds another uncertainty to the result. I conclude that the results agree to within measurement error.

The nonlinear test cases are more difficult to analyze. The most unambiguous result is that the southward drift of the pressure maximum was bounded above by  $1/4$  of the maximum Rossby phase speed (to within measurement error) in

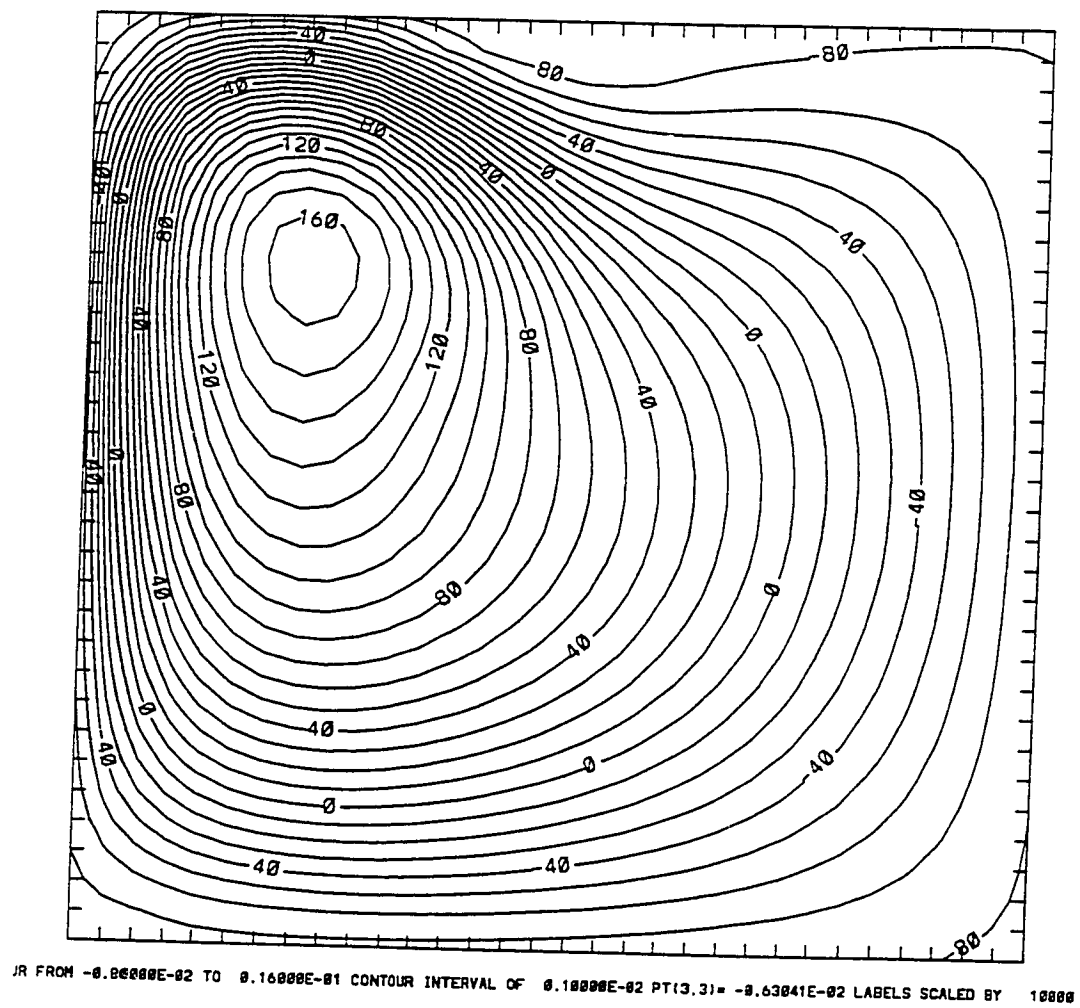


Figure 4.3: Sample SSH field for a nonlinear barotropic Stommel/Munk test



all cases. This result is common to all of the numerical papers except (Mied and Lindemann, 1979).

The other results from the nonlinear cases are very difficult to compare to (Smith and Reid, 1982) because of several errors in that paper, and because the authors of that paper did not realize that the nonlinear response of cyclonic and anticyclonic vortices is different. For example, the paper shows that nonlinearity decreases the rate of westward propagation of the center of mass, while the current model shows it to increase slightly. Their results are correct for cyclones, while the current result is correct for the anticyclones that were tested here (Nof, 1983).

### **4.3 Flow over an isolated Seamount**

In order to test the topographic terms in the barotropic mode, flow over an isolated, idealized seamount was chosen. The parameter space amenable to quasi-geostrophic modelling has been documented in (Verron and Provost, 1985).

Two parameter regimes are of interest: strong topography, and strong nonlinearity. The case of strong topography is represented in Fig. 4.4. In this case, the seamount extends through one half of the water column. The resulting streamlines are identical to the strong topography case in (Verron and Provost, 1985), their Fig. 3.

### **4.4 Flow Over Fieberling Guyot**

The first application of the new model to a test case for which the answers are not well known is the simulation of flow over multiple steep seamounts. In this case, the topography is an idealized representation of the Fieberling Guyot, located at approximately  $128^{\circ}$  W,  $32^{\circ}$  N, in the California Current system. The seamount

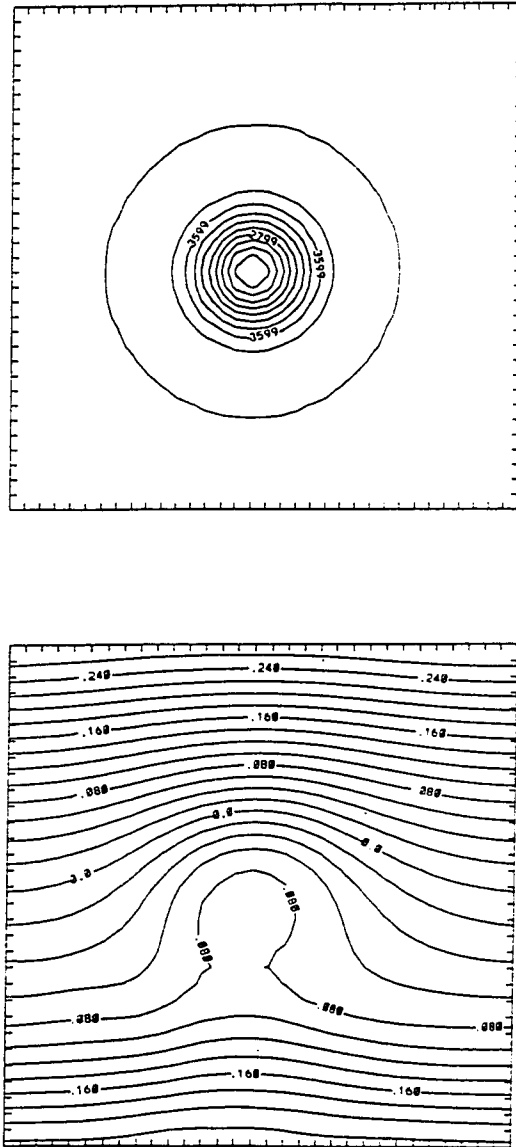


Figure 4.4: (a) Topography of isolated seamount. (b) Sea-surface height anomaly approximating the streamfunction.

extends from the sea floor at 4500 m depth to a peak at just 438 m depth. The guyot is nearly circular, and is well-represented by a Gaussian structure with an e-folding scale of 12 km. The very steep slopes of the seamount (exceeding  $30^\circ$  in some locations) pose significant difficulties for many numerical schemes.

The geometry for the initial numerical experiments contains one seamount and is shown in Fig. 4.5. The north and south boundaries are closed, with no applied stresses. The east and west boundaries are periodic. The domain is 256 km by 256 km.

Some further experiments are performed with two additional seamounts included to the east of Fieberling. Fieberling II is 55 km distant at an angle of  $20^\circ$  south of east, and extends up to a depth of 1050 m. The third seamount in the chain is another 30 km east-southeast along the same line, and extends up to a depth of about 1100 m. Both of the minor seamounts have e-folding radial scales of 6 km. This geometry is presented in Fig 4.6.

The flow is spun up from rest by a uniform zonal wind stress of  $1 \text{ dyne/cm}^2$ . The bottom drag coefficient was fixed at 50 days so that the solution would equilibrate in a reasonable amount of time. Most of the calculations were performed with an extremely small explicit lateral viscosity of  $10 \text{ m}^2\text{s}^{-1}$ .

Because of the expense of calculations with the full three-dimensional model, most of the experiments regarding convergence and sensitivity were performed with just the barotropic component of the code.

The goal of the barotropic tests was to determine the resolution required to adequately resolve the flow's interaction with the topography and to determine the sensitivity of the flow to changes in the horizontal viscosity coefficient.

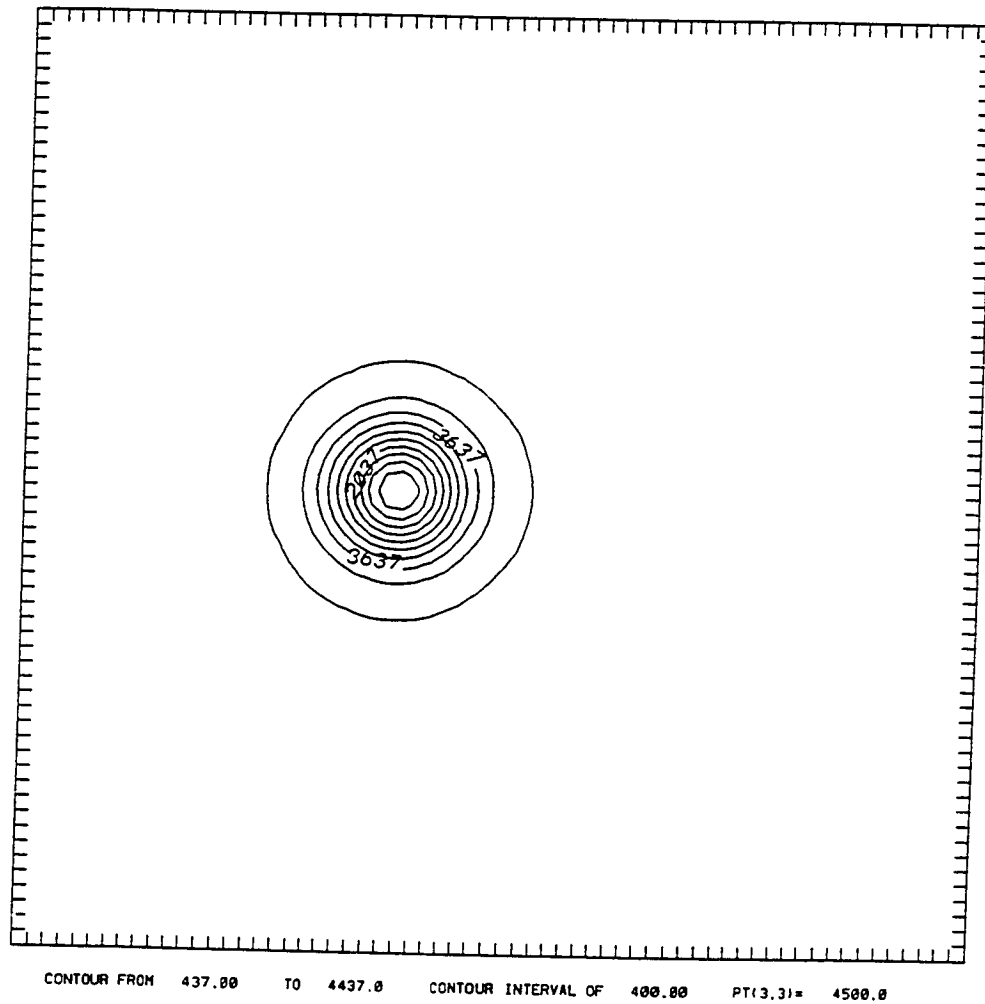


Figure 4.5: Contours of depth for the idealized Fieberling Guyot test cases. The far-field depth is 4500 m, and the minimum depth is 438 m. The lateral scale of the seamount is 12 km, and the box is 256 km by 256 km.



#### 4.4.1 Single Seamount Tests

The approach of the model to steady-state is shown in Fig 4.7. The maximum velocity in the domain increases steadily to about  $15 \text{ cm s}^{-1}$  in the first 200 days, while the total energy increases to about  $10^{15} \text{ J}$  in that period.

The barotropic response of the ocean to strong topography is best understood by examining the conservation of potential vorticity. In this case, the variations in  $f/h$  are so strong that bulk of the fluid above the seamount cannot acquire enough relative vorticity to move off of the seamount into deeper water. This trapped fluid constitutes the well-known Taylor column. As will be seen below, a small amount of water does leak off the SE corner of the seamount.

Experiments were run with 4 km and 2 km grid spacing to determine resolution required to converge to the continuous solution. The sea-surface-height (SSH) anomaly for both calculations are shown in Fig 4.8 for day 100 of the simulation. Only very minor deviations are apparent, particularly just upstream of the seamount, and on the SW corner.

More detailed comparisons are presented in Fig 4.9 and Fig 4.10. The anomaly of SSH due to the seamount is calculated by removing a mean slope from the SSH signal. The main SSH anomaly pattern is the maximum on the north side of the seamount. This does not change much in structure between days 100 and 150, but does increase slightly in amplitude. The difference field was produced by averaging the 2 km solution in  $x$  and  $y$  to evaluate at the same physical locations as the SSH points in the 4 km case. At day 100, there are coherent differences of up to 2 mm in amplitude. This corresponds to a phase error in the initial pinching off of a “bulge” from the SE corner of the seamount, as shown in Fig 4.9d. By day 150, that phase error has disappeared, and there are no coherent regions of

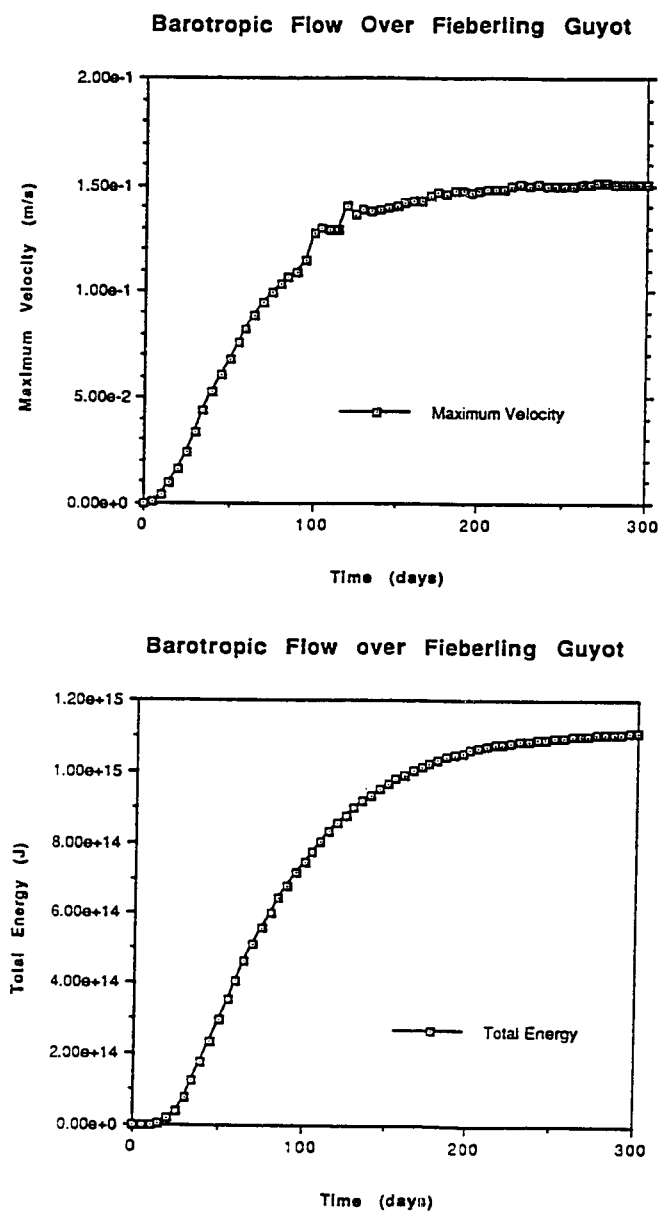


Figure 4.7: Spinup characteristics of the barotropic flow over Fieberling Guyot. (a) Peak velocity as a function of time. (b) Total energy as a function of time.





difference between the two solutions with amplitudes larger than 1 mm.

#### 4.4.2 Three Seamount Tests

The geometry of the seamount chain containing the Fieberling Guyot is approximated by the three seamounts of Fig 4.6. The spinup of these experiments is quite similar to the previous single-seamount cases, but requires slightly longer to equilibrate. The sea-surface-height anomaly at day 300 is shown in Fig 4.11. The important difference to note is the plateau in SSH over the two downstream seamounts. The flow around the upstream seamount is nearly identical to the single-seamount experiments. The SSH anomaly due to the topography is shown in Fig 4.12, and is very similar to the anomaly shown in Fig 4.10 for the earlier test.

More details are shown in Fig 4.13, which isolates the important contour levels at day 300. The field shows clear evidence of three Taylor columns, with stagnation points at the southwest corner of Fieberling I, due west of Fieberling II, and slightly south of west of Fieberling III. There is a uniform flow due southward in the gap between Fieberling I and II, and essentially no flow between Fieberling II and III. The flow which was diverted northward around the upstream seamount bifurcates at the stagnation point on the west flank of Fieberling II, and about half travels southward through the gap, while the other half rides the north side of Fieberling II and III until it can return south along the east side of Fieberling III.

#### 4.4.3 Convergence Tests

The model geometry with three seamounts was used in a series of tests designed to explore the convergence rate of the numerical model calculations. The model

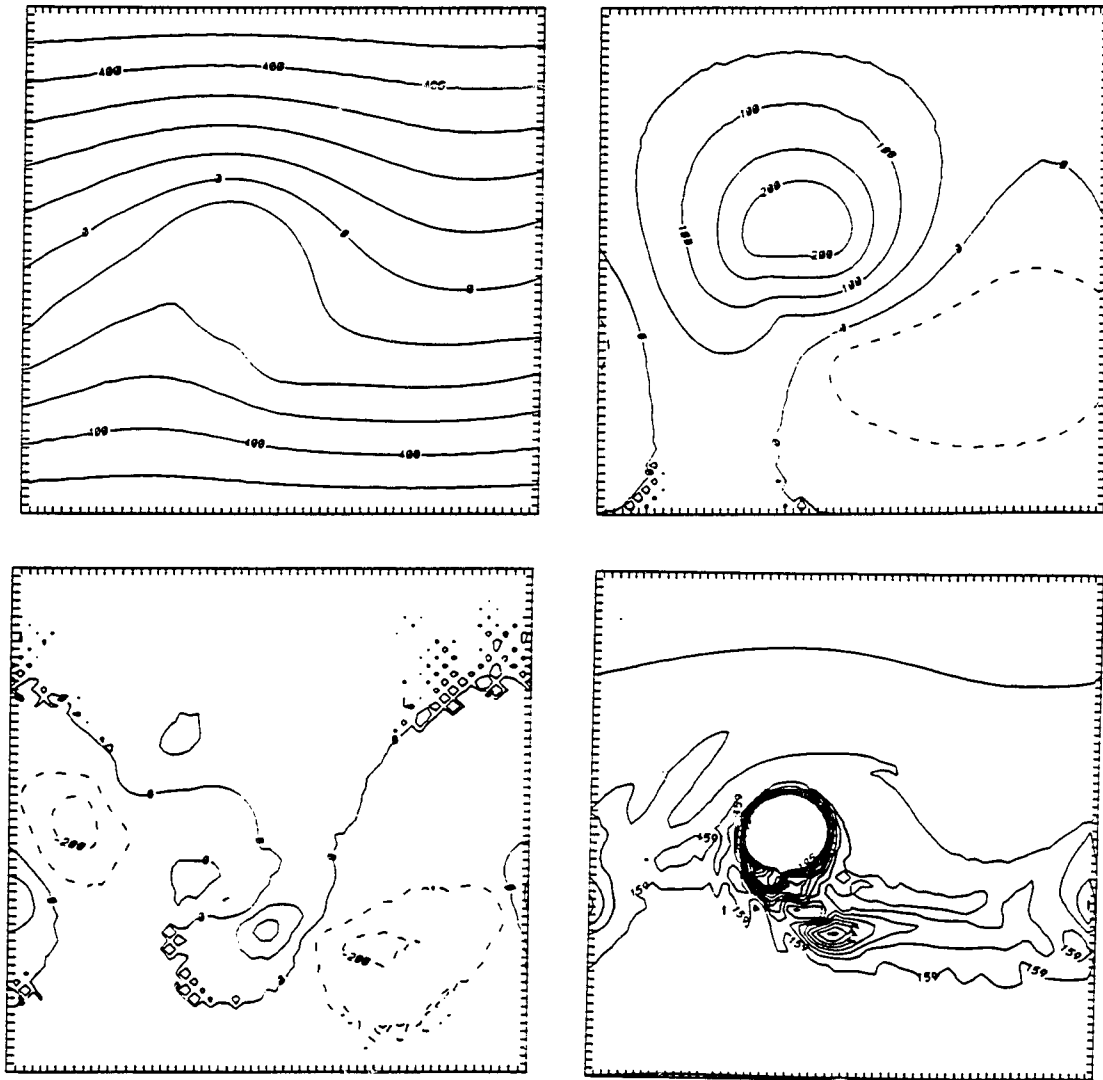


Figure 4.9: Barotropic response of the Fieberling Guyot at day 100 of the simulation. (a) Sea-surface height. Range is  $\pm 6$  cm. (b) Sea-surface-height anomaly due to seamount. Range is  $\pm 2$  cm. (c) Difference between 2 km and 4 km resolution experiments. Range is  $\pm 2$  mm. (d) Potential vorticity field, showing the pinch-off of a bulge on the SE corner of the seamount.

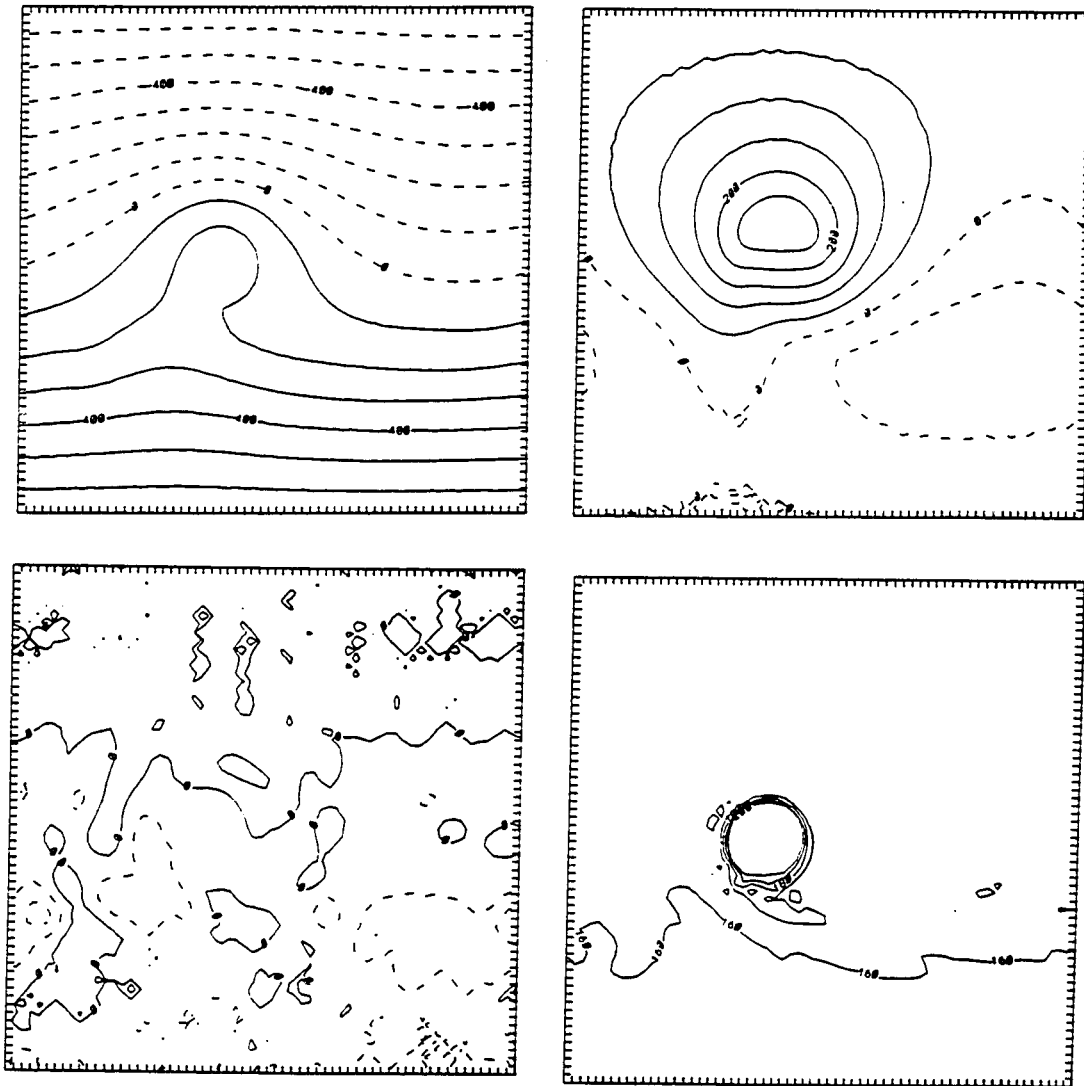
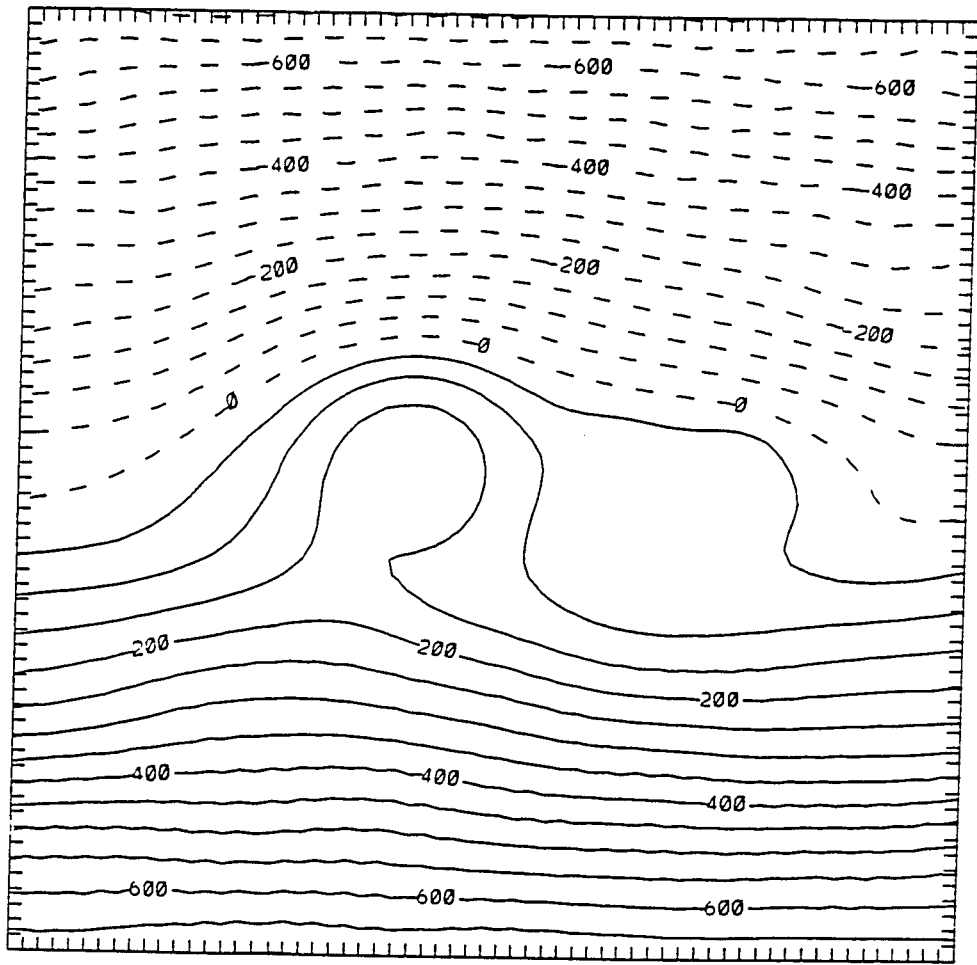
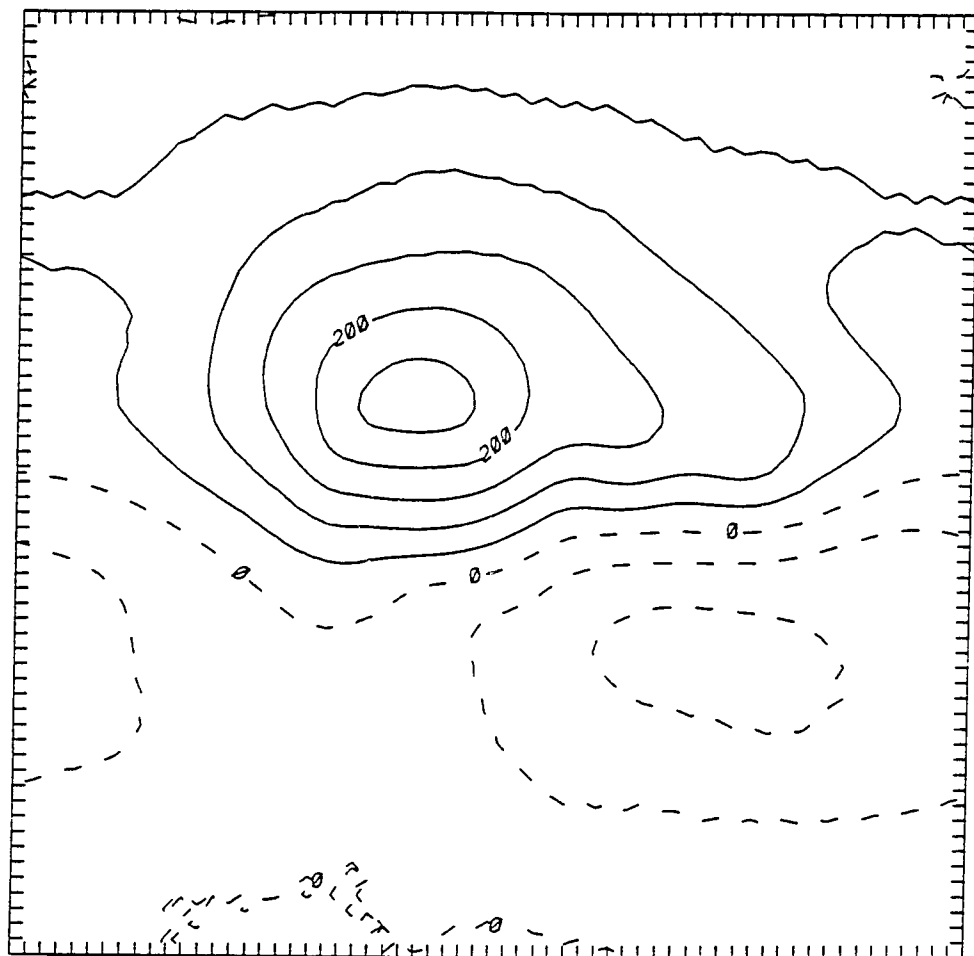


Figure 4.10: Barotropic response of the Fieberling Guyot at day 150 of the simulation. (a) Sea-surface height. Range is  $\pm 7$  cm. (b) Sea-surface-height anomaly due to seamount. Range is  $\pm 3$  cm. (c) Difference between 2 km and 4 km resolution experiments. Range is  $\pm 1$  mm. (d) Potential vorticity field, showing some water leaking off of the SE corner of the seamount.



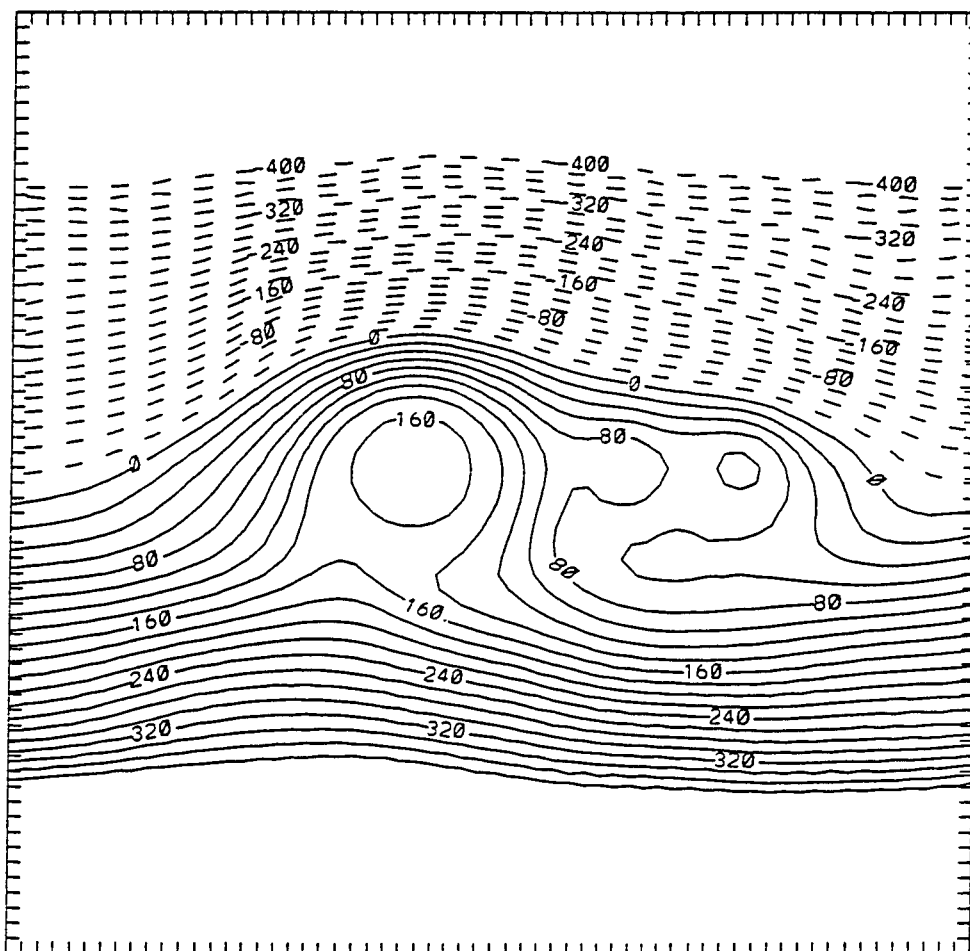
JR FROM -0.70000E-01 TO 0.70000E-01 CONTOUR INTERVAL OF 0.50000E-02 PT(3.31) = 0.63593E-01 LABELS SCALED BY 10000

Figure 4.11: Sea-surface height at day 300 for the barotropic Fieberling Guyot experiment with three seamounts. The range is  $\pm 7$  cm.



JR FROM -0.70000E-01 TO 0.70000E-01 CONTOUR INTERVAL OF 0.50000E-02 PT(3,31) = -0.10325E-02 LABELS SCALED BY 10000

Figure 4.12: Anomaly of the SSH due to barotropic flow over three seamounts of the Fieberling Guyot chain at day 300.



JR FROM -0.40000E-01 TO 0.38000E-01 CONTOUR INTERVAL OF 0.20000E-02 PT(3,31)= 0.63593E-01 LABELS SCALED BY 10000

Figure 4.13: Close-up of the important SSH anomaly contours for the barotropic flow over three seamounts on day 300.

was run with resolutions of 16, 8, 4, and 2 km, with the 2 km case assumed to be the exact solution. The topography was defined on each grid by the three Gaussian shapes defined above, and then was smoothed separately for each case with a single pass of a Wallington filter (Navon and Riphagen, 1979). The Wallington filter consists of two fourth-order (5-point) filters with staggered poles. It identically removes the  $2\Delta x$  signal, but damps the  $4\Delta x$  and longer components much less than a simple Hanning filter. This filtering was deemed necessary to avoid exciting short waves in the solution, which would have led to stability problems.

Figure 4.14 shows the normalized maximum error and normalized RMS error for each of the cases relative to the 2 km resolution case. The figure shows a decrease in error of approximately 3 for each doubling of the resolution. The discrepancy from the expected value of 4 is believed to be primarily due to the smoothing of the topography. The time discretization errors differ for the four cases since proportionately longer time steps were taken for the cases with coarser resolution, however the solution was very nearly steady, so these time differencing errors should not be a major influence. It is important to note that this test does not demonstrate the quadratic convergence of the model for a fixed (coarse-grid) geometry, though the results are consistent with quadratic convergence. What the test *does* suggest is that the fine scales present in the topography in the higher-resolution tests cases cause the sequence of experiments to converge at a rate slightly slower than quadratic.

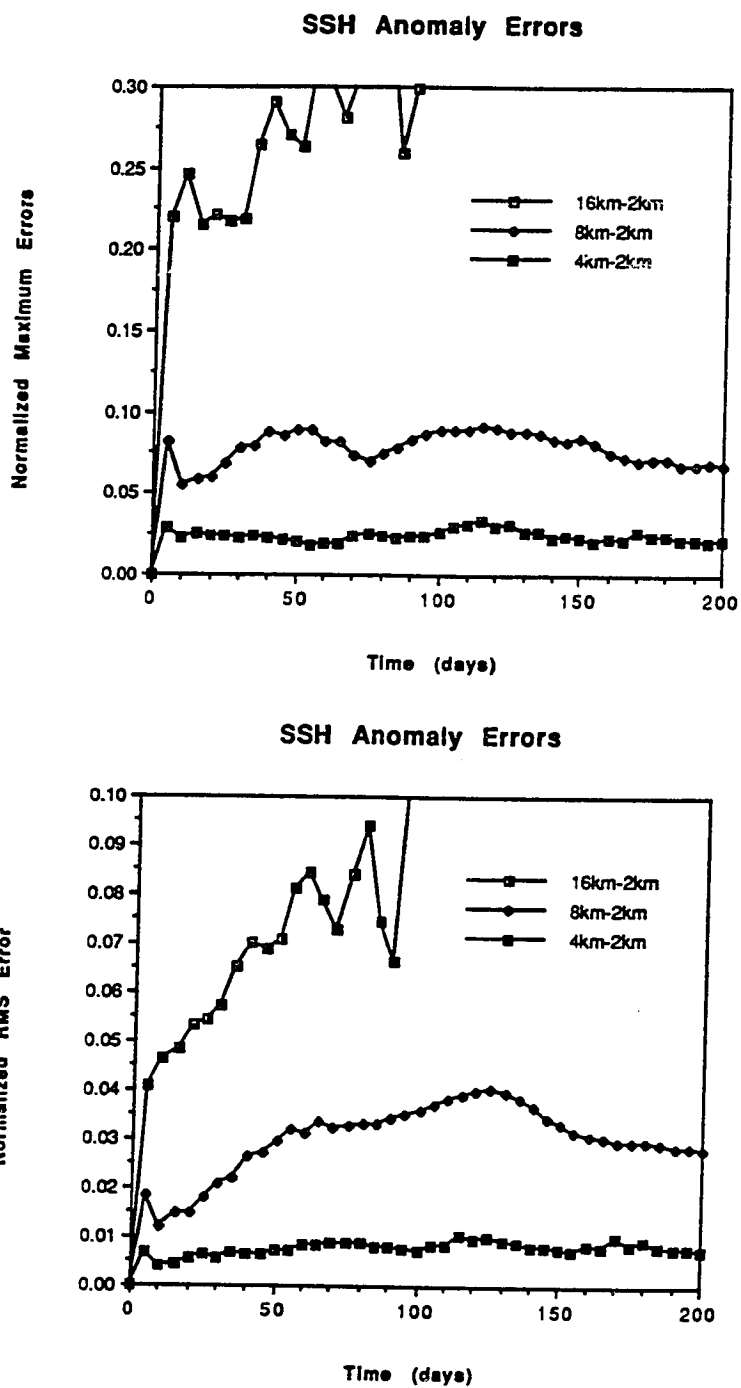


Figure 4.14: Error norms of the Barotropic flow for the three-seamont case at various resolutions. (a) Normalized maximum error. (b) Normalized RMS error.



# Chapter 5

## Baroclinic Model Tests

It is substantially more difficult to find useful baroclinic test cases than to find useful barotropic test cases, since there is so much more experience with layered models than with three-dimensional models. The difficulty is compounded by the fact that it is quite difficult to calculate the vertical modes of the current model because of the nonlinear vertical stretching and the non-local derivatives in the finite-element scheme. Therefore the tests shown below are somewhat more qualitative than the previous cases. Each of the modules of the model (*e.g.* the calculation of vertical velocity, vertical advection, pressure, etc.) was tested extensively against analytic solutions, so the following test cases exist mostly to see if the modules fit together properly and if the boundary conditions are handled correctly.

### 5.1 Single-Gyre Tests

The classical Stommel model for wind-driven ocean circulation is not well-suited for a stratified model, as the stratification hides the bottom friction from the baroclinic flow, and the upper layer flow accelerates to unrealistic velocities. The Munk model uses lateral friction as the energy sink, and this is perfectly suited

to a stratified model.

The model shows the desired qualitative behavior for this test case. The Ekman convergence in the upper layers causes an increase in sea-surface height and a deepening of the thermocline. Associated with this comes the expected clockwise gyre circulation. The temperature at 533 m after 50 days of integration in one test run are presented in Fig. 5.1. The asymmetry in the field is caused by upwelling in the NW and SE quadrants where the wind is blowing the water offshore, and downwelling in the NE and SW quadrants where the wind is blowing the water onshore. The westward intensification of the gyre is clearly beginning, though the response is still linear at this point in the integration.

Some interesting numerical anomalies show up in this test case as well. The most obvious is that the finite-element vertical discretization does not preserve the extrema of the temperature field at the top and bottom boundaries. In a finite-difference model, the bottom temperature minimum is guaranteed since there is no velocity through the bottom boundary. Since the advection equation is evaluated pointwise, the advection term therefore vanishes. In the finite-element scheme this is not so. The vertical advection term is integrated over the entire interval, so that the effective vertical velocity at the bottom node is not zero. If there is a gradient of temperature between the bottom two nodes, then the temperature of the bottom node may decrease, despite the fact that the flux is known to be zero across the boundary. Of course, since the finite-element scheme is a Galerkin scheme, the total temperature is actually conserved by the advective part of the equations. This is an example of how an integral scheme can produce pointwise errors while minimizing a global error norm.

The other numerical anomaly that shows up in these cases (as well as in the

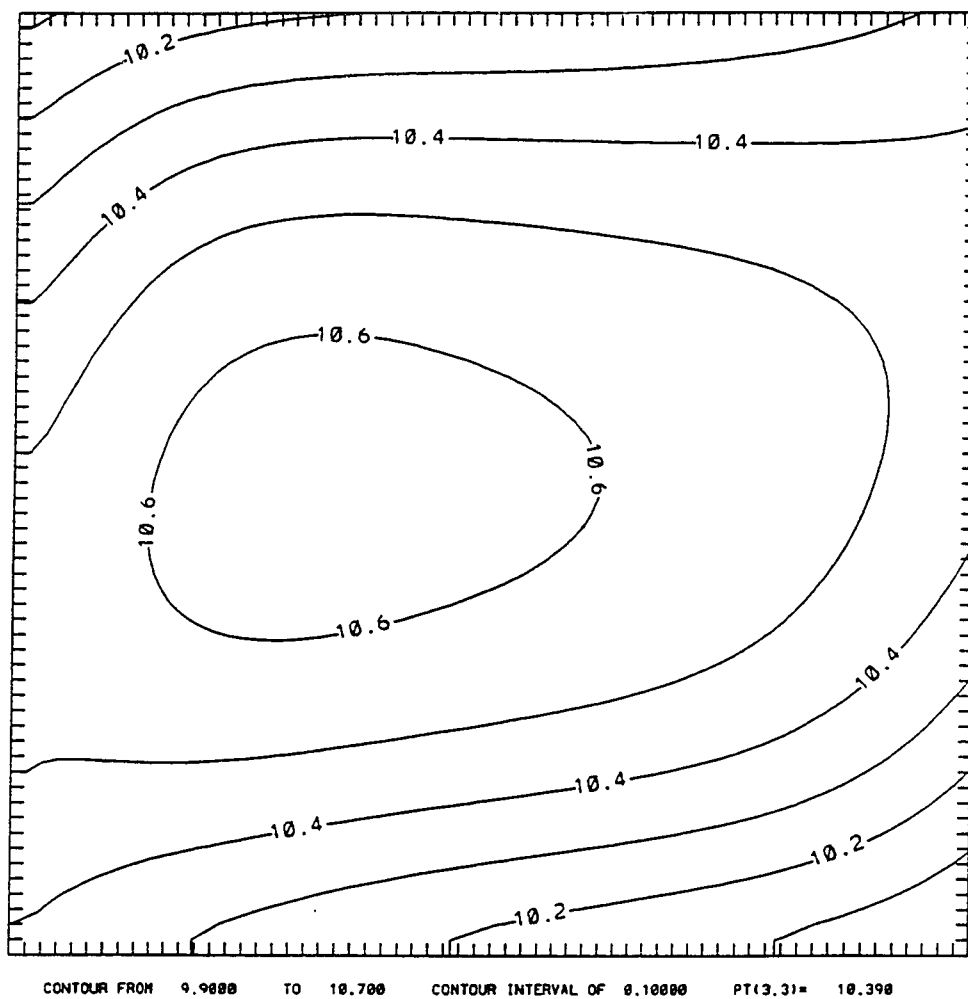


Figure 5.1: Temperature at 533 m at day 50 of a baroclinic single-gyre calculation.

channel cases discussed below) is related to the boundary conditions on pressure and sea-surface height. The boundary conditions required for the implicit integration of  $\eta$  depend on knowledge of the vertical integral of the normal gradient of the perturbation pressure at the boundaries. It is not possible to externally specify this boundary condition, since the system is fully specified by the boundary conditions on velocity and temperature. Therefore a boundary condition which is already implied by the equations must be discovered, as was discussed in an earlier section. Experiments with the combined barotropic/baroclinic code have demonstrated that the stability of the model is quite sensitive to the particular estimate employed for the normal gradient of perturbation pressure. The best results so far have been obtained with a simple linear extrapolation of the perturbation pressure gradient, but these calculations tend to gradually become unstable after about 10,000 steps. The instability manifests itself as  $2\Delta x$  noise in the velocity fields near (and tangential to) the boundary. This noise is much easier to produce in this model than in a rigid-lid model because the boundary condition is on the normal gradient of  $\eta$ , while the rigid-lid case has a boundary condition on the tangential gradient of  $\eta$  which clamps it to a single value along closed boundaries. Further work is in progress to identify the precise cause of the instability and to develop means to eliminate it.

## 5.2 Channel Tests

In this series of tests, the geometry was set up to be a recirculating channel, closed on the north and south boundaries. The solution for the baroclinic case is quite different than the barotropic case for this geometry. In the barotropic case, one observes a linear sea-surface height anomaly balancing a uniform zonal

current. In the baroclinic case, one finds a meridional cell superimposed on this basic circulation. The surface flow has a southward component due to the Ekman drift. Upwelling occurs at the northern boundary and downwelling at the southern boundary as the water turns under and flows back north at depth. This configuration was run successfully for 100 days of simulated time.

The next step was to include a seamount in the middle of the channel to test the baroclinic code's treatment of the terms introduced by topography. The seamount was modelled after the Fieberling Guyot, with a 12 km  $e$ -folding scale, but was employed with various heights, ranging from 400 m to 3000 m.

The primary activity in the baroclinic tests has been to attempt to overcome the problems caused by the imperfect cancellation of the two components of the baroclinic pressure gradient term for the case of flat isopycnals:

$$\nabla p' + g\bar{\rho}'\nabla z. \quad (5.1)$$

In the case of an initially resting fluid with flat isopycnals and non-flat topography, these terms do not identically cancel — thus producing spurious accelerations. Although the precise cause is not known, for sufficiently steep topography intersecting stratified water, this energy input to the system causes catastrophic instability. This problem, which will be quantified by some examples below, has also been observed by Haidvogel in his sigma-coordinate model (Haidvogel, personal communication).

A two-dimensional Taylor series expansion of the  $x$ -component of the pressure gradient vector shows that the error is due to the incomplete cancellation of two of the ten second-order truncation error terms, specifically the third derivatives in  $x$  of the  $p$  and  $z$  functions. Working out the expansions and assuming that the density field is linear in  $z$  and uniform in  $x$  leaves the following expression for the

error in the right-hand-side of the u-momentum equation

$$- 2\Delta t \frac{1}{\rho_0} \frac{1}{24} \Delta x^2 \left[ \frac{\partial^3 p'}{\partial x^3} + g\rho' \frac{\partial^3 z}{\partial x^3} \right]. \quad (5.2)$$

By use of the hydrostatic relation, it can be seen that the two terms scale like

$$\frac{1}{24} \frac{g\hat{\rho}\Delta x^2 A_z}{L_x^3}, \quad (5.3)$$

where  $\hat{\rho}$  is a characteristic scale for the variations in  $\rho'$ ,  $A_z$  is a characteristic height of the topography, and  $L_x$  is a characteristic horizontal scale for the topography. Now assuming the following scaling numbers for the baroclinic cases tested here:  $A = 1000$  m,  $L = 12000$  m,  $\Delta t = 600$  s,  $\hat{\rho} = 1$  kg m<sup>-3</sup>,  $\Delta x = 4000$  m, then the error term (and hence  $\Delta u$  over one time step) is approximately  $5 \times 10^{-3}$  m s<sup>-2</sup>.

This is a large acceleration, oceanographically, as it would produce flows of about 30 cm s<sup>-1</sup> after one day. The test cases here did not observe such large errors, probably due to partial cancellation of the error terms, but the errors observed were of the same order of magnitude. It is clear that extreme caution must be used with this technique since the upper bound on the spurious acceleration is so large.

Two approaches for ameliorating this problem are tested here. The “heating” technique consists of attempting to find the minimum potential energy state of the resting ocean by heating a stationary, homogeneous fluid from above, without any lateral viscosity. This is based on the hypothesis that the energy that goes into the flow is available because the model has a slightly different idea of what the minimum potential energy state is than the user. The “re-normalization” technique simply consists of calculating the pressure imbalance for an initial resting state, and subtracting that imbalance at every time step. The technique is expected to have trouble if the flow causes the density field

Seamount Amplitude (m)	Time to Blowup (days)	Surface Temperature
400	> 80	0
1000	> 80	0
1500	> 80	0
2000	25	0
3000	11	0
1000	20	15
1000	53	10
1000	58	5

Table 5.1: Stability of test cases with topography. The table shows the number of model days before the model went unstable as a function of the seamount amplitude and the temperature gradient. The temperature gradient was defined to be linear over the far-field depth, and is quantified by the surface temperature.

to change markedly from the initial conditions, but should work well for cases without strong baroclinicity near the topography.

The tests performed with the “heating” technique were all failures. In the presence of topography, the heat was not transmitted uniformly (in  $z$ ) and therefore caused lateral pressure gradients and associated large currents. The cases all became unstable after a few days of integration.

The tests performed with the “re-normalization” of the pressure gradient terms were somewhat more successful. A variety of seamount sizes and stratification strengths were tried, as summarized in table 5.1. Without the renormalization, the cases with strong topography became unstable in less than two days of simulation time.

The stability of the scheme was greatly improved by occasional filtering of the velocity and sea-surface height fields. The results shown in table 5.1 included one pass of a Wallington filter every 19 time steps. The Wallington filter consists of consecutive passes of two 5-point, fourth-order filters. It identically removes

the  $2\Delta x$  wave, and is only weakly damping for waves longer than  $6\Delta x$ . Since it is a fourth-order filter, it corresponds to the addition of biharmonic viscosity in the momentum equations. It acts much the same as a de-aliasing operator for the momentum equations.

By increasing the frequency of the filtering operations from every 19 time steps to every 5 time steps, the stability of the 1000 m,  $5^\circ$  case was extended to beyond 100 days. It is not possible to apply the same strategy for filtering to the temperature field, however, so short-scale noise is not completely eliminated from the system. When filtering is applied to the temperature field along  $s$  surfaces, it causes unphysical pressure gradients and spurious flows around the topography. This leads to inaccurate results and eventual instability.

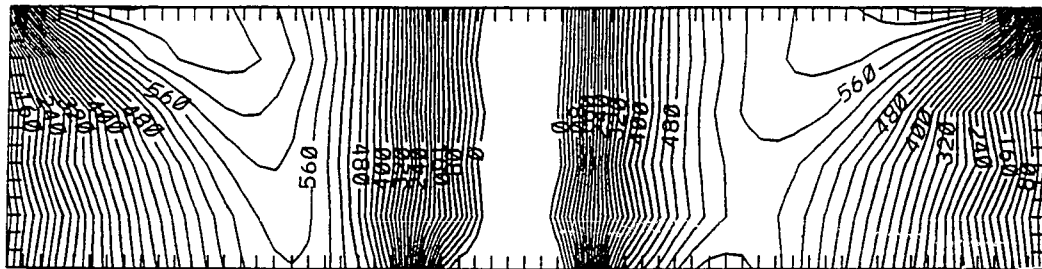
Three sections from this experiment are shown in Fig. 5.2. The top frame is a meridional section of the zonal velocity through the seamount center. Note that the vertical axis of the figure is  $s$  rather than  $z$ , so the seamount is not visible. The seamount is located in the center of the domain, with a lateral  $e$ -folding scale of three tick marks in the left-right direction. The immediately evident features of the flow are the boundary layers along the north and south walls, the Taylor column above the seamount and the surface-intensified baroclinic jet in between.

The middle frame of Fig. 5.2 is the temperature field along the same axis as top frame (the zonal velocity). The depression of the isotherms in the center of the domain is simply a manifestation of the coordinate transformation. The dynamically interesting part of this figure is the downwelling at the southern boundary and upwelling at the northern boundary. Note that this vertical motion is restricted to the upper level, which is consistent with the surface intensification of the zonal velocity field.

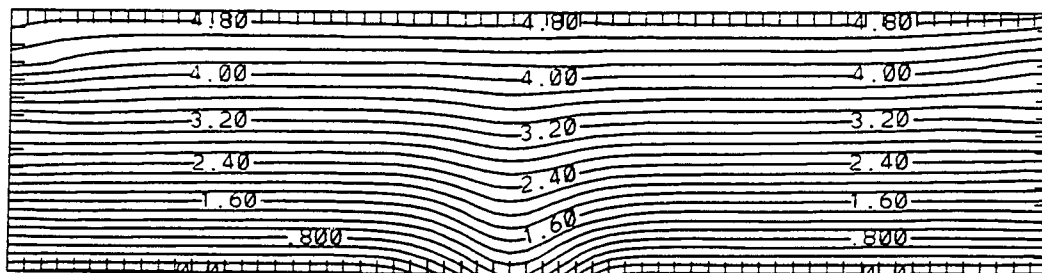


The bottom frame of Fig. 5.2 is a zonal cross-section of the meridional velocity field. The southward velocities of the surface Ekman layer are present everywhere except over the top of the seamount, where the water is nearly stationary. On the leading edge of the seamount there is a northward bottom current reminiscent of the northward flow observed in the barotropic experiments. As the topography gets higher (still on the upstream side), the flow becomes southward, then northward again at the top and along the downstream side.

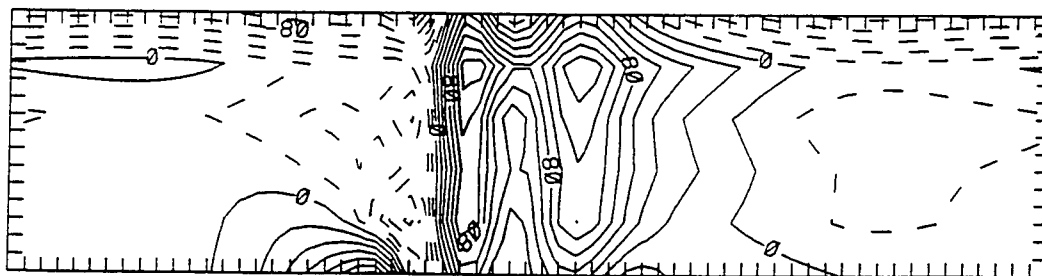
This meridional velocity profile is very difficult to analyze, since it is not possible to distinguish flow due to errors in the pressure gradient term with the “correct” results. Since the pressure gradient error term is so large, it is impossible to know how much of the “re-normalization” is incorrect due to the change in the density field. It is very easy to imagine a situation for which one can come up with a “plausible” explanation for the model’s behavior, when in fact the model’s behavior is merely an artifact of the incorrect pressure gradient terms.



JR FROM 0.00000E+00 TO 0.70000E-01 CONTOUR INTERVAL OF 0.20000E-02 PT(3,3)= 0.16576E-01 LABELS SCALED BY 10000



CONTOUR FROM 0.00000E+00 TO 5.0000 CONTOUR INTERVAL OF 0.20000 PT(3,3)= 0.00116



JR FROM -0.16000E-01 TO 0.16000E-01 CONTOUR INTERVAL OF 0.20000E-02 PT(3,3)= -0.09629E-03 LABELS SCALED BY 10000

Figure 5.2: Sections of three-dimensional flow over seamount at day 50. (top) Meridional section of zonal velocity. The southern boundary is on the left. (middle) Meridional section of temperature. (bottom) Zonal section of meridional velocity. Positive values are northward flows. The west end of the channel is on the left.

# Chapter 6

## Summary and Conclusions

The task of developing a three-dimensional primitive equation ocean model is a difficult and complex one. It is difficult because of the breadth of the problem implied in the wide range of physical processes contained in the primitive equations, and it is complex because of the subtleties of the relationships between the finite numerical methods and the continuous governing equations. This study has contributed to the enterprise of ocean modelling in several ways, including the development and implementation of a new model and the analysis of several numerical techniques applicable to ocean simulations.

A three-dimensional numerical model employing a vertical boundary-fitted coordinate and finite-element vertical representation was produced. The model combines a novel vertical mapping with linear Galerkin finite elements to obtain fourth-order accuracy in the vertical discretization. This is contrasted with the first-order accuracy of current non-uniformly-spaced finite-difference models.

The barotropic part of this code was used for a variety of experiments to study the flow over a chain of seamounts modelled after Fieberling Guyot and its neighbors. A careful analysis of the convergence of the finite-difference scheme suggests that a resolution of at least 3 grid points per characteristic scale of the

topography is necessary to obtain convergence to within 1% of the continuous solution. The inclusion of finer scales in the topography for the higher resolution cases also decreased the rate of convergence of the scheme to less than quadratic, though still faster than linear.

The model appears to have met the goals of efficiency and modularity. The vertical discretization appears to be effective and accurate in flat-bottom cases. On the negative side, the problems associated with the imperfect cancellation of the pressure gradient terms in the presence of topography and stratification have not yet been overcome. These problems include spurious flows in the vicinity of topography and numerical instability. Attempts to overcome these problems by (1) heating an initially homogeneous fluid from above; and (2) subtracting off the pressure gradient error (calculated from an initial resting state) have not been successful enough to warrant much confidence in the techniques.

Several other results of the current research have been in the evaluation of numerical techniques for the primitive equations. The semi-Lagrangian and semi-implicit integration schemes have been studied in some detail, and the effects of the sigma-coordinate transformation on the pressure gradient calculation have been investigated.

The semi-Lagrangian advection scheme was analyzed to establish quantitative measures of the implied dissipation. Formulae are provided to estimate the equivalent Laplacian eddy-viscosity (for linear interpolation) or biharmonic eddy-viscosity (for quadratic or cubic interpolation) as a function of grid spacing and time step. For the grid resolutions currently used in ocean models, the semi-Lagrangian scheme was shown to contain excessive implied diffusion for long-term integrations, and so was not used in the present model. On the other hand, the

excellent phase response of the semi-Lagrangian scheme makes it ideally suited for short-term integrations involving tracers, such as pollutant or oil-spill trajectory modelling, or in the atmospheric forecast models where it is now popular.

The three-dimensional version of the semi-implicit scheme was analyzed for possible application to three-dimensional ocean models. It was shown that the scheme is physically ill-posed in the limit as the stratification of the fluid becomes neutral. The scheme is still arithmetically well-posed, however. Further research is required to analyze the precise nature of the error introduced by the semi-implicit scheme and to document its consequences for realistic profiles of vertical stratification.

# Bibliography

- Abramopoulos, F. (1988). Generalized energy and potential enstrophy conserving finite difference schemes for the shallow water equations. *Monthly Weather Review*, 116:650–662.
- Abramowitz, M. and Stegun, I. (1972). *Handbook of Mathematical Functions*. Dover.
- Bates, J. (1984). An efficient semi-Lagrangian and alternating direction implicit method for integrating the shallow water equations. *Monthly Weather Review*, 112:2033–2047.
- Bates, J. and McDonald, A. (1982). Multiply-upstream, semi-Lagrangian schemes: Analysis and application to a multi-level primitive equation model. *Monthly Weather Review*, 110:1831–1842.
- Batteen, M. (1988). On the use of sigma coordinates in large-scale for ocean circulation models. published in the *Ocean Modelling* newsletter.
- Beland, M., Cote, J., and Staniforth, A. (1983). The accuracy of a finite-element vertical discretization scheme for primitive equation models: Comparison with a finite-difference scheme. *Monthly Weather Review*, 111:2298–2318.

- Bleck, R. and Boudra, D. (1981). Initial testing of a numerical ocean circulation model using a hybrid (quasi-isopycnic) vertical coordinate. *Journal of Physical Oceanography*, 11:755–770.
- Bleck, R. and Boudra, D. (1986). Wind-driven spin-up in eddy-resolving models formulated in isopycnal and isobaric coordinates. *Journal of Geophysical Research*, 91:7611–7621.
- Bleck, R. and Smith, L. (1989). A wind-driven isopycnic coordinate model of the north and equatorial atlantic ocean. part i: Model development and supporting experiments. *Journal of Geophysical Research*, to appear.
- Bryan, K. (1963). A numerical investigation of a non-linear model of a wind-driven ocean. *Journal of the Atmospheric Sciences*, 20:594–606.
- Bryan, K. (1969). A numerical method for the study of the circulation of the world ocean. *Journal of Computational Physics*, 4:347–376.
- Busalacchi, A. J. and O'Brien, J. J. (1980). The seasonal variability in a model of the tropical pacific. *Journal of Physical Oceanography*, 10:1929–1951.
- Campana, K. (1979). Higher order finite difference experiments with a semi-implicit model at NMC. *Monthly Weather Review*, 107:363–376.
- Cane, M. A. (1986). Introduction to ocean modeling. In O'Brien, J. J., editor, *Advanced Physical Oceanographic Numerical Modelling*, pages 5–22. Reidel.
- Chang, H.-R. and Shirer, H. N. (1985). Compact spatial differencing techniques in numerical modeling. *Monthly Weather Review*, 113:409–423.

- Cote, J. and Staniforth, A. (1988). A two-time-level semi-Lagrangian semi-implicit scheme for spectral models. *Monthly Weather Review*, 116:2003–2012.
- Cox, M. D. (1987). An eddy-resolving numerical model of the ventilated thermocline: Time dependence. *Journal of Physical Oceanography*, 17:1044–1056.
- Cullen, M. J. P. (1979). The finite element method. In *Numerical Methods used in Atmospheric Models, Volume II*, GARP Publication #17, chapter 5, pages 300–337. ICSU/WMO.
- Cushman-Roisin, B. (1984). Toward a unified theory of geostrophic regimes: Homogeneous and stratified systems. Unpublished Manuscript.
- Davies, A. M. (1987). Spectral models in continental shelf sea oceanography. In Heaps, N. S., editor, *Three-Dimensional Coastal Ocean Models*, volume 4 of *Coastal and Estuarine Sciences*, pages 71–106. American Geophysical Union.
- Duff, I. S. and Reid, J. K. (1983). The multifrontal solution of indefinite sparse symmetric linear systems. *ACM Transactions on Mathematical Software*, 9:302–325.
- Duff, I. S. and Reid, J. K. (1984). The multifrontal solution of unsymmetric sets of linear equations. *SIAM Journal on Scientific and Statistical Computing*, 5:633–641.
- Fletcher, C. A. J. (1984). *Computational Galerkin Methods*. Springer-Verlag.
- Flierl, G. R. (1977). The application of linear quasigeostrophic dynamics to gulf stream rings. *Journal of Physical Oceanography*, 7:365–379.



- Gargett, A. E. (1986). Small-scale parameterization in large-scale ocean models. In O'Brien, J. J., editor, *Advanced Physical Oceanographic Numerical Modelling*, pages 144–154. Reidel.
- Gent, P. and McWilliams, J. (1983). The equatorial waves of balanced models. *Journal of Physical Oceanography*, 13:1179–1192.
- Grammeltveldt, A. (1969). A survey of finite difference schemes for the primitive equations for a barotropic fluid. *Monthly Weather Review*, 97:384–404.
- Grotjahn, R. and O'Brien, J. J. (1976). Some inaccuracies in finite differencing hyperbolic equations. *Monthly Weather Review*, 104:180–194.
- Haltiner, G. and Williams, R. (1979). *Numerical Prediction and Dynamic Meteorology*. Wiley.
- Hartmann, D. (1988). On the comparison of finite-element to finite-difference methods for the representation of vertical structure in model atmospheres. *Monthly Weather Review*, 116:269–273.
- Hurlburt, H. and Thompson, J. (1980). A numerical study of loop current intrusions and eddy shedding. *Journal of Physical Oceanography*, 10:1611–1651.
- Jensen, T. G. and Kopriva, D. A. (1988). Comparison of a finite difference and a spectral collocation reduced gravity ocean model. Fsu-scri-88-65, Supercomputer Computations Research Institute.
- Kalnay de Rivas, E. (1972). On the use of nonuniform grids in finite-difference equations. *Journal of Computational Physics*, 10:202–210.

- Kreiss, H. and Olinger, J. (1973). Methods for the approximate solution of time dependent problems. Garp publication #10, ICSU/WMO.
- Kwizak, M. and Robert, A. (1971). A semi-implicit scheme for grid-point atmospheric models of the primitive equations. *Monthly Weather Review*, 99:32–36.
- Leith, C. E. (1968). Two dimensional eddy viscosity coefficients. In *Proc. WMO/IUGG Symposium on Numerical Weather Prediction*, pages I,41–44.
- LeProvost, C. (1986). On the use of finite element methods for ocean modelling. In O'Brien, J. J., editor, *Advanced Physical Oceanographic Numerical Modelling*, pages 557–580. Reidel.
- Madala, R. and Piacsek, S. (1977). A semi-implicit numerical model for baroclinic oceans. *Journal of Computational Physics*, 23:167–178.
- McCalpin, J. D. (1988). A quantitative analysis of the dissipation inherent in semi-Lagrangian advection. *Monthly Weather Review*, 116:2330–2336. Also available as technical report FSU-SCRI-88-08.
- McCalpin, J. D. (1989). A note on the use of the semi-implicit scheme for three-dimensional ocean models. Technical Report FSU-SCRI-89-14, Supercomputer Computations Research Institute, The Florida State University.
- McDonald, A. (1984). Accuracy of multiply-upstream, semi-Lagrangian advective schemes. *Monthly Weather Review*, 112:1267–1275.
- McDonald, A. (1986). A semi-Lagrangian and semi-implicit two-time-level integration scheme. *Monthly Weather Review*, 114:824–830.

- McDonald, A. (1987). Accuracy of multiply-upstream, semi-Lagrangian advective schemes ii. *Monthly Weather Review*, 115:1446–1450.
- McWilliams, J. C. and Flierl, G. R. (1979). On the evolution of isolated mesoscale vortices, with application to gulf stream rings. *Journal of Physical Oceanography*, 9:1155–1182.
- McWilliams, J. C. and Gent, P. R. (1980). Intermediate models of planetary circulations in the atmosphere and ocean. *Journal of the Atmospheric Sciences*, 37:1657–1678.
- Mellor, G. L. and Blumberg, A. F. (1985). Modeling vertical and horizontal diffusivities with the sigma coordinate system. *Monthly Weather Review*, 113:1379–1383.
- Mied, R. P. and Lindemann, G. J. (1979). The propagation and evolution of gulf stream rings. *Journal of Physical Oceanography*, 9:1183–1206.
- Munk, W. H. (1950). On the wind-driven ocean circulation. *J. Meteor.*, 7:79–93.
- Navon, I. M. and Riphagen, H. A. (1979). An implicit compact fourth-order algorithm for solving the shallow-water equations in conservation-law form. *Monthly Weather Review*, 107:1107–1127.
- Nof, D. (1983). On the migration of isolated eddies with application to gulf stream rings. *Journal of Marine Research*, 41:399–425.
- O'Brien, J. J. (1986a). The diffusive problem. In O'Brien, J. J., editor, *Advanced Physical Oceanographic Numerical Modelling*, pages 127–144. Reidel.

- O'Brien, J. J. (1986b). The hyperbolic problem. In O'Brien, J. J., editor, *Advanced Physical Oceanographic Numerical Modelling*, pages 165–186. Reidel.
- Oliger, J. and Sundstrom, A. (1978). Theoretical and practical aspects of some initial-boundary value problems in fluid dynamics. *SIAM Journal of Applied Mathematics*, 35:419–446.
- Orszag, S. A. (1971). On the elimination of aliasing in finite-difference schemes by filtering high-wavenumber components. *Journal of the Atmospheric Sciences*, 28:1074.
- Pares-Sierra, A. and Vallis, G. K. (1989). A fast semi-direct method for the numerical solution of non-separable elliptic equations in irregular domains. *Journal of Computational Physics*, 82:398–412.
- Pedlosky, J. (1979). *Geophysical Fluid Dynamics*. Springer-Verlag.
- Peters, H., Gregg, M., and Toole, J. (1988). On the parameterization of equatorial turbulence. *Journal of Geophysical Research*, 93:1199–1218.
- Pudykiewicz, J. and Staniforth, A. (1984). Some properties and comparative performance of the semi-Lagrangian method of Robert in the solution of the advection-diffusion equation. *Atmosphere-Ocean*, 22:283–308.
- Purnell, D. K. (1976). Solution of the advection equation by upstream interpolation with a cubic spline. *Monthly Weather Review*, 104:42–48.
- Redi, M. H. (1982). Oceanic isopycnal mixing by coordinate rotation. *Journal of Physical Oceanography*, 12:1154–1158.

- Ritchie, H. (1986). Eliminating the interpolation associated with the semi-Lagrangian scheme. *Monthly Weather Review*, 114:135–146.
- Ritchie, H. (1988). Application of the semi-Lagrangian method to a spectral model of the shallow water equations. *Monthly Weather Review*, 116:1587–1598.
- Robert, A., Henderson, J., and Turnbull, C. (1972). An implicit time integration scheme for baroclinic models of the atmosphere. *Monthly Weather Review*, 100:329–335.
- Robert, A., Yee, T., and Ritchie, H. (1985). A semi-Lagrangian and semi-implicit numerical integration scheme for multilevel atmospheric models. *Monthly Weather Review*, 113:388–394.
- Semtner, A. (1986a). Finite-difference formulation of a world ocean model. In O'Brien, J. J., editor, *Advanced Physical Oceanographic Numerical Modelling*, pages 187–202. Reidel.
- Semtner, A. (1986b). History and methodology of modelling the circulation of the world ocean. In O'Brien, J. J., editor, *Advanced Physical Oceanographic Numerical Modelling*, pages 23–32. Reidel.
- Smith, D. and Reid, R. O. (1982). A numerical study of nonfrictional decay of mesoscale eddies. *Journal of Physical Oceanography*, 12:244–255.
- Stommel, H. (1948). The westward intensification of wind-driven ocean currents. *Trans. Amer. Geophys. Union*, 99:202–206.

- Takano, K. and Wurtele, M. (1982). A fourth order energy and potential enstrophy conserving difference scheme. Technical report, Air Force Geophysics Laboratory. AFGL-TR-82-0205 (NTIS AD-A126626).
- Veronis, G. (1966). Wind-driven ocean circulation – part 2. numerical solutions of the non-linear problem. *Deep-Sea Research*, 13:31–55.
- Verron, J. and Provost, C. L. (1985). A numerical study of quasi-geostrophic flow over isolated topography. *Journal of Fluid Mechanics*, 154:231–252.
- Wajsowicz, R. C. (1986). Free planetary waves in finite-difference numerical models. *Journal of Physical Oceanography*, 16:773–789.
- Williams, G. P. (1985). Geostrophic regimes on a sphere and a beta plane. *Journal of the Atmospheric Sciences*, 42:1237–1243.
- Williamson, D. L. (1988). The effect of vertical finite difference approximations on the NCAR community climate model. *Journal of Climate*, 1:40–58.
- Williamson, D. L. and Browning, G. L. (1973). Comparison of grids and difference approximations for numerical weather prediction over a sphere. *Journal of Applied Meteorology*, 12:264–274.

# Appendix A

## The Dissipation of the Semi-Lagrangian Advection Scheme

### A.1 Introduction

In the search for more efficient numerical techniques for the integration of the atmospheric equations of motion, a number of authors have recently been experimenting with the so-called semi-Lagrangian advective scheme. This scheme works by back-tracking along particle trajectories and interpolating on the flow fields to update the values at the fixed grid points. It differs from a pure Lagrangian scheme in that the parcels followed are different at each time step. When the grid points used in the interpolation are the nearest neighbors to the parcel's departure point (rather than its arrival point), then the scheme is called "multiply-upstream." Advection with a multiply-upstream scheme is unconditionally stable.

There are many options in the implementation of semi-Lagrangian advection. Several authors have used a split scheme (Bates and McDonald, 1982; Bates, 1984), in which the equations are divided into pure advection and linear relax-

ation, and integrated independently. Then the time step for the advective portion can be based on accuracy considerations, rather than stability criterion. Alternatively, the equations may be integrated in a single step, with the non-advective terms being moved to the right-hand-side and evaluated along the trajectory (Robert et al., 1985; McDonald, 1986). For simplicity, the analysis here is for a pure advective scheme.

McDonald (McDonald, 1984; McDonald, 1987) has discussed the accuracy of semi-Lagrangian advection using Lagrangian interpolation schemes. He and others have noted its dissipation (Bates, 1984; Robert et al., 1985; Ritchie, 1988), but have not quantified it in terms of more common measures of viscosity. In this study, the dissipation inherent in semi-Lagrangian advection will be quantified in terms of the dissipative decay time scale and the effective eddy viscosity as functions of the horizontal scale and the residual Courant number.

## A.2 Amplification Factors

McDonald (McDonald, 1984) has calculated the amplification factors for a particular implementation of the semi-Lagrangian advection of plane waves using Lagrangian interpolation. The amplification factor of the Lagrangian interpolation scheme is separable into multiplicative  $x$  and  $y$  components, which makes the analysis much simpler. Since we are only concerned with the amplitudes here (not the phase), it is sufficient to deal with only the magnitudes of the amplification factors. Following McDonald, the interpolation points are chosen such that the fractional part of the Courant number lies between 0 and 1 for the cases of bilinear and bicubic interpolation, and between  $-\frac{1}{2}$  and  $+\frac{1}{2}$  for the cases of biquadratic and biquartic interpolation. Hereafter, the fractional part



of the Courant number will be referred to by  $\alpha$ , and will be called the “residual Courant number”. With the definition:  $c = 1 - \cos(k\Delta x)$ , the magnitudes of the amplification factors for the four schemes are thus:

$$\begin{aligned} |\lambda_1|^2 &= 1 - 2\alpha(1 - \alpha)c & (A.1) \\ |\lambda_2|^2 &= 1 - \alpha^2(1 - \alpha^2)c^2 \\ |\lambda_3|^2 &= 1 - \alpha(2 - \alpha)(1 - \alpha^2)c^2[3 + 2c\alpha(1 - \alpha)]/9 \\ |\lambda_4|^2 &= 1 - \alpha^2(1 - \alpha^2)(4 - \alpha^2)c^3[4 + c(1 - \alpha^2)]/36, \end{aligned}$$

where  $\alpha$  is the residual Courant number,  $k$  is the wavenumber, and  $\Delta t$  and  $\Delta x$  are the usual finite difference time and space increments. The subscript indicates the order of the interpolation.

Needless to say, these are not the only possible choices for the interpolation. Spline interpolations are known to have some properties that are superior to Lagrangian interpolation, and have been used with semi-Lagrangian advective schemes (Purnell, 1976; Pudykiewicz and Staniforth, 1984). Low-order trigonometric interpolations have also been investigated for semi-Lagrangian advection in storm surge modelling (R.O. Reid, personal communication). Therefore, the details of a particular implementation may differ from the results presented here, but the orders of accuracy should be the same for varying interpolation techniques.

### A.3 Decay time scales and “equivalent” viscosity

The amplification factors shown above all have magnitudes less than or equal to unity, ensuring stability for the schemes. However, the magnitude of the

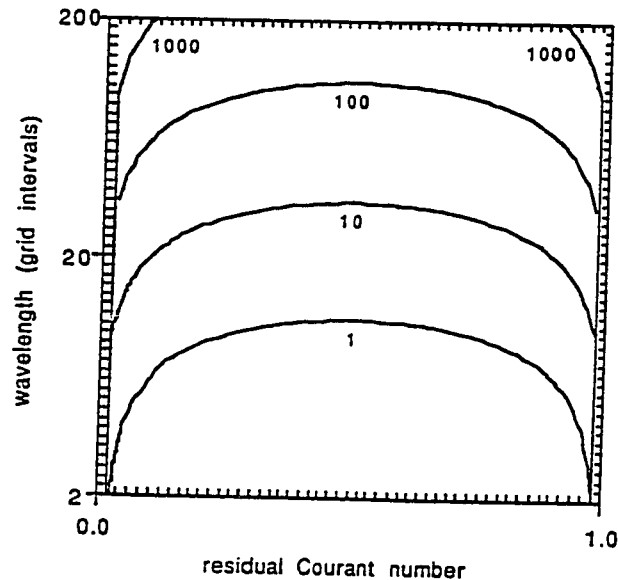


Figure A.1: Contours of the dissipation decay time scale in days as a function of residual Courant number ( $U\Delta t/\Delta x$ ) and wavelength for the case of one-dimensional semi-Lagrangian advection with linear interpolation. Note that the vertical axis and contour interval are logarithmic. The vertical contours near  $\alpha = 0$  and  $\alpha = 1$  are artifacts of the contouring.

amplification factor is not a very understandable measure of the dissipation in a finite-difference scheme (unless it is significantly smaller than 1 !). A much more easily understood measure is the dissipative decay time scale. This is defined as the time required to reduce a signal to  $e^{-1}$  times its original amplitude. In terms of the amplification factor, the decay time scale is

$$\tau = -\frac{\Delta t}{\ln |\lambda|}. \quad (\text{A.2})$$

An alternate representation of the magnitude of the dissipation is the coefficient of viscosity or hyperviscosity which produces the same damping. The dependence of the damping on the wavelength will show how the dissipation is more, or less, scale-dependent than the traditional Laplacian eddy viscosity formulation, which has a  $k^2$  spectral dependence.

The dependencies of the decay time scales on  $\alpha$  and wavelength for each of

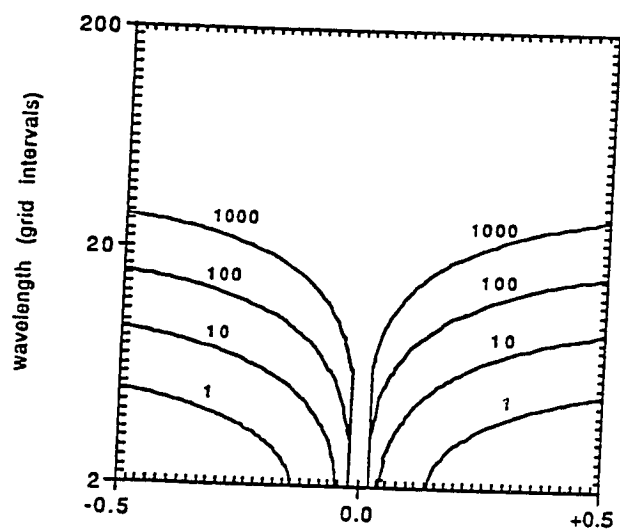


Figure A.2: As Fig. 1, but for quadratic interpolation.

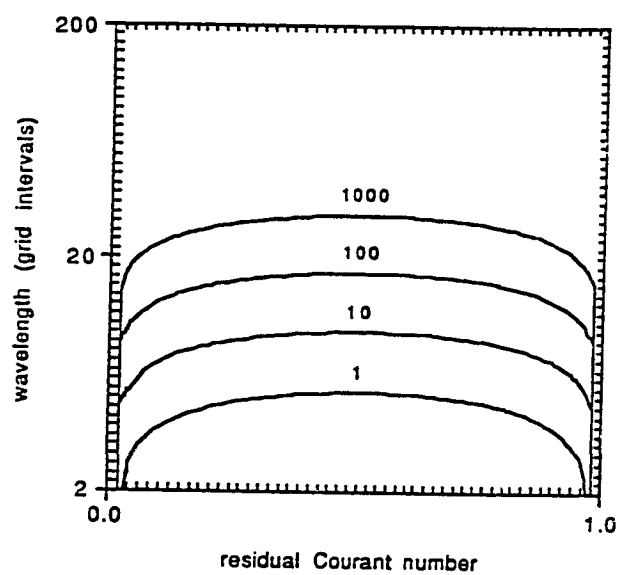


Figure A.3: As Fig. 1, but for cubic interpolation.

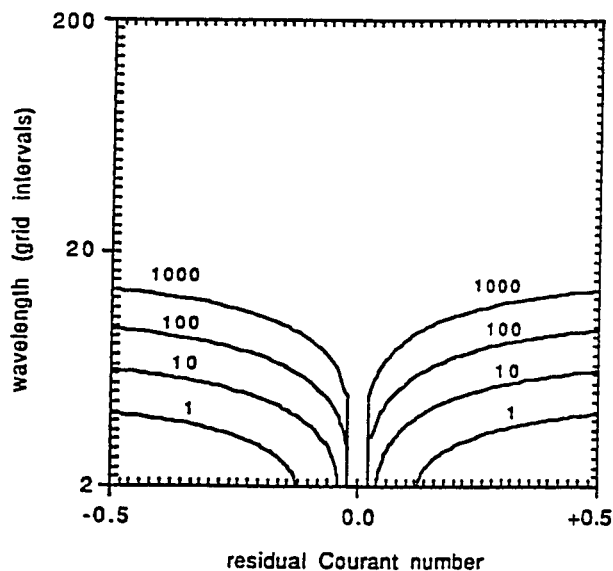


Figure A.4: As Fig. 1, but for quartic interpolation.

the four schemes described in the previous section are shown in Figs. 1-4. Note that the  $\alpha$  axis is linear, and that the wavelength axis and the contour interval are logarithmic. Note also that since the wavenumber dependence of the decay time scale appears only as  $k\Delta x$ , the vertical axis has been non-dimensionalized by  $\Delta x$ . The grid interval  $\Delta x$  also shows up in the residual Courant number, so the effects of time and space discretization cannot be entirely separated. This will be discussed in some detail in section A.5. The decay time scale is in units of days, for a time increment  $\Delta t = 3600\text{s}$ . When it is appropriate to use dimensional quantities, the values  $\Delta x = 200\text{km}$  and  $\Delta t = 3600\text{s}$  will be used as representative numbers. For this “typical” horizontal resolution the figures cover the two decades from the Nyquist cutoff on the short wave end, to the global mode 1 wave on the long wave end. Following sections will discuss the long-wave and short-wave characteristics of the semi-Lagrangian scheme separately.

### A.3.1 Long waves

For long waves ( $k\Delta x \ll 1$ ), the wavenumber dependent term in the amplification factors ( $1 - \cos(k\Delta x)$ ) reduces to approximately  $\frac{1}{2}(k\Delta x)^2$ . Inspection of (A.1) shows that linear interpolation has the same spectral characteristics as Laplacian viscosity and quadratic and cubic interpolation have the same spectral characteristics as biharmonic viscosity.

It may often be the case that the advecting velocity is only large in a portion of the computational domain. For the regions in which the Courant number is small, the amplification factors can be approximated:

$$\begin{aligned} |\lambda_1| &= 1 - \frac{1}{2}\alpha(k\Delta x)^2 \\ |\lambda_2| &= 1 - \frac{1}{8}\alpha^2(k\Delta x)^4 \\ |\lambda_3| &= 1 - \frac{1}{12}\alpha(k\Delta x)^4 \\ |\lambda_4| &= 1 - \frac{1}{36}\alpha^2(k\Delta x)^6. \end{aligned} \tag{A.3}$$

This shows clearly that the third-order scheme can have *more* dissipation than the second-order scheme, and that the spectral dependence of its diffusivity is the same. The third-order scheme does, however, have a better phase representation than the second-order scheme (as pointed out by McDonald (McDonald, 1984)).

Purnell (Purnell, 1976) and Pudykiewicz and Staniforth (Pudykiewicz and Staniforth, 1984) analyzed a cubic-spline interpolation from which can be obtained an analogous expression for  $|\lambda_3|$ , which reduces to

$$|\lambda_3| = 1 - \frac{1}{12}\alpha^2(k\Delta x)^4,$$

in this limit. This result shows that the cubic-spline interpolation has slightly less dissipation than the quadratic Lagrangian interpolation used here, but displays

the same spectral slope.

For these long waves, it is straightforward to calculate the equivalent eddy viscosity from the amplification factor. The analytic solution for the amplitude of a plane wave damped by Laplacian friction is

$$\hat{\psi}(k, t) = \hat{\psi}(k, 0)e^{-A_H k^2 t}.$$

The Taylor series expansion (in time) for the amplification factor is

$$|\lambda| = 1 - A_H k^2 \Delta t + O(\Delta t^2).$$

Then equate the first two terms of the long-wave expansion for the semi-Lagrangian step with these two terms and solve for  $A_H$ . The results are:

$$\begin{aligned} A_{H1} &= \frac{1}{2\Delta t}(\alpha - \alpha^2)\Delta x^2 \\ A_{H2} &= \frac{1}{8\Delta t}(\alpha^2 - \alpha^4)\Delta x^2(k\Delta x)^2 \\ A_{H3} &= \frac{1}{24\Delta t}(2\alpha - \alpha^2 - 2\alpha^3 + \alpha^4)\Delta x^2(k\Delta x)^2 \\ A_{H4} &= \frac{1}{144\Delta t}(4\alpha^2 - 5\alpha^4 + \alpha^6)\Delta x^2(k\Delta x)^4. \end{aligned}$$

Only the linear case has the  $k^2$  spectral dependence characteristic of Laplacian friction. Since  $\alpha$  is in the range 0–1, an upper bound to the equivalent Laplacian dissipation for this case is

$$A_{H1} \leq \frac{1}{2\Delta t} \left(\frac{1}{4}\right) \Delta x^2 = \frac{1}{8} \frac{\Delta x^2}{\Delta t}, \quad (\text{A.4})$$

which is approximately  $1.4 \times 10^6 \text{m}^2 \text{s}^{-1}$  for the parameters listed at the beginning of this section. For the atmosphere, values of the eddy diffusion coefficient have historically been estimated at less than  $10^6 \text{m}^2 \text{s}^{-1}$ , though it is generally accepted that Laplacian eddy viscosity is a rather poor approximation to the actual turbulent dissipation and diffusion in the atmosphere.

An analogous comparison may be made for biharmonic viscosity. The equivalent biharmonic viscosities are:

$$\begin{aligned}
 A_{B1} &= \frac{1}{2\Delta t}(\alpha - \alpha^2)\Delta x^4(k\Delta x)^{-2} \\
 A_{B2} &= \frac{1}{8\Delta t}(\alpha^2 - \alpha^4)\Delta x^4 \\
 A_{B3} &= \frac{1}{24\Delta t}(2\alpha - \alpha^2 - 2\alpha^3 + \alpha^4)\Delta x^4 \\
 A_{B4} &= \frac{1}{144\Delta t}(4\alpha^2 - 5\alpha^4 - \alpha^6)\Delta x^4(k\Delta x)^2.
 \end{aligned}$$

Noting the ranges available for  $\alpha$ , the upper bounds for the quadratic and cubic cases are:

$$\begin{aligned}
 A_{B2} &\leq \frac{1}{8\Delta t} \left(\frac{3}{16}\right) \Delta x^4 = \frac{3}{128} \frac{\Delta x^4}{\Delta t} \\
 A_{B3} &\leq \frac{1}{24\Delta t} \left(\frac{9}{16}\right) \Delta x^4 = \frac{3}{128} \frac{\Delta x^4}{\Delta t},
 \end{aligned} \tag{A.5}$$

which are both approximately  $1.0 \times 10^{16} \text{m}^4 \text{s}^{-1}$  for the parameters listed at the beginning of this section. It is difficult to define this non-physical dissipation observationally, but the European Center for Medium-Range Weather Forecasting high-resolution model uses values of about  $1.0 \times 10^{15} \text{m}^4 \text{s}^{-1}$  for medium range forecasts (Ritchie, 1988).

### A.3.2 Short Waves

For short waves, the term  $(1 - \cos(k\Delta x))$  does not display the same dependence on  $k$  as for the long waves. Two cases of special interest are wavelengths of  $2\Delta x$  and  $4\Delta x$ , for which the cosine terms reduce to  $2^n$  and 1, respectively, where  $n$  is the order of the interpolation. The dissipation still increases with increasing wavenumber, but it does so at a much slower rate than the appropriate power

of  $k$  near the shortest waves in the system. Thus, the equivalent eddy viscosity actually *decreases* for the shortest waves, and the effect gets worse as the order of the scheme increases. This is unfortunate, as one would usually desire *larger* dissipation in this wavelength range to damp out the poorly resolved (and inaccurate) short waves.

It is instructive to examine the amplification factors for these special cases, which are simply polynomials in  $\alpha$ :

$$L = 2\Delta x$$

$$|\lambda_1|^2 = 1 - 4\alpha + 4\alpha^2$$

$$|\lambda_2|^2 = 1 - 4\alpha^2 + 4\alpha^4$$

$$|\lambda_3|^2 = 1 - \frac{8}{3}\alpha - \frac{20}{9}\alpha^2 + 8\alpha^3 + \frac{4}{9}\alpha^4 - \frac{16}{3}\alpha^5 + \frac{16}{9}\alpha^6$$

$$|\lambda_4|^2 = 1 - \frac{16}{3}\alpha^2 + \frac{76}{9}\alpha^4 - \frac{32}{9}\alpha^6 + \frac{4}{9}\alpha^8$$

and,

$$L = 4\Delta x$$

$$|\lambda_1|^2 = 1 - 2\alpha + 2\alpha^2$$

$$|\lambda_2|^2 = 1 - \alpha^2 + \alpha^4$$

$$|\lambda_3|^2 = 1 - \frac{2}{3}\alpha - \frac{1}{9}\alpha^2 + \frac{4}{3}\alpha^3 - \frac{1}{9}\alpha^4 - \frac{2}{3}\alpha^5 + \frac{2}{9}\alpha^6$$

$$|\lambda_4|^2 = 1 - \frac{5}{9}\alpha^2 + \frac{29}{36}\alpha^4 - \frac{5}{18}\alpha^6 + \frac{1}{36}\alpha^8.$$

For small  $\alpha$ , these functional dependences demonstrate that the even-ordered schemes have similar dissipation for short scales, and that this dissipation is much less than that of the odd-ordered schemes (which also have similar dissipation). Figs. 1–4 show this to be true for the entire decade of wavelengths just above the Nyquist cutoff.



## A.4 Comparison to Other Dissipative Schemes

Many Eulerian differencing schemes which have been used for the advection problem are also non-conservative, and it is of interest to compare their dissipation rates to that of the semi-Lagrangian scheme. Three representative schemes are upstream differencing, the Lax-Wendroff scheme, and the Matsuno (Euler-backward) scheme (Haltiner and Williams, 1979; O'Brien, 1986b). It is easy to see from its derivation that upstream differencing is exactly the first-order semi-Lagrangian technique (restricted to being non-multiply-upstream). This technique produces an equivalent Laplacian ( $k^2$ ) friction (the same as (A.4)) which is generally considered too dissipative for large-scale atmospheric or oceanic models.

### A.4.1 Lax-Wendroff

It can be shown that the Lax-Wendroff scheme in its usual form is simply a second-order, non-multiply upstream semi-Lagrangian technique. The  $k^4$  spectrum is somewhat surprising, as the Lax-Wendroff scheme can be written in a form that appears to contain Laplacian ( $k^2$ ) friction with a coefficient of  $\frac{1}{2}U^2\Delta t$ .

The advection equation

$$\psi_t = -U\psi_x,$$

defines  $\frac{\partial}{\partial t}$ , so that we may also write

$$\psi_{tt} = U^2\psi_{xx}.$$

The Taylor series expansion for the temporal evolution of  $\psi$  is

$$\psi^{n+1} = \psi^n + \Delta t\psi_t + \frac{\Delta t^2}{2}\psi_{tt} + O(\Delta t^3).$$

Substituting in the definitions for  $\psi_t$  and  $\psi_{tt}$  gives

$$\psi^{n+1} = \psi^n - \Delta t U \psi_x + \frac{\Delta t^2}{2} U^2 \psi_{xx} + O(\Delta t^3).$$

Although this equation appears to be a first-order (in time) advection coupled with a Laplacian dissipation, it is better understood as a quadratic interpolation formula for the value of  $\psi$  at  $x - U\Delta t$ , and is actually second-order in time, with a dissipation that depends on the accuracy of the spatial derivatives. The usual Lax-Wendroff scheme uses centered second-order spatial discretizations for  $\psi_x$  and  $\psi_{xx}$ , resulting in exactly the same transfer function as for the quadratic semi-Lagrangian case. Higher-order spatial discretizations yield cubic and quartic semi-Lagrangian schemes. Increasing the number of terms in the original Taylor series in time increases the temporal accuracy beyond  $O(\Delta t^2)$ . It should be noted here that in multiple spatial dimensions, the straightforward Lax-Wendroff scheme will differ from the semi-Lagrangian scheme using Lagrangian interpolation because Lagrangian interpolation introduces some extraneous terms in the Taylor series expansion to allow separability.

#### A.4.2 Matsuno (Euler-backward)

The Matsuno scheme is a well-known two-step integration technique, which can be written

$$\begin{aligned}\psi_j^* &= \psi_j^n - \frac{U\Delta t}{2\Delta x}(\psi_{j+1}^n - \psi_{j-1}^n) \\ \psi_j^{n+1} &= \psi_j^n - \frac{U\Delta t}{2\Delta x}(\psi_{j+1}^* - \psi_{j-1}^*).\end{aligned}$$

The amplification factor is

$$|\lambda|^2 = 1 - (\alpha \sin k\Delta x)^2 + (\alpha \sin k\Delta x)^4.$$

For long waves, this reduces to

$$|\lambda|^2 = 1 - \alpha^2(k\Delta x)^2 + O(k^4).$$

The equivalent Laplacian friction coefficient for these long waves is

$$A_H = \frac{1}{2\Delta t}\alpha^2\Delta x^2.$$

For long waves the dissipation acts like Laplacian friction, while for shorter waves the higher-order terms act to decrease the order of the dissipation, ultimately bringing the scheme back to neutral stability at  $k\Delta x = \pi$ . This Laplacian friction has a form very similar to that of the linear semi-Lagrangian technique (or upstream differencing), except that it depends on  $\alpha^2$ , rather than  $\alpha$ . For a Courant number of 1, the friction reaches its upper bound of

$$\frac{1}{2} \frac{\Delta x^2}{\Delta t} = 5.6 \times 10^6 \text{m}^2\text{s}^{-1}.$$

## A.5 Discussion

### A.5.1 Dependence on $\Delta t$

The expressions for the amplification factors in sections 2 and 3 all depend on  $\Delta t$  (through the  $\alpha$  term). For a constant advecting velocity, an expression can be derived for the ratio of the decay time scales for various choices of the time step. For convenience, the time step will be halved relative to a standard case, and the decay time scales for the case of quadratic interpolation will be compared.

The ratio of the decay time scales is simply

$$\frac{\tau(\Delta t)}{\tau(\frac{\Delta t}{2})} = \frac{\Delta t}{\ln \lambda(\Delta t)} \frac{\ln \lambda(\frac{\Delta t}{2})}{\frac{\Delta t}{2}}.$$

For long waves (small  $k\Delta x$ ), the Taylor series expansion for quadratic interpolation gives

$$\begin{aligned} \frac{\tau(\Delta t)}{\tau(\frac{\Delta t}{2})} &= 2 \frac{\alpha_2^2(1 - \alpha_2^2)}{\alpha_1^2(1 - \alpha_1^2)} \\ &\quad - \frac{1}{4} \frac{\alpha_2^2(1 - \alpha_2^2)(\alpha_1^2 - \alpha_2^2)(1 - \alpha_1^2 - \alpha_2^2)}{\alpha_1^2(1 - \alpha_1^2)} (k\Delta x)^4 \\ &\quad + O(k\Delta x)^6, \end{aligned}$$

where  $\alpha_1$  and  $\alpha_2$  are defined below. Let  $\hat{\alpha}$  be the Courant number, then let  $\alpha_1$  denote the residual Courant number for the standard case, and  $\alpha_2$  denote the residual Courant number for the half-time-step case. These latter two quantities are defined by

$$\alpha_1 = \hat{\alpha} - \text{NINT}(\hat{\alpha}) \quad (\text{A.6})$$

$$\alpha_2 = \hat{\alpha}/2 - \text{NINT}(\hat{\alpha}/2), \quad (\text{A.7})$$

where  $\text{NINT}()$  is the nearest integer function.

Given these definitions, the coefficient of the second term of (A.6) is small in all cases (typically 2-3 orders of magnitude smaller than the first term). Coupled with the requirement that  $(k\Delta x) \ll 1$  for the expansion to be valid, it is clear that the first term governs the ratio. Fig. 5 shows the base 10 log of the first term of (A.6) for a Courant number varying between 0 and 2. Negative values imply that the *shorter* time step is less dissipative, while positive values imply that the *longer* time step is less dissipative. The ratio goes to infinity at a Courant number of 1.0, since the time scale for decay of the long time step is infinite at that value.

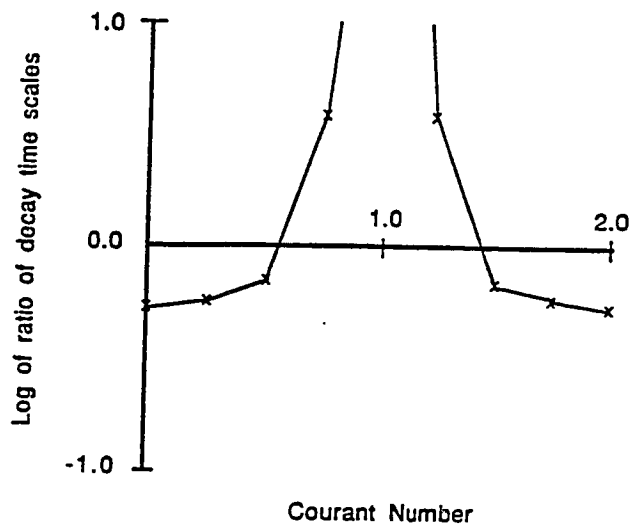


Figure A.5: Base 10 log of the ratio of the decay time scales when the time step is halved, as a function of the Courant number based on the longer time step.

In practice, it is typically observed that semi-Lagrangian advection schemes are less dissipative with longer time steps. In light of Fig. 5, this can be seen as implying that the majority of the flow is contained in the range  $0.5 < \alpha < 1.5$ , which is a reasonable range of values for the requirements of accuracy and efficiency. It is, of course, also possible to estimate a distribution of the Courant numbers and integrate it against the first term in (A.6) (also using (A.6)) to obtain single value for the ratio of the decay time scales. Unless the distribution were strongly weighted to small Courant numbers, the results can be expected to show a decrease in damping with larger time steps.

### A.5.2 Dependence on $\Delta x$

It has already been mentioned that the dissipative decay time scale is related to the grid spacing in such a way that the decay time scale is independent of  $\Delta x$  for a wavelength of a fixed number of grid intervals. For a fixed *absolute*

wavelength, however, decreasing the grid spacing by a factor of  $p$  increases the decay time scales (*i.e.* decreases the damping) of the four schemes by factors of  $p^2$ ,  $p^4$ ,  $p^4$ , and  $p^6$ . It also doubles the Courant number, which may act to modify this improvement. This strong dependence of the effective viscosity on the grid spacing suggests that some care be taken with the choice of discretization parameters.

### A.5.3 Shallow-Water Equation Results

Ritchie (Ritchie, 1988) has performed a series of experiments with a spectral shallow-water model which provide an excellent illustration of the applicability of the effective eddy viscosity concept in a more complex situation. He ran several spectral model simulations with various choices for the advection and diffusion. The Eulerian model was run with a biharmonic diffusion coefficient of  $10^{15}\text{m}^4\text{s}^{-1}$ , and the semi-Lagrangian scheme used Lagrangian bicubic interpolation. Ritchie's figures 10 and 11 show that after 20 days, the T63 resolution semi-Lagrangian code lost about 5% of its total energy, which was about twice the dissipation of the Eulerian case. Increasing the resolution to T126 caused the energy losses in the semi-Lagrangian case to be negligible ( $< 1\%$ ) over the 20-day integration period.

The T63 resolution case corresponds to a  $\Delta x$  of roughly 200 km, and was run with a time step of 3600 s. By this analysis, it should then display an equivalent biharmonic viscosity with a magnitude bounded above by  $10^{16}\text{m}^4\text{s}^{-1}$ . The experiments suggest an effective viscosity of about  $2 \times 10^{15}\text{m}^4\text{s}^{-1}$ , a reasonable agreement. The T126 experiments should have  $\frac{1}{16}$  the viscosity ( $6 \times 10^{14}\text{m}^4\text{s}^{-1}$ ), and the observed viscosity was, in fact, seen to be small compared to  $10^{15}\text{m}^4\text{s}^{-1}$ .

### A.5.4 Application to Ocean Models

Large-scale ocean circulation models are run in two distinct regimes. Non-eddy-resolving simulations typically use grid intervals of 100–400 km and require Laplacian eddy viscosities of the order of  $10^4 \text{m}^2 \text{s}^{-1}$  to account for sub-grid-scale processes. These models are run for decades to centuries, and are used in climate studies. Eddy-resolving simulations have grid spacings in the range of 20–40 km and are typically used with Laplacian eddy viscosities of the order of  $10^2 \text{m}^2 \text{s}^{-1}$ . These models are run for months to years, and are used in dynamical studies.

Semi-Lagrangian advection with linear interpolation requires extremely fine grids to produce numerical diffusion values comparable to those quoted above. Assuming that the time step will be chosen such that an advection of  $1 \text{ m s}^{-1}$  produces a Courant number of 1, (A.4) yields  $A_H = \frac{1}{8} \Delta x$ . For non-eddy-resolving simulations, this specifies a grid interval of 80 km and a time step of 22 hrs, while for the eddy-resolving case, it specifies a grid interval of 0.8 km and a time step of 13 minutes. For both regimes the grid spacings are too small, particularly in the latter case.

Modelling sub-grid-scale dissipation by biharmonic diffusivity is a largely *ad hoc* method. Therefore the values to be used for the coefficients are much more difficult to assign than for the Laplacian case. In the absence of clear knowledge of the physical dissipation, and noting that the wind-driven ocean circulation is a forced, almost inviscid system, it should at least be required that the decay time scales should be longer than the time scales for variability of the forcing. For the wind-driven flow the dominant signals are seasonal, so the dissipative decay time scales should be greater than order 100 days for an accurate simulation. Assuming quadratic or cubic interpolation, fig. 2 suggests that the grid spacing

be less than  $1/10$  (preferably  $1/20$ ) of the shortest wavelength one desires to model accurately. This scaling is the same as is typically suggested for accuracy considerations, however computational resources are not generally available to perform simulations with this level of resolution.

## A.6 Summary

For the simple case of constant advecting velocity, the dissipation due to semi-Lagrangian advection has been quantified and compared to the dissipation of other non-conservative integration schemes. The use of linear interpolation results in dissipation which is effectively Laplacian, while quadratic and cubic interpolation both result in biharmonic dissipation. The coefficients of Laplacian and biharmonic viscosity are shown to be strongly dependent on the resolution, so that care must be taken for the use of this method in long-term integrations. The formulae presented here (particularly (A.4) and (A.5)) can be used to obtain a good estimate for the resolution required to attain the desired degree of conservation in a simulation. For a completely conservative integration, the non-interpolating method of Ritchie (Ritchie, 1986) is available.

This paper does not address the errors in the amplification factors due to incorrect estimation of the departure point, but McDonald (McDonald, 1987) provides a detailed analysis of the order of the errors from that source. The variability in the dissipation due to time- and space-varying velocity fields has also not been addressed. Since this variability would be very difficult to predict or monitor, the semi-Lagrangian technique should not be used as the sole source of viscosity in a viscous flow simulation. It can be used as the sole source of dissipation in a simulation of (nearly) inviscid flow, in which the viscosity is



only present to prevent nonlinear instability (Ritchie, 1988; Cote and Staniforth, 1988).

Figs 1-4 show that the decay time scale as a function of the residual Courant number,  $\alpha$ , is near its shortest (*i.e.* most dissipative) value over most of the range of  $\alpha$ , so that the worst case viscosity coefficients calculated in (A.4) and (A.5) may be typical values if a broad range of residual Courant numbers are present.

## Appendix B

# The Non-Interpolating Semi-Lagrangian Scheme

In (McCalpin, 1988), I showed that the semi-Lagrangian advection scheme using quadratic or cubic interpolation results in excessive numerical dissipation for ocean simulations. A version of the scheme which is conservative was presented by Ritchie (Ritchie, 1986). This scheme splits the advection into two parts: one which consists of advection from grid-point-to-grid-point on the finite-difference grid, and a residual. The grid-point-to-grid-point advection is handled by the semi-Lagrangian scheme, while the advection is handled by an Eulerian scheme and evaluated at the grid-point nearest the middle of the trajectory.

The stability of the scheme depends on the Courant number of the residual advection. When the grid point chosen for the semi-Lagrangian part of the advection is the nearest neighbor, then the Courant number associated with the residual flow can never exceed 0.56. Comparing the stability restrictions of the standard Eulerian scheme to the semi-Lagrangian and non-interpolating semi-Lagrangian yields:

Eulerian:

$$\frac{(|U| + c)\Delta t}{\Delta x} < 1.0$$

Semi-Lagrangian:

$$\frac{c\Delta t}{\Delta x} < 1.0$$

Non-Interpolating Semi-Lagrangian:

$$\frac{c\Delta t}{\Delta x} < 0.44$$

The non-interpolating semi-Lagrangian scheme can therefore be seen to be useful when advection causes more serious time constraints than wave propagation. In the ocean, this is never the case. In mid-latitudes, the maximum baroclinic internal gravity wave phase speeds are up to  $5 \text{ m s}^{-1}$ , compared to maximum advective velocities of about  $1\text{--}2 \text{ m s}^{-1}$ . In the tropical oceans, the maximum gravity-wave phase speed is about  $3 \text{ m s}^{-1}$ , with similar advective speeds.

Based on these values, it is clear that an implicit method for integrating the wave equations would allow a longer time step than an implicit method for just the advective terms. In appendix C, I show that the three-dimensional semi-implicit scheme is not applicable for this purpose. It may be possible to treat only the first few baroclinic modes implicitly and the rest explicitly, but it is unclear what sort of stability properties would govern such a system. In addition, the first baroclinic mode Kelvin waves would still be slowed down by the implicit scheme, producing inaccurate results in equatorial or Rossby adjustment simulations.

# Appendix C

## The Three-Dimensional Semi-Implicit Scheme

### C.1 Introduction

The semi-implicit scheme proposed by (Kwizak and Robert, 1971) for the shallow water equations and by (Robert et al., 1972) for the three-dimensional primitive equations has proven to be a successful scheme for improving the efficiency of atmospheric models. The scheme has also been shown to be effective for layered models in the ocean (e.g. (Hurlburt and Thompson, 1980)). In this appendix, I will discuss the applicability of the scheme to three-dimensional ocean models, and show that the scheme is unsuitable.

### C.2 Application to Shallow Water Equations

The most stringent time step limitation in the hydrostatic, incompressible primitive equations of geophysical fluid dynamics is the limitation due to the propagation of barotropic gravity waves. With phase speeds in excess of  $200 \text{ m s}^{-1}$  in deep water, an explicit model with (for example) 10 km horizontal resolution is limited to time steps of less than one minute. Many models eliminate these

waves by employing the “rigid-lid” surface condition, which prevents the vertically integrated flow from having a divergent component. An alternate method of overcoming this time step limitation is the semi-implicit scheme. In this scheme, the terms in the primitive equations which are responsible for gravity waves are treated implicitly by time averaging. These terms are the pressure gradient terms in the momentum equations and the divergence term in the continuity equation. For the shallow water equations, this yields:

$$\frac{Du}{Dt} - fv = -g \overline{\frac{\partial h}{\partial x}}^t \quad (1)$$

$$\frac{Dv}{Dt} + fu = -g \overline{\frac{\partial h}{\partial y}}^t \quad (2)$$

$$\frac{Dh}{Dt} + H \overline{\left( \frac{\partial u}{\partial x} + \frac{\partial v}{\partial y} \right)}^t + h \left( \frac{\partial u}{\partial x} + \frac{\partial v}{\partial y} \right) = 0, \quad (3)$$

where  $H$  is the mean depth of the fluid and  $h$  is the perturbation of the free surface. For convenience, a flat bottom is assumed, though this is not necessary. The split of the divergence into two terms is also not necessary, but it is convenient, as it makes the resulting Helmholtz equation have a constant Helmholtz coefficient, as will be seen below.

Now apply the leapfrog time differencing scheme and rearrange:

$$u^{n+1} + g\Delta t \frac{\partial h^{n+1}}{\partial x} = u_f \quad (4)$$

$$v^{n+1} + g\Delta t \frac{\partial h^{n+1}}{\partial y} = v_f \quad (5)$$

$$h^{n+1} + \Delta t H \left( \frac{\partial u}{\partial x} + \frac{\partial v}{\partial y} \right)^{n+1} = h_f, \quad (6)$$

where  $u_f$ ,  $v_f$ , and  $h_f$  represent all the terms which are evaluated at time levels  $n$ , and  $n - 1$ , which are known. Next, take the divergence of the momentum equations and replace the divergence term in (6). This yields a Helmholtz equation for the depth anomaly:

$$\left( \frac{\partial^2 h}{\partial x^2} + \frac{\partial^2 h}{\partial y^2} \right)^{n+1} - \frac{1}{gH\Delta t^2} h^{n+1} = \frac{1}{gH\Delta t^2} \left( \frac{\partial u_f}{\partial x} + \frac{\partial v_f}{\partial y} \right) - \frac{1}{gH\Delta t^2} h_f. \quad (7)$$

After this equation is solved,  $u^{n+1}$  and  $v^{n+1}$  are obtained from (4) and (5) by back-substitution. The scheme is unconditionally stable (ignoring advection) for  $|h| < H$ .

### C.3 Application to Three-Dimensional Equations

For the three-dimensional primitive equations, the situation is somewhat more complicated. Following (Robert et al., 1972), and ignoring diffusive processes and topography, the equations for the oceanic case can be reduced to:

$$\frac{Du}{Dt} - fv = -\frac{1}{\rho_0} \overline{\frac{\partial p}{\partial x}}^t \quad (8)$$

$$\frac{Dv}{Dt} + fu = -\frac{1}{\rho_0} \overline{\frac{\partial p}{\partial y}}^t \quad (9)$$

$$\frac{\partial p}{\partial z} = -g\rho \quad (10)$$

$$\frac{\partial u}{\partial x} + \frac{\partial v}{\partial y} + \frac{\partial w}{\partial z} = 0 \quad (11)$$

$$\frac{D\rho}{Dt} = 0. \quad (12a)$$

A horizontal mean density and its associated hydrostatic pressure are subtracted from the equations, and advection of the mean density field is treated implicitly, so (12a) becomes

$$\frac{D\rho'}{Dt} + \bar{w}^t \frac{\partial \bar{\rho}}{\partial z} = 0. \quad (12b)$$

Again, leapfrog time differencing is applied and the divergence of the momentum equations is used to replace the horizontal divergence in the continuity equation (applied at time level  $n + 1$ ) to yield:

$$u^{n+1} + \frac{\Delta t}{\rho_0} \frac{\partial p'^{n+1}}{\partial x} = u_f \quad (13)$$

$$v^{n+1} + \frac{\Delta t}{\rho_0} \frac{\partial p'^{n+1}}{\partial y} = v_f \quad (14)$$

$$-\frac{\Delta t}{\rho_0} \left( \frac{\partial^2 p'}{\partial x^2} + \frac{\partial^2 p'}{\partial y^2} \right)^{n+1} + \frac{\partial w^{n+1}}{\partial z} = - \left( \frac{\partial u_f}{\partial x} + \frac{\partial v_f}{\partial y} \right) \quad (15)$$

$$\rho'^{n+1} + \Delta t w^{n+1} \frac{\partial \bar{\rho}}{\partial z} = \rho_f \quad (16)$$

Solving (16) for  $w^{n+1}$  and applying the hydrostatic relation (10) gives

$$w^{n+1} = -\frac{\gamma}{\Delta t} \rho'^{n+1} + \frac{\gamma}{\Delta t} \rho_f$$

$$w^{n+1} = \frac{\gamma}{g\Delta t} \frac{\partial p'^{n+1}}{\partial z} + \frac{\gamma}{\Delta t} \rho_f,$$

where  $\gamma \equiv (\partial \bar{\rho} / \partial z)^{-1}$ .

Taking  $\partial/\partial z$  of this allows substitution into (15) to yield a 3-D Helmholtz equation for the perturbation pressure

$$\left(\frac{\partial^2 p'}{\partial x^2} + \frac{\partial^2 p'}{\partial y^2}\right)^{n+1} - \frac{\rho_0}{g\Delta t^2} \frac{\partial}{\partial z} \left(\gamma \frac{\partial p'}{\partial z}\right)^{n+1} = \frac{\rho_0}{\Delta t} \left(\frac{\partial u_f}{\partial x} + \frac{\partial v_f}{\partial y}\right) + \frac{\rho_0}{\Delta t} \frac{\partial}{\partial z} (\gamma \rho_f). \quad (17)$$

After this is solved for  $p'^{n+1}$ , back substitution into (13), (14), (10), and (16) yields  $u^{n+1}$ ,  $v^{n+1}$ ,  $\rho'^{n+1}$ , and  $w^{n+1}$ .

## C.4 Discussion

The preceding derivation contains one very significant problem. The scheme rests on the ability to invert (16) for  $w^{n+1}$ . At first glance, this appears possible, since it is always possible to choose a reference state such that  $\partial\bar{\rho}/\partial z > 0$  at all locations. With such a choice, the scheme is *numerically* well-posed (*i.e.* one never divides by zero). It is, however, *physically* ill-posed wherever the vertical derivative of the *total* density vanishes, because (12a), and hence (16), contains no information about  $w$  in those regions — quite independent of any choice of the mean reference state.

Unlike the atmosphere, in the ocean the vertical gradient of the total density field is expected to be very close to zero in the deep ocean everywhere, and may also vanish in the upper mixed layer. The scheme is therefore probably only safe to apply in the (vertical) region of the main thermocline. If the vertical density gradient is small but not quite zero, the problem is very sensitive to noise in the density field. Looking at the continuous problem,  $w$  is inversely proportional to  $\partial\rho/\partial z$ , and the sensitivity to small changes in the vertical density gradient is



$$\frac{\partial w}{\partial \left( \frac{\partial \rho}{\partial z} \right)} \propto -\frac{1}{\left( \frac{\partial \rho}{\partial z} \right)^2},$$

which rapidly becomes very large for small  $\partial\rho/\partial z$ .

This error is especially pernicious because the scheme is numerically well-behaved. If the vertical derivative of the total density vanishes, then using this scheme *should* produce a division by zero! The *apparent* information in (16) about the vertical velocity arises solely from the  $O(\Delta t^2)$  truncation error of the time averaging of  $w$ .

It is easy to see that for the hydrostatic primitive equations, no other robust, physically well-posed schemes can be developed which calculate  $w$  implicitly, since outside of the continuity equation,  $w$  appears only in advective terms. There is therefore no way to solve for  $w$  in terms of the other variables, or *vice versa*, without inverting an advection term for  $w$ , and this can be expected to fail routinely in the ocean. This strongly suggests that no unconditionally stable integration schemes are possible.

Mathematically, the difficulty with this scheme is related to the fact that the vertical eigenfunctions of the 3-D Helmholtz operator do not form a complete set when the vertical density gradient vanishes over a region. When the vertical gradient of the density becomes very small (though not exactly zero), the ill-conditioning of the problem causes the eigenfunctions to lose their orthogonality when calculated in finite-precision arithmetic (particularly in 32-bit precision). Because of this lack of orthogonality, if the Helmholtz equation is solved by projection onto the vertical eigenfunctions, then any small-vertical-scale information in the forcing terms in deep water will be ignored. Such information can come

from boundary conditions, or from deep flows whose density contrast is not represented in the basic state.

The situation is not changed for the case in which compressibility is considered. This case (as would be required in the atmosphere or perhaps the deep ocean) generates completely analogous equations, except that the vertical derivative of the mean state density is replaced by the vertical derivative of the mean state potential density. The scheme is then physically ill-posed if the vertical potential density gradient vanishes.

Of course the scheme will generate incorrect answers in the atmosphere (as well as in the ocean) if the stability becomes neutral, but this does not happen in the atmosphere on large horizontal scales. Static *instability*, which occurs on small scales in both the ocean and atmosphere, is a different problem, and must be treated by some sort of parameterization of the convection.